

UNIVERSIDADE DE SÃO PAULO  
INSTITUTO DE FÍSICA DE SÃO CARLOS

EMERSON CRISTIANO BARBANO

Third-harmonic generation at interfaces with femtosecond pulses: self-focusing contribution and nonlinear microscopy

São Carlos  
2016



EMERSON CRISTIANO BARBANO

Third-harmonic generation at interfaces with femtosecond pulses: self-focusing contribution and nonlinear microscopy

Thesis presented to the Graduate Program in Physics at the Instituto de Física de São Carlos, Universidade de São Paulo to obtain the degree of Doctor of Science.

Concentration area: Basic Physics

Advisor: Prof. Dr. Lino Misoguti

Corrected Version

(Original version available on the Program Unit)

São Carlos  
2016

AUTHORIZE THE REPRODUCTION AND DISSEMINATION OF TOTAL OR PARTIAL COPIES OF THIS THESIS, BY CONVENTIONAL OR ELECTRONIC MEDIA FOR STUDY OR RESEARCH PURPOSE, SINCE IT IS REFERENCED.

Cataloguing data reviewed by the Library and Information Service  
of the IFSC, with information provided by the author

Barbano, Emerson Cristiano

Third-harmonic generation at interfaces with femtosecond pulses: self-focusing contribution and nonlinear microscopy / Emerson Cristiano Barbano; advisor Lino Misoguti - reviewed version -- São Carlos 2016.

101 p.

Thesis (Doctorate - Graduate Program in Basic Physics) -- Instituto de Física de São Carlos, Universidade de São Paulo – Brasil , 2016.

1. Nonlinear optics. 2. Third-harmonic generation. 3. Self-focusing. 4. Femtosecond laser. 5. SPIFI microscopy. I. Misoguti, Lino, advisor. II. Title.

*To my parents and brother,  
for their encouragement, support and endless love.*



## ACKNOWLEDGEMENTS

First and foremost I would like to thank my advisor Prof. Dr. Lino Misoguti. He is an inspiring researcher and I am very thankful for having been given the opportunity to work with him. His expert advice, optimism, support and patience have been unwavering throughout the entirety of this project.

Next, I would like to thank Prof. Dr. Sergio Carlos Zilio for his guidance during my undergrad, opportunities and for the valuable discussions about this research.

I would also like to express my gratitude to the whole Photonics Group team: Professors Dr. Cleber R. Mendonça, Dr. Leonardo De Boni, and Dr. Luís G. Marcassa; the staff, André Romero, Daniel Foschini, and Dr. Marcos Cardoso; and all my labmates past and present for their support over the years, Adriano Otuka, Anderson R. de Oliveira, Caio Wetterich, Fernando Gotardo, Franciele Henrique, Gustavo B. de Almeida, Henry Passagem, Jessica Dipold, Jonathas Siqueira, Jorge Gomes, Jorge Massayuki, José Francisco Domenegueti, Juliana M. P. de Almeida, Kelly T. de Paula, Leandro Cocca, Luís Gonçalves, Marcelo Vivas, Maria L. Miguez, Marlon Melhado, Nathália Tomázio, Oriana Salas, Paulo Henrique Ferreira, Pedro Cônsoli, Renato Martins, Regina E. Alves, Ruben Rodriguez, Sabrina N. C. dos Santos, Tarcísio Figueredo, Tiago G. B. de Souza, and Vinícius Tribuzi. Thank you all for providing an encouraging lab atmosphere and for the stimulating discussions.

I wish to thank Kerriane Harrington for having helped me with part of the research and for her friendship.

My sincere thanks also goes to Prof. Dr. Jeff Squier, who provided me an opportunity to join his team as intern at Colorado School of Mines. Despite his busy schedule he always made himself available for my needs, whether professional or personal. His group provided me an excellent stay in Golden. Thanks Alyssa Motz, Erica Block, and Nathan Worts. I would especially like to thank Michael D. Young, not only for having taught me the SPIFI technique but also for our many conversations and his friendship.

Many thanks go to the IFSC library members, for their attention and sympathy, and to my friends at USP, André Orlandi, Geisiane Rosa, Leonardo A. de Castro, Pedro Soares, Rafael F. Rossetti, and Victor Teizen for the enjoyable talks and for all the fun we have had together.

I must acknowledge and thank my parents, Rosa and José Carlos, my brother, Elton, and my uncle, Ronaldo (Pilito), for their support and encouragement over the years. They provided me the chance to get here.

A very special thanks to my girlfriend, Rafaella, for all moments we pass together and for her invaluable love and attention.

Finally, I would like to thank the São Paulo Research Foundation (FAPESP) for the financial support, grants: 2011/22787-7 (scholarship) and 2015/14666-6 (internship).

*“It’s not that I’m so smart,  
it’s just that I stay with problems longer”*

**Albert Einstein**



## ABSTRACT

BARBANO, E. C. **Third-harmonic generation at interfaces with femtosecond pulses: self-focusing contribution and nonlinear microscopy**. 2016. 101 p. Thesis (Doctor in Science) - Instituto de Física de São Carlos, Universidade de São Paulo, São Carlos, 2016.

Third-harmonic generation (THG) is a fundamental nonlinear optical process that has been used in different applications such as third-order nonlinear materials characterization and nonlinear microscopy. It is widely employed since the third-order nonlinearity is the most important in isotropic materials and THG occurs in all media regardless of symmetry. In the tightly focused laser beam condition THG is observed only at the material's interfaces, where the focal symmetry is broken due to the presence of two media with different refractive index and/or third-order susceptibilities. Measuring slabs of different types of optical glasses, using femtosecond laser pulses, we could explain the asymmetric THG intensity profile observed at the interfaces. The harmonic generated at the exit interface is systematically stronger than the one generated at the entrance and this phenomenon can be understood by taking into account the presence of self-focusing effects. Basically, the self-focusing reduces the beam waist radius at the exit interface, resulting in greater laser irradiance and, consequently, higher THG. This study was then extended to the interfaces of a cuvette filled with organic solvents. Such systems present four interfaces and a mixture of nonlinear processes contributions since the cuvette walls present only electronic nonlinearity and the solvents present both electronic and orientational ones. In this way, the solvents may present an additional self-focusing contribution and, due to the noninstantaneous nature of the orientational process, the self-focusing from the solvent may be influenced by the pulse duration. In this case, the THG, which is an instantaneous electronic phenomenon, can be indirectly affected by pulse duration by means of the self-focusing effect. Usually, the slow orientational contribution is not considered for materials characterization by THG which may lead to incorrect nonlinear coefficient values, that means our study is important from the fundamental physics point of view and also for applications such as materials characterization. Based on the application of THG in nonlinear microscopy, we also present a microscopy technique which makes use of spatial frequency-modulated imaging (SPIFI) with single element detection. The microscope was developed at Colorado School of Mines (CSM) during an internship. The system uses a spatial light modulator (SLM) to provide the spatial frequency modulation and permits enhanced resolution images. THG SPIFI images are shown for the first time and we also

report images obtained by other nonlinear optical process. In summary, the studies presented in this PhD work are of great importance for THG fundamental understanding, materials characterization and nonlinear optical microscopy.

Keywords: Nonlinear optics. Third-harmonic generation. Self-focusing. Femtosecond laser. SPIFI microscopy.

## RESUMO

BARBANO, E. C. **Geração de terceiro harmônico em interfaces com pulsos de femtossegundos: contribuição da autofocalização e microscopia não linear.** 2016. 101 p. Tese (Doutorado em Ciências) - Instituto de Física de São Carlos, Universidade de São Paulo, São Carlos, 2016.

Geração de terceiro harmônico (GTH) é um processo óptico não linear fundamental que tem sido usado em diferentes aplicações, como em caracterização óptica não linear de materiais e microscopia não linear. Ele é amplamente empregado uma vez que a não linearidade de terceira ordem é a mais importante em materiais isotrópicos e GTH ocorre em todos os meios independente da simetria. Na condição de feixe fortemente focalizado a GTH é observada apenas nas interfaces do material, onde a simetria focal é quebrada devido à presença de dois meios com diferentes índices de refração e/ou susceptibilidades de terceira ordem. Medindo lâminas de diferentes tipos de vidros ópticos, com pulsos de laser de femtossegundos, nós explicamos o perfil assimétrico de intensidade de GTH observado nas interfaces. O harmônico gerado na interface de saída é sistematicamente mais intenso do que o gerado na entrada e este fenômeno pode ser entendido levando-se em conta a presença do efeito de autofocalização. Basicamente, a autofocalização reduz a cintura do feixe na interface de saída do material, resultando em uma maior irradiância e, conseqüentemente, maior GTH. Este estudo foi estendido para o caso de interfaces de uma cubeta preenchida com diferentes solventes orgânicos. Tais sistemas apresentam quatro interfaces e uma mistura na contribuição dos processos não lineares, dado que as paredes da cubeta apresentam apenas não linearidade eletrônica e os solventes podem apresentar não linearidades tanto eletrônicas quanto orientacionais. Neste sentido, os solventes podem apresentar uma contribuição adicional de autofocalização e, devido à natureza não instantânea do processo orientacional, a autofocalização proveniente do solvente pode ser influenciada pela duração do pulso. Neste caso, a GTH, que é um fenômeno eletrônico (instantâneo), pode ser indiretamente afetada pela duração do pulso por meio do efeito de autofocalização. Usualmente, a contribuição orientacional não é considerada na caracterização de materiais por GTH, o que pode levar à valores incorretos para os coeficientes não lineares, o que significa que nosso estudo é importante do ponto de vista de física fundamental como também em aplicações como caracterização de materiais. Por conta da aplicação da GTH em microscopia não linear, apresentamos também nesta tese uma técnica de microscopia, que baseia-se em uma

modulação em frequência espacial para imageamento (SPIFI) com uso de um detector de elemento único. O microscópio foi desenvolvido na Colorado School of Mines (CSM) durante um período de estágio. O sistema utiliza um modulador espacial de luz (SLM) para produzir a modulação em frequência espacial e permite obtenção de imagens em alta resolução. Imagens por GTH SPIFI são mostradas pela primeira vez e também apresentamos imagens obtidas por outros processos ópticos não lineares. Em resumo, os estudos apresentados neste trabalho de doutorado são de grande importância para o entendimento fundamental do processo de GTH, caracterização de materiais e microscopia óptica não linear.

Palavras-chave: Óptica não linear. Geração de terceiro harmônico. Autofocalização. Laser de femtossegundo. Microscopia SPIFI.

## LIST OF FIGURES

Figure 2.1 –	Field amplitude distribution for a Gaussian laser beam. ....	31
Figure 2.2 –	Representation of the beam waist and wavefront radius of curvature behavior during the propagation of a Gaussian beam. ....	32
Figure 2.3 –	Harmonic generation efficiency as a function of $\Delta kL/2$ . ....	35
Figure 2.4 –	Maker fringes pattern for the harmonic generated in plane-wave limit. ....	36
Figure 2.5 –	Phase matching integral dependence with $b\Delta k$ for THG. ....	37
Figure 2.6 –	Gouy phase shift. ....	37
Figure 2.7 –	Wavevector diagram for third-harmonic generation. For $\Delta k$ positive, (a), due to angular spread of the fundamental beam wavevectors, (b), it is possible to obtain the phase-matched condition while for $\Delta k$ negative, (c), THG cannot occur efficiently. ....	38
Figure 3.1 –	Self-focusing of light. As a result of the nonlinear interaction the material behaves as if it had larger optical thickness at the center of the beam (a). For a material short enough, the focal plane will be outside of the medium (b), however, for a material sufficiently long or beam intensity sufficiently large, the focal plane will occur within the medium (c). ....	45
Figure 4.1 –	Schematic self-focusing action represented by the dashed line for beam focused at the exit (a) and entrance (b) interfaces. ....	49
Figure 4.2 –	Experimental setup for measuring the TH signal. DM, dichroic mirrors. ....	50
Figure 4.3 –	THG Z-scan signal for silica, BK7, SK11, and F2 obtained at an average laser power of $\sim 0.44$ mW. An offset of 0.1 between consecutive curves was introduced for better visualization. ....	51
Figure 4.4 –	Normalized TH peaks generated at the entrance (red) and exit (black) interfaces obtained with 0.44 mW pump power. The points are the experimental results, and the lines are fittings with Gaussian functions. ....	52
Figure 4.5 –	Normalized TH peaks generated at the entrance (red) and exit (black) interfaces for silica obtained with 0.8 mW pump power. The points are the experimental results, and the lines are fittings with Gaussian functions. ....	52

Figure 4.6 –	THG peak values at the entrance (red) and exit (black) interfaces as a function of the incident laser power for silica, BK7, SK11, and F2. The symbols are the experimental data, while the solid lines are results obtained with the model proposed. The numbers in parenthesis indicate the slopes (THG dependence with laser power).....	53
Figure 4.7 –	$2z_r$ from the TH collected as a function of the pump laser power for silica, BK7, SK11, and F2 glasses. The solid lines were obtained from Eq. (4.10). .....	55
Figure 5.1 –	(I) Definition of the cuvette interfaces and, (II) typical TH intensity curve for silica/DMSO system. ....	61
Figure 5.2 –	Open squares show values of $J/b$ as a function of $ b\Delta k $ calculated with Eq. (5.4). The solid curve is the best fit obtained by using Eq. (5.7) and the inset is just an expanded view. ....	62
Figure 5.3 –	THG signals for three different solvents as a function of the sample position for the four interfaces. We used two different cuvettes: silica (S) and B270 glass (G). The curves were obtained using pump powers of 0.430 mW and 0.415 mW for silica and B270 cuvettes, respectively. Other pump powers present very similar curves. ....	64
Figure 5.4 –	Nonlinear susceptibility ratios for all solvents obtained with TH peak ratios using Eq. (5.6) for different laser powers. We used two different cuvettes: silica (S) and B270 glass (G). The error bar for each laser power comes from dispersion among the four possible ratios. ....	64
Figure 5.5 –	Peak values of THG curves at the silica cuvette interfaces as a function of input laser power for all solvents and all interfaces. The symbols are the experimental data and the solid lines are the fits using the empirical model. The numbers in parentheses are the approximate slopes.....	66
Figure 5.6 –	Peak values of THG curves at the B270 cuvette interfaces as a function of input laser power for all solvents and all interfaces. The symbols are the experimental data and the solid lines are the fits using the empirical model. The numbers in parentheses are the approximate slopes.....	67
Figure 6.1 –	(I) Integrated THG signal. The interfaces were labeled as (a) air-silica (entrance interface), (b) silica-solvent (there is no signal at this interface), (c) solvent-silica and (d) silica-air (exit interface). The TH profiles are presented for acetone, chloroform and DMSO for different pulse durations. (II) Absorbance spectrum for each solvent.....	72
Figure 7.1 –	Schematic of first SPIFI setup.....	77

Figure 7.2 – SPIFI system configuration with circular reticle (mask) for superresolved multiphoton microscopy. Schematic representations in the $(x,z)$ (a) and $(y,z)$ (b) planes. ....	79
Figure 7.3 – (a) circular reticle. (b) modulation in $\theta$ at different values of $r$ . (c) modulation in $r$ at different values of $\theta$ . ....	80
Figure 7.4 – (a) equivalent Cartesian mask to be used with the 2D SLM. (b) modulation in the $x$ dimension at different values of $y$ . (c) modulation in the $y$ dimension at different values of $x$ . ....	80
Figure 7.5 – Schematic diagram for amplitude modulation using cylindrical lens and galvanometric mirror, CL = cylindrical lens, PBS = polarizing beamsplitter, $\lambda/2$ = half waveplate, SM = scan mirror (galvanometric mirror), SL = scan lens, Obj = objective lens. The half waveplate should rotate the input polarization by $45^\circ$ . ....	82
Figure 7.6 – (a) SPIFI trace of the laser beam. (b) beam profile retrieved. ....	83
Figure 7.7 – Central part of the line cursor blocked with a stick. ....	84
Figure 7.8 – Measurement with a stick blocking the central part of the beam as shown in Fig. 7.6. (a) SPIFI trace of the laser beam. (b) beam profile retrieved. ....	84
Figure 7.9 – THG SPIFI signal of polystyrene beads (a). Fourier transform of the signal with respect to the scan time where it is possible to observe the higher-order signals (b). ....	84
Figure 7.10 – First-, second- and third-order signals obtained in the Fourier transform. The higher orders make possible superresolution images. ....	85
Figure 7.11 – Portion of an onion skin sample. On the left we see the first order and on the right the second order of diffraction, both correspond to the same portion of the sample. The bars were used to verify the second order is twice the thickness of the first, 31 and 15 pixels respectively. ....	86
Figure 7.12 – TPEF images collected from a portion of onion skin sample with SPIFI. (a) first- and (b) second-order SPIFI images. (c) A black screen is placed on the left side of the image to avoid the saturation caused by the lower order. ....	86
Figure 7.13 – TPEF images collected from lens tissue sample. (a) – (c) first through third order images. Scale bar: $20\mu\text{m}$ . (d) sample under white light illumination, the vertical lines indicate approximately the portion of the sample scanned by the line cursor. ....	87

Figure 7.14 – SHG images collected from cornstarch in water. (a) SPIFI image, (b) sample under white light illumination, the vertical lines indicate approximately the portion of the sample scanned by the line cursor. ....	88
Figure 7.15 – First THG SPIFI image. (a) and (b) are the first and second order images of polystyrene beads (diameter = 6 $\mu\text{m}$ ). (c) sample under white light image. Scale bar: 20 $\mu\text{m}$ . ....	88
Figure 7.16 – THG SPIFI images of polystyrene beads (diameter = 6 $\mu\text{m}$ ). (a) – (c) first through third order images. Scale bar: 20 $\mu\text{m}$ . (d) portion of the sample under white light illumination. ....	89
Figure 7.17 – (a) THG SPIFI image of polystyrene beads (diameter = 6 $\mu\text{m}$ ) using linear vs circular configuration. (b) portion of the sample under white light illumination. Scale bar: 20 $\mu\text{m}$ . ....	90

## LIST OF TABLES

Table 4.1 – Optical glasses used with corresponding refractive index and thickness.....	50
Table 4.2 – Theoretical and experimental $n_2$ . The experimental values were obtained from the ratio $B_{glass} / B_{silica}$ .....	56
Table 5.1 – Dispersion properties of the materials used <sup>a,b</sup> .....	63
Table 5.2 – Nonlinear susceptibility ratios of the solvents obtained by averaging the experimental data of Fig. 5.4 <sup>a</sup> .....	65
Table 5.3 – Coefficients $A$ and $B$ obtained for the silica cuvette for interfaces (b) and (c) <sup>a</sup> .....	67
Table 5.4 – Coefficients $A$ and $B$ obtained for the B270 cuvette for interfaces (b) and (c) <sup>a</sup> .....	68
Table 5.5 – Ratios $n_{2solvent} / n_{2cuvette}$ obtained with the coefficients $B$ and $A^a$ .....	68



## LIST OF ABBREVIATIONS AND ACRONYMS

CCD	Charge Coupled Device
CPA	Chirped Pulse Amplification
CW	Continuous-Wave
DFG	Difference-Frequency Generation
DMSO	Dimethyl Sulfoxide
FS	Femtosecond
FWHM	Full Width at Half Maximum
KGW	Potassium Gadolinium Tungstate
LUT	Look-Up-Table
NA	Numerical Aperture
OPA	Optical Parametric Amplifier
PBS	Polarizing Beamsplitter
PMT	Photomultiplier Tube
SFG	Sum-Frequency Generation
SHG	Second-Harmonic Generation
SLM	Spatial Light Modulator
SPIFI	SPatIal Frequency-modulated Imaging
SVEA	Slowly Varying Envelope Approximation
TH	Third Harmonic
THG	Third-Harmonic Generation
TPEF	Two-Photon Excitation Fluorescence



# CONTENTS

<b>1</b>	<b>INTRODUCTION.....</b>	<b>23</b>
<b>2</b>	<b>THEORETICAL FOUNDATIONS – HARMONIC GENERATION .....</b>	<b>27</b>
2.1	Gaussian beams .....	30
2.2	Harmonic generation using focused Gaussian beams .....	32
<b>3</b>	<b>NONLINEAR REFRACTIVE INDEX AND SELF-FOCUSING EFFECT.....</b>	<b>41</b>
3.1	Nonlinear refractive index.....	41
3.2	Self-focusing of light.....	44
<b>4</b>	<b>THIRD-HARMONIC GENERATION AT OPTICAL GLASSES INTERFACES.....</b>	<b>47</b>
4.1	Methodology .....	47
4.2	Results .....	50
4.3	Discussion .....	56
<b>5</b>	<b>THIRD-HARMONIC GENERATION AT THE INTERFACES OF A CUVETTE FILLED WITH ORGANIC SOLVENTS.....</b>	<b>57</b>
5.1	Theoretical approach.....	58
5.2	Experiments.....	60
5.3	Results and Discussion.....	61
<b>6</b>	<b>THG AT ORGANIC SOLVENTS INTERFACES AS A FUNCTION OF PULSE DURATION.....</b>	<b>71</b>
6.1	Results .....	72
<b>7</b>	<b>SPIFI IMAGING WITH A PROGRAMMABLE 2D SPATIAL LIGHT MODULATOR..</b>	<b>75</b>
7.1	Abstract .....	75
7.2	Introduction .....	75
7.3	SPAtial Frequency-modulated Imaging - SPIFI .....	77
7.4	Experimental setup.....	81
7.5	Results .....	82
7.6	Discussion .....	90
<b>8</b>	<b>GENERAL CONCLUSIONS AND PERSPECTIVES .....</b>	<b>93</b>
	<b>REFERENCES .....</b>	<b>95</b>



## 1 INTRODUCTION

Third-harmonic generation (THG) at interfaces<sup>1</sup> has long been of interest for third-order nonlinear material's characterization,<sup>2-4</sup> ultrashort pulse measurements,<sup>5-6</sup> and nonlinear microscopy.<sup>7-8</sup> Any of these applications requires the precise knowledge of the fundamental processes involved for a correct interpretation of the results. It is well known that for a thick sample (thickness much larger than the Rayleigh range), the THG vanishes in bulk media because the Gouy phase shift<sup>9</sup> leads to the destructive interference between third harmonics (TH) generated before and after the focus.<sup>3,10-11</sup> The THG occurs only at interfaces because the focal symmetry is broken by the presence of two materials with different refractive indices and/or third-order susceptibilities. As a result, TH at interfaces can be used to measure the discontinuity in the fast electronic part of the cubic susceptibility,  $\Delta\chi^{(3)}(-3\omega; \omega, \omega, \omega)$ . However, there are cases where such a nonlinear process is not acting alone during the light-matter interaction, leading to difficulties in the reliable interpretation of the expected signal behavior.

We have studied the THG of femtosecond (fs) pulses in different glass slabs<sup>12</sup> (where the sample was scanned along the beam propagation direction) and we observed the TH generated at the entrance and exit interfaces are unequal. There are previous works where the asymmetry of THG peaks was observed and a few explanations were proposed. For example, we may quote the constructive interference due to the Fresnel reflections,<sup>12</sup> the overcompensation of group velocity dispersion<sup>13</sup> at output interfaces, and even some theoretical studies where the non-negligible third-order susceptibility of air can cause asymmetry between front and back interface peaks.<sup>14</sup> Therefore, it seems worthwhile to investigate more carefully the contributions of linear and nonlinear refractive indices at the interfaces of different materials and the main goal of the present research project is to study this asymmetry of THG peaks.

The present dissertation reports on THG measurements carried out with a setup similar to the Z-scan technique<sup>15</sup> at the tightly focused laser beam condition. We performed THG measurements at air-glass interfaces of several optical glasses, as well as at glass-liquid interfaces, where we have used a cuvette filled with selected organic solvents. In the first case, by carefully controlling the sample position and laser power, we could follow the evolution of the THG intensity at both interfaces (entrance and exit) of different glasses. We found that the TH generated at the entrance interface follows the expected cubic power dependence, which is characteristic of a third-order process, but the THG at the exit presents a

slope higher than three, indicating that another nonlinear effect is also present. We propose that self-focusing strongly contributes to the THG asymmetry because the positive nonlinear refraction decreases the effective beam waist as the pulse propagates, resulting in higher laser irradiance at the exit interface. This unbalances the TH generated at the entrance and exit interfaces. In the case of a cuvette filled with different solvents, we extended our study to a different configuration. Such a system presents four interfaces separating three materials of different refractive indices and third-order nonlinear susceptibilities. Using different cuvettes and solvents we have a variety of interfaces with different linear and nonlinear optical properties. Although the THG is due to the electronic part of the nonlinear susceptibility, it can suffer from the influence of the self-focusing effect, that can have both instantaneous electronic and slow nuclear contributions. This mixture of two distinct third-order nonlinear processes was never considered for such interfaces. Here, using the cuvette walls as a reference and taking into account the self-focusing effect, we could determine by the THG signals the nonlinear refractive indices,  $n_2$ , and third-order nonlinear susceptibilities of the solvents,  $\chi^{(3)}$ . We also proposed a study of the self-focusing effect on the THG by changing the pulse duration of the pump beam. Due to the noninstantaneous nature of the orientational process, the self-focusing from the solvent may be influenced by the pulse duration. In this case, the THG, which is an instantaneous electronic phenomenon, can be indirectly affected by pulse duration by means of the self-focusing effect from noninstantaneous nonlinearity.

One additional research was added at the end of this dissertation. As mentioned earlier, THG is a nonlinear optical process that can be used for nonlinear microscopy and, in this way, we report a microscopy technique based on spatial frequency-modulated imaging (SPIFI),<sup>16-19</sup> with a programmable 2D spatial light modulator (SLM). With this technique we were able of getting TH images, as well as images by other nonlinear optical processes such as Two-photon excitation fluorescence (TPEF)<sup>20-22</sup> and Second-harmonic generation (SHG).<sup>23-25</sup> This microscope was developed at the Squier's Group during a six-month internship at Colorado School of Mines, Golden, CO, USA.

We can summarize the organization of this dissertation as follows: in Chapter 2 we present a review of the fundamental concepts on nonlinear optics and third-harmonic generation. In Chapter 3 an analytical expression for the nonlinear refractive index is derived and the self-focusing effect is presented. Chapters 4 and 5 are based on a compilation of journal articles already published<sup>26-27</sup> where we present the main results of this dissertation (study of THG at different interfaces). Basically, in Chapter 4 we describe the experimental setup, the approach we are going to use and show the results for THG at the interfaces of

different types of optical glasses, and, in Chapter 5, the study was extended to the interfaces of a cuvette filled with different solvents. In Chapter 6 we have preliminary results about the influence of orientational nonlinearity on THG at organic solvents by changing the pulse duration. In Chapter 7 we focus on the SPIFI microscope and, finally, in Chapter 8 we present the general conclusions and perspectives.



## 2 THEORETICAL FOUNDATIONS – HARMONIC GENERATION

To understand the nonlinear interaction between light and matter we can consider the electromagnetic wave equation, which in the SI system of units is:<sup>10</sup>

$$\nabla^2 \vec{E} - \mu_0 \varepsilon_0 \frac{\partial^2 \vec{E}}{\partial t^2} = \mu_0 \frac{\partial^2 \vec{P}}{\partial t^2} \quad (2.1)$$

where  $\vec{E}$  is the electric field,  $\mu_0$  and  $\varepsilon_0$  are, respectively, the permeability (or magnetic constant) and the permittivity of free space, and  $\vec{P}$  is the induced polarization. Equation (2.1) describes the propagation of electromagnetic waves through a medium. In the case of linear optics, the induced polarization  $\vec{P}$  depends linearly on the electric field,

$$\vec{P} = \varepsilon_0 \vec{\chi} : \vec{E}. \quad (2.2)$$

In Eq. (2.2),  $\vec{\chi}$  is the electric susceptibility and its tensor nature indicates the polarization and electric field are not necessarily parallel as, for example, in anisotropic media. For isotropic media, the electric susceptibility is a scalar quantity,  $\chi$ .

Using ordinary light sources, the radiation field is much smaller than the fields that bind the electrons to the atoms, and the relation between the polarization and the radiation field is linear, Eq. (2.2). However, using a radiation field comparable with the atomic fields, this relation is no longer a linear one, and is often described by expressing the polarization as a power series in terms of the electric field:<sup>10,28</sup>

$$\vec{P} = \varepsilon_0 \vec{\chi}^{(1)} : \vec{E} + \varepsilon_0 \vec{\chi}^{(2)} : \vec{E} \vec{E} + \varepsilon_0 \vec{\chi}^{(3)} : \vec{E} \vec{E} \vec{E} + \dots, \quad (2.3)$$

where  $\vec{\chi}^{(1)}$  is the same linear susceptibility used in Eq. (2.2), and  $\vec{\chi}^{(2)}$  and  $\vec{\chi}^{(3)}$  are known as second- and third-order nonlinear susceptibilities, respectively. If we separate the linear and nonlinear contributions in Eq. (2.3), we can write the induced polarization as

$$\vec{P} = \vec{P}^{(1)} + \vec{P}^{NL} \quad (2.4)$$

where  $\vec{P}^{(1)}$  and  $\vec{P}^{NL}$  represent the linear and nonlinear response of the medium, respectively. Using Eq. (2.4) in Eq. (2.1) we have

$$\begin{aligned}\nabla^2 \vec{E} - \mu_0 \epsilon_0 \frac{\partial^2 \vec{E}}{\partial t^2} &= \mu_0 \frac{\partial^2}{\partial t^2} (\vec{P}^{(1)} + \vec{P}^{NL}) \\ \nabla^2 \vec{E} - \mu_0 \epsilon_0 \frac{\partial^2 \vec{E}}{\partial t^2} - \mu_0 \frac{\partial^2}{\partial t^2} (\epsilon_0 \vec{\chi}^{(1)} : \vec{E}) &= \mu_0 \frac{\partial^2}{\partial t^2} \vec{P}^{NL}\end{aligned}\quad (2.5)$$

For an isotropic medium, the linear electric susceptibility is a scalar quantity,  $\chi$ . Therefore, using that  $c^2 = 1/\mu_0 \epsilon_0$  and  $\epsilon^{(1)} = 1 + \chi^{(1)}$  one can obtain

$$\nabla^2 \vec{E} - \frac{\epsilon^{(1)}}{c^2} \frac{\partial^2 \vec{E}}{\partial t^2} = \frac{1}{\epsilon_0 c^2} \frac{\partial^2}{\partial t^2} \vec{P}^{NL}\quad (2.6)$$

where  $c$  is the speed of light in vacuum and  $\epsilon^{(1)}$  is the dielectric constant.

We can see from Eq. (2.6) that the nonlinear response acts as a source term and, in the absence of this term, the Eq. (2.6) presents solutions of the form of free waves with velocity  $v = c/n$ , where  $n$  is the refractive index of the medium,  $n = \sqrt{\epsilon}$ .

In nonlinear optical process we can have waves at the same frequency (degenerated) or at different frequencies (nondegenerated) propagating in the medium. Then, for a dispersive media,  $\epsilon^{(1)} = \epsilon^{(1)}(\omega)$ , we must take into account each frequency separately. In this case, we can write the electric field and nonlinear polarization using the superposition principle:

$$\vec{E}(\vec{r}, t) = \sum_n \vec{E}_n(\vec{r}, t) = \sum_n \vec{E}_n(\vec{r}) e^{-i\omega_n t} + c. c. \quad (2.7a)$$

$$\vec{P}^{NL}(\vec{r}, t) = \sum_n \vec{P}_n^{NL}(\vec{r}, t) = \sum_n \vec{P}_n^{NL}(\vec{r}) e^{-i\omega_n t} + c. c. \quad (2.7b)$$

When Eqs. (2.7a) and (2.7b) are introduced into Eq. (2.6), we obtain a wave equation for each frequency:

$$\nabla^2 \vec{E}_n(\vec{r}, t) - \frac{\epsilon^{(1)}(\omega_n)}{c^2} \frac{\partial^2}{\partial t^2} \vec{E}_n(\vec{r}, t) = \frac{1}{\epsilon_0 c^2} \frac{\partial^2}{\partial t^2} \vec{P}_n^{NL}(\vec{r}, t) \quad (2.8)$$

In practice, the excitation radiation usually comes from laser beams with Gaussian transverse intensity profile and, in this way, it is interesting to express the Laplace operator in cylindrical coordinates:

$$\nabla^2 = \frac{\partial^2}{\partial z^2} + \nabla_{\text{T}}^2 \quad (2.9)$$

where

$$\nabla_{\text{T}}^2 = \frac{1}{r} \frac{\partial}{\partial r} \left( r \frac{\partial}{\partial r} \right) + \frac{1}{r^2} \frac{\partial^2}{\partial \phi^2} \quad (2.10)$$

is the transverse Laplacian in cylindrical coordinates, and we are assuming the propagation in the  $z$  direction. Also, in this case, the amplitudes of  $\vec{E}$  and  $\vec{P}$  should vary spatially,

$$\vec{E}_n(\vec{r}, t) = \vec{A}_n(\vec{r}) e^{i(k_n z - \omega_n t)} + c. c. \quad (2.11a)$$

$$\vec{P}_n^{NL}(\vec{r}, t) = \vec{p}_n(\vec{r}) e^{i(k'_n z - \omega_n t)} + c. c. \quad (2.11b)$$

where  $k = \omega n/c$  is the wave vector and  $\vec{A}_n(\vec{r})$  and  $\vec{p}_n(\vec{r})$  are the complex amplitudes of the electric field and polarization, respectively. We can next substitute Eqs. (2.11a) and (2.11b) into (2.8), and use the Laplace operator given by Eqs. (2.9) and (2.10), to obtain:

$$\begin{aligned} & \left[ \frac{\partial^2}{\partial z^2} \vec{A}_n(\vec{r}) + 2ik_n \frac{\partial}{\partial z} \vec{A}_n(\vec{r}) + \left( \frac{\epsilon^{(1)}(\omega_n) \omega_n^2}{c^2} - k_n^2 \right) \vec{A}_n(\vec{r}) + \nabla_{\text{T}}^2 \vec{A}_n(\vec{r}) \right] e^{i(k_n z - \omega_n t)} \\ & = \frac{-\omega_n^2}{\epsilon_0 c^2} \vec{p}_n(\vec{r}) e^{i(k'_n z - \omega_n t)}. \end{aligned} \quad (2.12)$$

Since the term in parenthesis on left side of Eq. (2.12) is equal to zero we can rewrite the equation as follows:

$$\frac{\partial^2}{\partial z^2} \vec{A}_n(\vec{r}) + 2ik_n \frac{\partial}{\partial z} \vec{A}_n(\vec{r}) + \nabla_{\text{T}}^2 \vec{A}_n(\vec{r}) = \frac{-\omega_n^2}{\epsilon_0 c^2} \vec{p}_n(\vec{r}) e^{i\Delta k z} \quad (2.13)$$

with  $\Delta k = k'_n - k_n$ .

In most practical cases of interest, the spectrum amplitude is centered at a frequency  $\omega$  and we have appreciable values of the electric field in a frequency interval  $\Delta\omega$ , which is small compared to  $\omega$ ,  $\Delta\omega \ll \omega$ . Also, the change in amplitude of the wave in a distance of the order of an optical wavelength is much smaller than unity. In this case, we can consider the approximation known as SVEA (*slowly varying envelope approximation*)<sup>10,29-30</sup>

$$\left| \frac{\partial^2}{\partial z^2} \vec{A}_n(\vec{r}) \right| \ll \left| k_n \frac{\partial}{\partial z} \vec{A}_n(\vec{r}) \right| \quad (2.14)$$

and the theoretical description of pulse propagation is simplified because we can neglect the first term on left side of Eq. (2.13) and obtain

$$2ik_n \frac{\partial}{\partial z} \vec{A}_n(\vec{r}) + \nabla_{\perp}^2 \vec{A}_n(\vec{r}) = \frac{-\omega_n^2}{\varepsilon_0 c^2} \vec{p}_n(\vec{r}) e^{i\Delta k z}. \quad (2.15)$$

Equation (2.15) is easier to be solved than (2.13) and we are interested in determining its solution for the case of Gaussian beams, that is,  $\vec{A}_n(\vec{r})$  and  $\vec{p}_n(\vec{r})$  should vary spatially according to a Gaussian distribution. Then, we shall firstly introduce the Gaussian waves.

## 2.1 Gaussian beams

The most used optical beam is that one where the intensity distribution at planes normal to the propagation direction is Gaussian.<sup>31</sup> In this case, the amplitude of the electric field can be represented as

$$A(r, z) = \mathcal{A} \frac{w_0}{w(z)} e^{-r^2/w^2(z)} e^{i \left[ \frac{kr^2}{2R(z)} - \eta(z) \right]}. \quad (2.16)$$

where we are assuming the propagation in the  $z$  direction. One can notice from Eq. (2.16) that the field amplitude decreases exponentially as the radial coordinate magnitude increases, Fig. 2.1.  $w(z)$  is the beam waist radius and it is one of the most important parameters of a Gaussian beam,<sup>32</sup> it can be expressed by

$$w^2(z) = \frac{2z_r}{k} [1 + (z/z_r)^2] = w_0^2 [1 + (z/z_r)^2] \quad (2.17)$$

where  $w_0$  represents its value at  $z = 0$ , and  $z_r$  is the Rayleigh range (or Rayleigh length).  $z_r$  corresponds to the distance in the  $z$  direction from the focal point where the width of the beam is  $\sqrt{2}$  larger than it is at  $z = 0$ , that is,  $w(z_r) = \sqrt{2}w_0$ . Usually, it is within the confocal parameter,  $2z_r$ , that the nonlinear effects significantly take place because it corresponds to the range where the beam intensity is high enough.

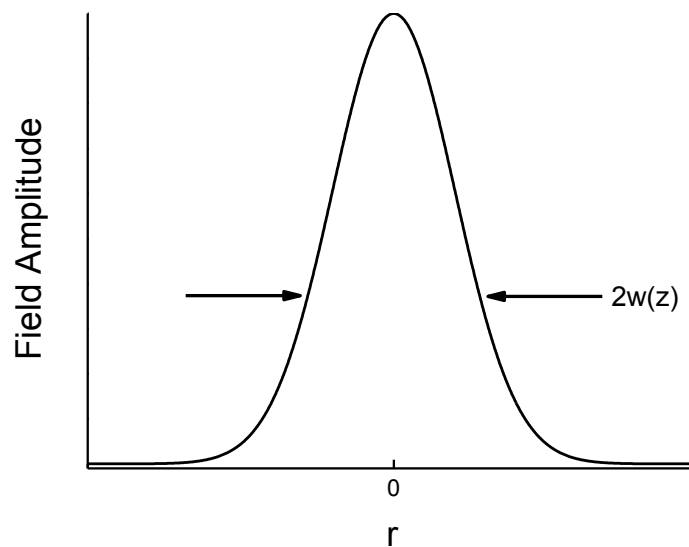


Figure 2.1 – Field amplitude distribution for a Gaussian laser beam.  
Source: By the author.

We can see from Eq. (2.17) that  $w_0$  and  $z_r$  are related by

$$z_r = \frac{kw_0^2}{2} = \pi n w_0^2 / \lambda \quad (2.18)$$

where  $n$  is the linear refractive index and  $\lambda$  is the wavelength.

In Eq. (2.16) we also have other parameters such as the wavefront radius of curvature  $R(z)$  and the Gouy phase  $\eta(z)$ ,

$$R(z) = z[1 + (z_r/z)^2] \quad (2.19)$$

$$\eta(z) = \arctan(z/z_r) \quad (2.20)$$

The radius of curvature has an infinity value at  $z = 0$  and  $z \rightarrow \infty$ , and it is minimum at  $z = \pm z_r$ . It changes as a function of  $z$  as illustrated in Fig. 2.2. The Gouy phase  $\eta(z)$  represents the spatial variation of the phase of the wave. One can see from Eq. (2.17) that, for  $z$  much larger than  $z_r$ ,  $w(z)$  tends to  $w_0 z/z_r$ . Using Eq. (2.18) we have

$$\frac{w(z)}{z} = \frac{\lambda}{\pi n w_0} = \tan(\theta) \approx \theta \quad (2.21)$$

where  $\theta$  is the far-field divergence angle.

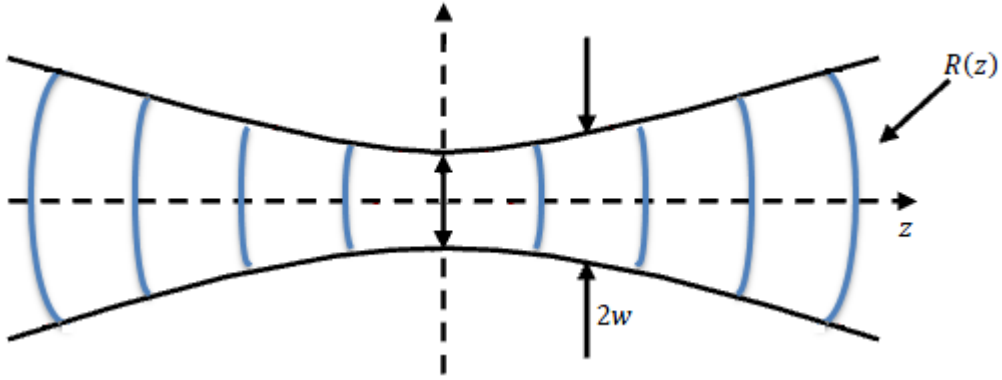


Figure 2.2 – Representation of the beam waist and wavefront radius of curvature behavior during the propagation of a Gaussian beam.

Source: Adapted from ZILIO.<sup>33</sup>

## 2.2 Harmonic generation using focused Gaussian beams

Nonlinear optical processes usually require high radiation intensity and, in order to achieve this regime, the laser beams are normally focused inside the medium. This is the case of harmonic generation for instance. We are going to develop in this section the theoretical foundations of harmonic generation using focused Gaussian laser beams. We shall follow the same approach used by Boyd<sup>10</sup> and for the theoretical work we are going to represent the Gaussian beam in a more compact form which is more convenient:

$$A(r, z) = \frac{\mathcal{A}}{1 + i\xi} e^{-r^2/w_0^2(1+i\xi)} \quad (2.22)$$

where

$$\xi = z/z_r = 2z/b. \quad (2.23)$$

Equation (2.22) is equivalent to Eq. (2.16) but it is easier to work due to the more compact form (although less intuitive). In Eq. (2.23),  $b = 2z_r$  is the confocal parameter.

According to Eq. (2.15), the amplitude  $A_q$  of the field component at frequency  $\omega_q = q\omega$  must follow

$$2ik_q \frac{\partial}{\partial z} A_q + \nabla_{\perp}^2 A_q = \frac{-\omega_q^2}{\epsilon_0 c^2} p_q e^{i\Delta k z} \quad (2.24)$$

where  $\Delta k = qk_1 - k_q$ . Now, using that  $p_q = \epsilon_0 \chi^{(q)} A_1^q$  we have

$$2ik_q \frac{\partial}{\partial z} A_q + \nabla_{\perp}^2 A_q = \frac{-\omega_q^2}{c^2} \chi^{(q)} A_1^q e^{i\Delta k z} \quad (2.25)$$

where  $\chi^{(q)}$  is the nonlinear optical susceptibility which describes the harmonic generation of order  $q$ , and  $A_1$  is the complex amplitude of the fundamental wave, that is,

$$A_1(r, z) = \frac{\mathcal{A}_1}{1 + i\xi} e^{-r^2/w_0^2(1+i\xi)}. \quad (2.26)$$

It is important to point out that we are assuming the interaction occurs sufficiently far from resonance bands of the material and, in this way, we can consider the susceptibility  $\chi$  independent of  $\omega$ .

Kleinman et al.<sup>34</sup> studied Eq. (2.25) and presented solution for second-harmonic generation (SHG) and, later, Ward and New<sup>35</sup> obtained solution for a general case for harmonic generation of order  $q$ . We can solve Eq. (2.25) adopting the trial solution

$$A_q(r, z) = \frac{\mathcal{A}_q(z)}{1 + i\xi} e^{-qr^2/w_0^2(1+i\xi)}, \quad (2.27)$$

which presents the same radial dependence of the source term in Eq. (2.25), and corresponds to a harmonic beam with the same confocal parameter as the fundamental beam. Now, we can

substitute Eqs. (2.26) and (2.27) into Eq. (2.25) and verify the trial solution satisfies the equation since  $\mathcal{A}_q(z)$  obeys the differential equation:<sup>10,36</sup>

$$\frac{d\mathcal{A}_q}{dz} = \frac{iq\omega}{2n_q c} \chi^{(q)} \mathcal{A}_1^q \frac{e^{i\Delta k z}}{(1+i\xi)^{q-1}} \quad (2.28)$$

which integrating directly leads to

$$\mathcal{A}_q(z) = \frac{iq\omega}{2n_q c} \chi^{(q)} \mathcal{A}_1^q \int_{z_e}^z \frac{e^{i\Delta k z'} dz'}{(1+2iz'/b)^{q-1}} \quad (2.29)$$

where  $z_e$  is the value of  $z$  at the entrance of the medium.

The integral in Eq. (2.29) is the *phase-matching* integral:<sup>37</sup>

$$J_q(\Delta k, z_e, z) = \int_{z_e}^z \frac{e^{i\Delta k z'} dz'}{(1+2iz'/b)^{q-1}} \quad (2.30)$$

In the case of  $b \gg |z_e|, |z|$  which is the plane-wave limit,

$$J_q(\Delta k, z_e, z) = \int_{z_e}^z e^{i\Delta k z'} dz' = \frac{e^{i\Delta k z} - e^{i\Delta k z_e}}{i\Delta k}. \quad (2.31)$$

Comparing Eqs. (2.30) and (2.31) one can conclude that the denominator in the integrand, Eq. (2.30), is the term that takes into account the focusing.

The harmonic irradiance is given by the time-averaged magnitude of the Poynting vector, which according to our definition to the electric field is:

$$I_q = 2n_q \varepsilon_0 c |A_q|^2. \quad (2.32)$$

Therefore,

$$I_q \propto (I_1^q) |J_q(\Delta k, z_e, z)|^2 = (I_1^q) L^2 \text{sinc}^2 \left( \frac{\Delta k L}{2} \right) \quad (2.33)$$

where  $L = z - z_e$  is the length of the interaction and  $I_1$  is the fundamental beam irradiance (beam at frequency  $\omega$ ). Figure 2.3 illustrates  $I_q$  as a function of  $\Delta kL/2$ . The first minimum occurs for  $\Delta kL/2 = \pi$  and one usually defines

$$L_c = 2\pi/\Delta k \quad (2.34)$$

where  $L_c$  is called coherent length. The most efficient condition for the conversion of the input fields into the harmonic is when  $\Delta k = 0$  and occurs perfect phase matching.

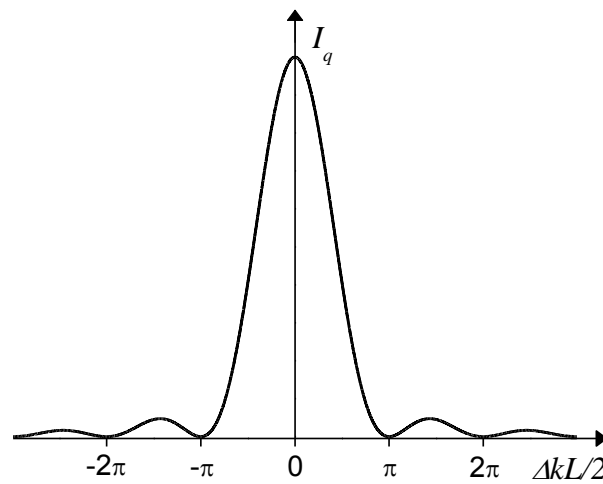


Figure 2.3 – Harmonic generation efficiency as a function of  $\Delta kL/2$ .  
Source: Adapted from BOYD.<sup>10</sup>

The behavior predicted by Eq. (2.33) was experimentally observed for the first time by Maker et al.<sup>38</sup> In their experiment, they focused a pulsed ruby laser into a crystal of quartz and measured the SHG as a function of the incident angle of the beam. By rotating the crystal, the effective path length varies and, consequently,  $\Delta kL/2$ , resulting in an interference pattern. Today, this pattern is known as Maker fringes.<sup>39-41</sup> Figure 2.4 illustrates this effect.

The other case for Eq. (2.30) is that where  $b \ll |z_e|, |z|$  which corresponds to beam focused tightly within the medium. This condition implies that  $z_e = -|z_e|$  and  $z = |z|$ . Since the beam is focused tightly inside the medium, we can use the approximation where the limits of integration are minus and plus infinity,

$$J_q(\Delta k, b, q) = \int_{-\infty}^{\infty} \frac{e^{i\Delta kz'} dz'}{(1 + 2iz'/b)^{q-1}} \quad (2.35)$$

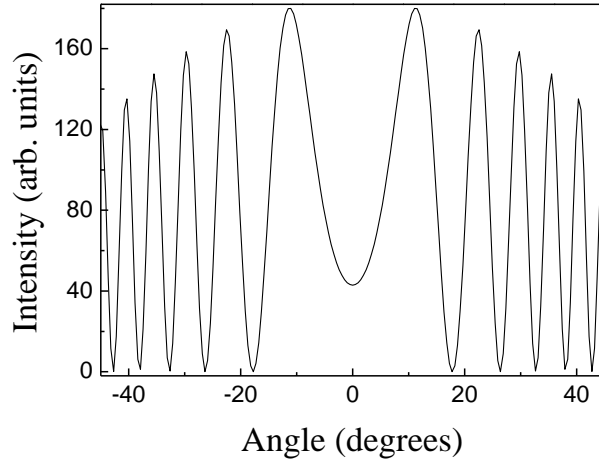


Figure 2.4 – Maker fringes pattern for the harmonic generated in plane-wave limit.  
Source: By the author.

The integral in Eq. (2.35) can be evaluated using the contour integration method, and the result is

$$J_q(\Delta k, b, q) = \begin{cases} 0, & \Delta k \leq 0 \\ \frac{\pi b}{(q-2)!} \left(\frac{b\Delta k}{2}\right)^{q-2} e^{-b\Delta k/2}, & \Delta k > 0 \end{cases} \quad (2.36)$$

In this dissertation we are especially interested in the solution when  $q = 3$ , that is, the third-harmonic generation case. THG phenomenon can be understood in the quantum description as a process in which three photons of frequency  $\omega$  are destroyed creating a simple photon at three times the frequency,  $3\omega$ . For  $q = 3$  the Eq. (2.36) becomes

$$J_3(\Delta k, b) = \begin{cases} 0, & \Delta k \leq 0 \\ \frac{\pi b^2 \Delta k}{2} e^{-b\Delta k/2}, & \Delta k > 0 \end{cases} \quad (2.37)$$

Figure (2.5) illustrates the dependence of the phase-matching factor for the THG case.

One can see there is a clear difference between the two regimes we discussed the Eq. (2.30). For  $\Delta k = 0$ , in the plane-wave condition, the harmonic generation reaches its maximum, while in the tightly focused laser beam condition there is no harmonic generation. This behavior is related to the Gouy phase shift of  $\pi$  radians the Gaussian beam experiences when passing through the focus position and, this effect is three times higher for the third-

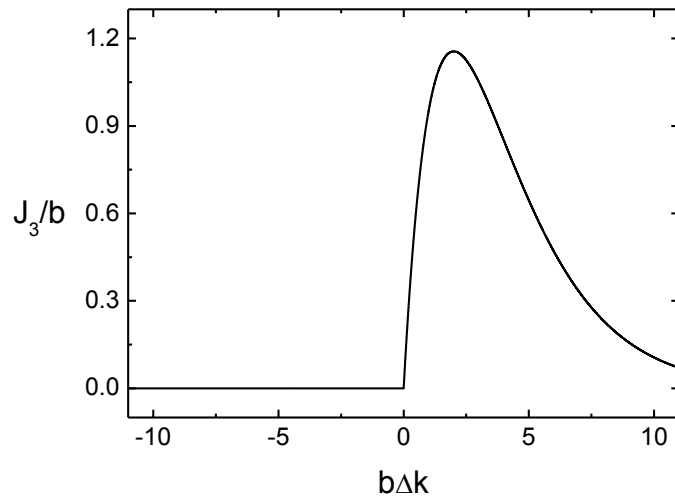


Figure 2.5 – Phase matching integral dependence with  $b\Delta k$  for THG.  
Source: By the author.

order polarization compared to the fundamental beam,<sup>42</sup> Fig. 2.6. There is an intrinsic opposite phase difference between the TH generated before and after the focal plane. Consequently, a wave vector mismatch  $\Delta k$  is necessary to compensate this phase shift and generate TH.<sup>43</sup> A theoretical analysis of third-order nonlinear interactions, for focused laser beams, which gives more information about this can be found in Bjorklund's paper.<sup>11</sup> Also, one can find alternative explanation<sup>44</sup> or new research<sup>45</sup> related to the Gouy phase shift. The understanding of why a positive value of  $\Delta k$  is desirable for harmonic generation is also possible by considering the argument presented in Fig. 2.7.

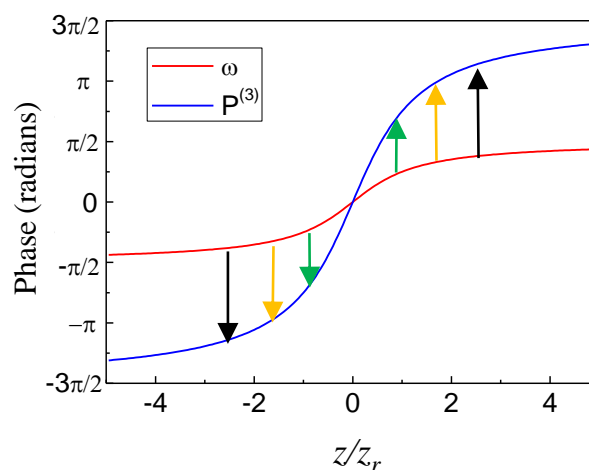


Figure 2.6 – Gouy phase shift.  
Source: Adapted from REINTJES.<sup>42</sup>

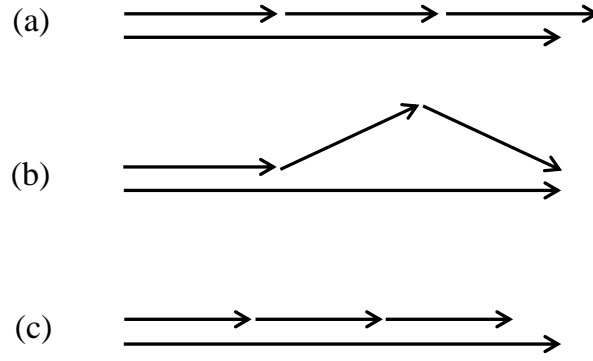


Figure 2.7 – Wavevector diagram for third-harmonic generation. For  $\Delta k$  positive, (a), due to angular spread of the fundamental beam wavevectors, (b), it is possible to obtain the phase-matched condition while for  $\Delta k$  negative, (c), THG cannot occur efficiently.

Source: Adapted from BOYD.<sup>10</sup>

Equation (2.37) shows that TH vanishes for laser beam focused tightly within media with normal dispersion,  $J_3(b\Delta k \leq 0, -\infty, +\infty) = 0$ . Now, consider the laser beam is focused at the interface between two media at  $z = 0$  so that the pre-focus medium,  $\chi_{pre}^{(3)}$ , occupies the region from  $z = -\infty$  to 0 and the post-focus medium,  $\chi_{post}^{(3)}$ , occupies the region from  $z = 0$  to  $+\infty$ . In this case,

$$I^{(3\omega)} \propto \left| J_3(b\Delta k_{pre}, -\infty, 0)\chi_{pre}^{(3)} + J_3(b\Delta k_{post}, 0, +\infty)\chi_{post}^{(3)} \right|^2 [I^{(\omega)}]^3 \quad (2.38)$$

Since, for  $b\Delta k \leq 0$ ,  $J_3(b\Delta k, -\infty, +\infty) = J_3(b\Delta k, -\infty, 0) + J_3(b\Delta k, 0, +\infty) = 0$ , one finds that

$$J_3(b\Delta k, -\infty, 0) = -J_3(b\Delta k, 0, +\infty) \quad (2.39)$$

Therefore, it is possible to say by Eq. (2.38), for  $b\Delta k \leq 0$ , that

$$I^{(3\omega)} \propto \left| (J_3 \cdot \chi^{(3)})_{post} - (J_3 \cdot \chi^{(3)})_{pre} \right|^2 [I^{(\omega)}]^3 \quad (2.40)$$

with

$$J_3 = \int_0^\infty \frac{e^{i\Delta kz}}{(1 + 2iz/b)^2} dz, \quad (2.41)$$

As a result of Eq. (2.40), THG is possible for  $b\Delta k \leq 0$  (media with normal dispersion) when the laser beam is focused at the interface between two media with different cubic nonlinearity or phase mismatch. This condition of THG at interfaces, when working in the tightly focused beam regime, is one of the most important TH properties we are going to use in this dissertation.

It is also important to mention that although, in this chapter, the polarization state of the field was not taken into account in the theoretical development for harmonic generation, such consideration would lead to a more general result which presents a significant consequence: there is no THG from a circularly polarized fundamental beam in an isotropic medium. This is related to the symmetry properties of the third-order susceptibility tensor elements and the electric field components<sup>42</sup> and, it is normally useful in order to suppress unwanted nonlinear processes when two or more effects can occur simultaneously.



### 3 NONLINEAR REFRACTIVE INDEX AND SELF-FOCUSING EFFECT

We discussed in Chapter 2 how the induced polarization can be expressed in the situation in which a medium interacts with an intense electric field, Eq. (2.3), and, how this polarization may lead to harmonic generation. Now, we are going to present the optical Kerr lens, another effect that arises from this nonlinear light-matter interaction. The optical Kerr lens is a change in the refractive index of the material in response to an intense electric field. This refractive index variation may lead to other phenomena such as self-focusing and self-phase modulation, for instance.<sup>10</sup> The self-focusing is especially important for the subject of this dissertation and, in this way, we are going to derive the irradiance-dependent refractive index (Kerr lens relationship) and briefly discuss the self-focusing effect in this section.

#### 3.1 Nonlinear refractive index

Let us consider the simple case where the electric field is monochromatic and can be represented as

$$E(t) = E_0 \cos(\omega t). \quad (3.1)$$

Using Eq. (3.1) in Eq. (2.3) we obtain:

$$P = \varepsilon_0 \chi^{(1)} E_0 \cos(\omega t) + \varepsilon_0 \chi^{(2)} E_0^2 \cos^2(\omega t) + \varepsilon_0 \chi^{(3)} E_0^3 \cos^3(\omega t) \quad (3.2)$$

where it is possible to show by trigonometric identities that:

$$P = \varepsilon_0 \chi^{(1)} E_0 \cos(\omega t) + \frac{1}{2} \varepsilon_0 \chi^{(2)} E_0^2 [1 + \cos(2\omega t)] \\ + \varepsilon_0 \chi^{(3)} E_0^3 \left[ \frac{3}{4} \cos(\omega t) + \frac{1}{4} \cos(3\omega t) \right]. \quad (3.3)$$

One can see from Eq. (3.3) the rise of a host of optical phenomena. The first term is the already known linear response of the material by the presence of light (the material's response to the applied optical field is linear with the strength of the applied optical field). The second term presents the second-order polarization  $P^{(2)}$  where we have two

contributions, a constant one and another one at the frequency  $2\omega$ . The first contribution (at zero frequency) is a process known as optical rectification, which is a static electric field created across the nonlinear medium, and the second one (at  $2\omega$ ) is related to the second-harmonic generation (SHG) process. It is important to point out that we are considering a simple case in which the applied electric field is monochromatic. For the general case in which the field is made up of several frequency components, the second-order polarization is related to even more process such as sum-frequency generation (SFG) and difference-frequency generation (DFG).<sup>10</sup> Here, the monochromatic approach is interesting since the expression for the third-order contribution to the nonlinear polarization [last term in Eq. (3.3)] is very complicated for the general case. The third-order contribution in Eq. (3.3) describes a nonlinear response to the polarization at the frequency of the input electric field and another one at frequency  $3\omega$  that leads to the process of third-harmonic generation.

Equation (3.3) shows the second-order effects depend on  $\chi^{(2)}$  while the third-order effects depend on  $\chi^{(3)}$ . For centrosymmetric materials, the response of the induced polarization to an external electric field must respect the relation  $P(-E) = -P(E)$ , that is, when the electric field is reversed, the polarization remains its magnitude but is opposite to the field.<sup>46</sup> Consequently, for centrosymmetric materials, all nonlinear susceptibilities of even powers of  $E$ ,  $\chi^{(2)}$ ,  $\chi^{(4)}$ , etc., have to be equal to zero and the nonlinear effects related to  $\chi^{(3)}$  are the most important. Therefore, in this case, the induced polarization can be written as:

$$P = \varepsilon_0 \chi^{(1)} E_0 \cos(\omega t) + \varepsilon_0 \chi^{(3)} E_0^3 \left[ \frac{3}{4} \cos(\omega t) + \frac{1}{4} \cos(3\omega t) \right]. \quad (3.4)$$

From Eq. (3.4) we see the part of the polarization which influences the propagation of the beam at frequency  $\omega$  is

$$P(\omega) = \varepsilon_0 \chi^{(1)} E_0 \cos(\omega t) + \frac{3}{4} \varepsilon_0 \chi^{(3)} E_0^3 \cos(\omega t) \quad (3.5a)$$

$$P(\omega) = \varepsilon_0 \left[ \chi^{(1)} + \frac{3}{4} \chi^{(3)} E_0^2 \right] E(t). \quad (3.5b)$$

Taking into account the wave equation for a beam that propagates at  $z$  direction,

$$\frac{\partial^2 E}{\partial z^2} - \mu_0 \varepsilon_0 \frac{\partial^2 E}{\partial t^2} = \mu_0 \frac{\partial^2 P}{\partial t^2} \quad (3.6)$$

we have

$$\begin{aligned} \frac{\partial^2 E}{\partial z^2} - \mu_0 \varepsilon_0 \frac{\partial^2 E}{\partial t^2} - \mu_0 \varepsilon_0 \left[ \chi^{(1)} + \frac{3}{4} \chi^{(3)} E_0^2 \right] \frac{\partial^2 E}{\partial t^2} &= 0 \\ \frac{\partial^2 E}{\partial z^2} - \mu_0 \varepsilon_0 \left[ 1 + \chi^{(1)} + \frac{3}{4} \chi^{(3)} E_0^2 \right] \frac{\partial^2 E}{\partial t^2} &= 0. \end{aligned} \quad (3.7)$$

In this way, we can say from Eq. (3.7) that:

$$\frac{1}{v^2} = \mu_0 \varepsilon_0 \left[ 1 + \chi^{(1)} + \frac{3}{4} \chi^{(3)} E_0^2 \right] \quad (3.8)$$

where  $v$  is the speed of light in the medium. Using  $c^2 = 1/\mu_0 \varepsilon_0$ , we obtain

$$\left( \frac{c}{v} \right)^2 = n^2 = 1 + \chi^{(1)} + \frac{3}{4} \chi^{(3)} E_0^2. \quad (3.9)$$

Therefore,

$$n = \sqrt{1 + \chi^{(1)}} \left[ 1 + \frac{3\chi^{(3)} E_0^2}{4(1 + \chi^{(1)})} \right]^{1/2}. \quad (3.10)$$

Here, considering the linear refractive index,  $n_0 = \sqrt{1 + \chi^{(1)}}$ , we have

$$n = n_0 \left[ 1 + \frac{3\chi^{(3)} E_0^2}{4(n_0^2)} \right]^{1/2} \approx n_0 \left[ 1 + \frac{3\chi^{(3)} E_0^2}{8(n_0^2)} \right], \quad (3.11)$$

where the approximation comes from the Taylor series expansion considering that the second term is much smaller than 1.

From the electric field definition given by Eq. (3.1), the irradiance is:

$$I = \frac{1}{2} cn_0 \varepsilon_0 E_0^2. \quad (3.12)$$

Therefore, we can use the Eq. (3.12) to express the effective refractive index as a function of  $I$ ,

$$n = n_0 + \frac{3}{4} \frac{\chi^{(3)}}{cn_0^2 \varepsilon_0} I. \quad (3.13)$$

An alternative way (and more commonly used) of defining the irradiance-dependent refractive index is

$$n = n_0 + n_2 I \quad (3.14)$$

where  $n_2$  is the material nonlinear refractive index. Then, in the SI system of units:

$$n_2 = \frac{3}{4} \frac{\chi^{(3)}}{cn_0^2 \varepsilon_0} \quad (3.15)$$

One can see from Eq. (3.14) that the refractive index depends on the irradiance of the light. Usually,  $n_2$  values are relatively small, typical values are of the order of  $10^{-20} \text{ m}^2/\text{W}$  for common optical glasses.

### 3.2 Self-focusing of light

Self-focusing effect is a consequence of the nonlinear refractive index. Briefly, it can be thought as an induced lens due to the nonlinear interaction between light and matter. The self-focusing process is illustrated schematically in Fig. 3.1. Considering a medium whose refractive index is given by Eq. (3.14), with positive  $n_2$ , and a laser beam with Gaussian transverse intensity profile,  $I = I(r)$ , propagating into this medium, we have

$$n(r) = n_0 + n_2 I(r). \quad (3.16)$$

In this case, the laser beam induces a refractive index variation in such a manner that the beam is caused to come to a focus.<sup>10,47</sup> The effective refractive index is larger at the center

of the beam than at its borders, the beam is slowed at the center in comparison to the edge and, the material acts as a positive lens. For negative  $n_2$ , the material presents a reduced refractive index on the beam axis and it acts as if it were a negative lens, self-defocusing.

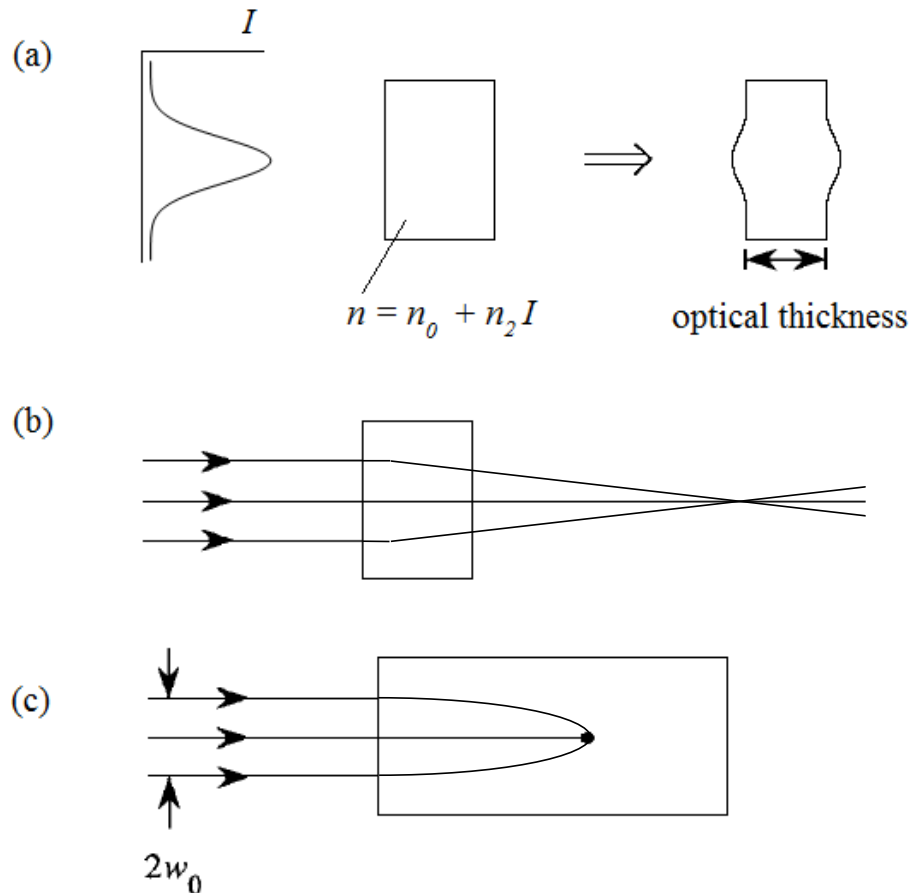


Figure 3.1 – Self-focusing of light. As a result of the nonlinear interaction the material behaves as if it had larger optical thickness at the center of the beam (a). For a material short enough, the focal plane will be outside of the medium (b), however, for a material sufficiently long or beam intensity sufficiently large, the focal plane will occur within the medium (c).

Source: Adapted from BOYD.<sup>48</sup>

There are different physical mechanisms that can produce an irradiance-dependent refractive index such as electronic polarization, electrostriction and thermal effects.<sup>49</sup> In the case we are going to study here, a short-pulse laser beam focused in solids and liquids, the responsible mechanism is the electronic polarization, also known as optical Kerr lens effect, and occurs due to electronic cloud distortion. But self-focusing has been observed for different types of materials and with many types of laser sources.<sup>50</sup> For instance, self-focusing of mode-locked laser pulses in liquid argon<sup>51</sup> and molecular gases,<sup>52</sup> pulsed dye lasers in gases due to resonant interactions<sup>53</sup> and, also, self-focusing of CW (continuous-wave) dye laser in sodium vapor has been reported.<sup>54</sup>

The self-focusing effect is a self-action phenomenon because the beam modifies its own propagation by means of the nonlinear response of the medium. As the beam propagates in the medium, the wavefront of the beam gets distorted and this distortion is similar to that imposed by a positive lens. Self-focusing is often responsible for optical damage of transparent materials. Since the propagation is perpendicular to the wavefront, the laser beam appears to focus by itself and the beam waist radius is decreased compared with that of a weak laser pulse.<sup>55</sup>

More information about self-focusing effect can be found, for example, in the books of Boyd<sup>10</sup> and Koechner.<sup>49</sup>

## 4 THIRD-HARMONIC GENERATION AT OPTICAL GLASSES INTERFACES<sup>†</sup>

In experiments where the sample is scanned along the beam propagation direction, the TH generated at the entrance and exit interfaces are different.<sup>12,56</sup> The TH generated at the exit interface is systematically stronger than one generated at the entrance. It seems worthwhile to study more carefully this phenomenon since THG is an important third-order process used in a variety of applications. In the present section we report on THG measurements, using femtosecond laser pulses, at the interfaces of several optical glasses carried out with the Z-scan technique<sup>15,57</sup> at the tightly focused laser beam condition. By controlling the sample position and laser power, we could follow the evolution of the THG intensity at both interfaces for different materials. We found the TH generated at the entrance interface follows the expected cubic power law dependence while the TH generated at the exit presents a slope higher than three. We next show how this behavior can be explained considering the self-focusing effect.

### 4.1 Methodology

To fully understanding the results that will be presented, we consider the usual THG cubic dependence on the fundamental beam irradiance:<sup>10</sup>

$$I_{sample}^{(3\omega)} \propto |\Delta\chi^{(3)}|^2 (I^{(\omega)})^3 \quad (4.1)$$

where  $I_{sample}^{(3\omega)}$  and  $I^{(\omega)}$  are the irradiances of the TH and fundamental beam, respectively.  $\Delta\chi^{(3)}$  is the difference between the third-order nonlinear susceptibility of the two materials at the interface. For the case of a single glass slab, Eq. (4.1) can be rewritten as:

$$I_{sample}^{(3\omega)} \propto \left(\chi_{sample}^{(3)}\right)^2 (I^{(\omega)})^3, \quad (4.2)$$

since the nonlinear susceptibility of air is negligible. As mentioned earlier, the THG at the entrance and exit interfaces are different and we propose the self-focusing effect explains this asymmetry. In this case, the self-focusing changes the beam waist,  $w$ , and the irradiance becomes a function of  $w$ ,

<sup>†</sup> Main results already published in Optics Letters.<sup>26</sup>

$$I_{sample}^{(3\omega)} \propto \left(\chi_{sample}^{(3)}\right)^2 \left[I^{(\omega)}(w)\right]^3. \quad (4.3)$$

Considering the beam waist radius changes with the laser power explains why the slope of the THG signal does not follow the cubic power law. In this simple model, we consider that the beam waist for a given laser power,  $P$ , depends on the sample's nonlinearity because of the self-focusing process. In the case of a positive nonlinearity, we assume that the beam radius at the exit surface is reduced to

$$w_{output} = w(P) = w_0(1 - BP) \quad (4.4)$$

where  $w_0$  is the radius without self-focusing,  $B$  is an empirical constant proportional to the sample's nonlinearity,  $n_2$ , and the product  $BP$  represents the amount of beam decrease. Since the laser irradiance is inversely proportional to the square of the beam radius

$$I \propto P/w^2 = P/[w(P)]^2, \quad (4.5)$$

we propose the following empirical equation:

$$I_{sample}^{(3\omega)} = A' \left( \frac{P}{[w_0(1 - BP)]^2} \right)^3, \quad (4.6)$$

where  $A'$  is a constant that depends on the particular sample. For our purpose here we are going to define  $A = A'/w_0^6$  and, in this way,

$$I_{sample}^{(3\omega)} = A \left[ \frac{P}{(1 - BP)^2} \right]^3, \quad (4.7)$$

The quantity  $BP$  changes the slope of the logarithmic THG intensity versus the input power curve, while  $A$  adjusts its offset.

The self-focusing of light occurs when a laser beam with a Gaussian transverse intensity profile propagates through a medium whose refractive index is given by

$$n = n_0 + n_2 I, \quad (4.8)$$

where  $n_2$  is the nonlinear refractive index proportional to  $\chi_{sample}^{(3)}$ .<sup>58</sup> For a positive nonlinearity, as is usual for the instantaneous electronic polarization of optical glasses, the refractive index is larger at the center of the laser beam than at its periphery, resulting in a positive lens whose focal length depends on the laser irradiance and sample nonlinearity.<sup>59</sup> In the Z-scan method, the interfaces translate through the laser focal plane. If the beam is tightly focused at the exit interface [Fig. 4.1 (a)], the sample is in the pre-focus region, and the nonlinear interaction occurs just in this region. On the other hand, when the beam is focused at the entrance interface [Fig. 4.1 (b)], only the post-focus region is important. It is worth mentioning that, in both cases, THG and self-focusing effects occur in a typical Rayleigh range,  $z_R$ , where the laser irradiance is strong enough to induce such nonlinear effects.

As seen in Fig. 4.1 (a), stronger THG is expected due to the reduction of the beam waist at the exit interface. Furthermore, the THG at the entrance interface is not enhanced because the self-focusing changes the beam waist just after the focus where the irradiance is smaller due to natural beam expansion.

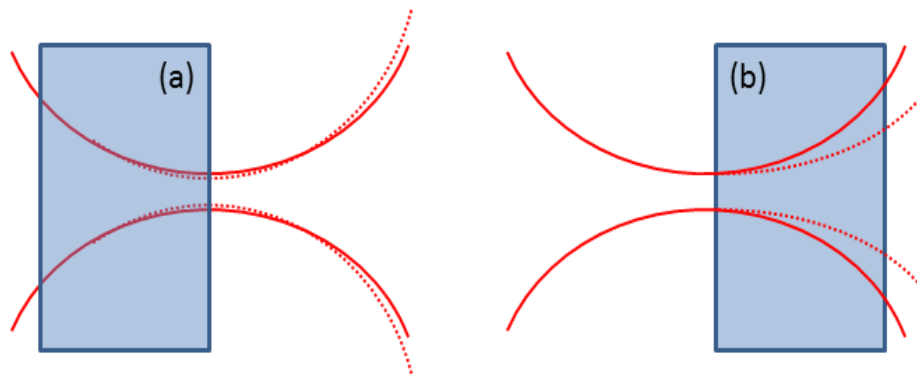


Figure 4.1 – Schematic self-focusing action represented by the dashed line for beam focused at the exit (a) and entrance (b) interfaces.

Source: BARBANO; ZILIO; MISOGUTI.<sup>26</sup>

In order to verify the validity of the model proposed, we carried out THG Z-scan measurements using a commercial optical parametric amplifier (OPA) (TOPAS, from Light Conversion), synchronously pumped by a chirped-pulse-amplified system (CPA 2001-Clark MXR) with a 775 nm central wavelength and 150 fs pulse duration at 1 kHz repetition rate. The OPA was set to generate pulses at the near IR range ( $\lambda = 1300$  nm) with about 120 fs of pulse duration. In this way, the TH is centered on 433 nm. In these wavelengths, the samples used here (silica, BK7, SK11, and F2) present no significant absorption. As the Z-scan method requires, the sample translates through the focus of the laser beam located at  $z = 0$ . Negative values of  $z$  correspond to sample positions between the focusing lens and its focal

plane such that the exit (entrance) interface appears at the negative (positive)  $z$  direction. The average laser power was carefully adjusted with a calcite polarizer in the range from 0.3 to 0.8 mW ( $I_0 \sim 2.4$  to  $6.4 \times 10^{16}$  W/m<sup>2</sup>) and was then focused with a 50 mm focal length lens ( $w_0 \approx 8 \mu\text{m}$ ) such that the Rayleigh range ( $z_r = 151 \mu\text{m}$ ) was shorter than the sample thickness, allowing us to resolve the two THG signal peaks (two interfaces). To avoid damage to the detector, we used three dichroic mirrors to separate the strong fundamental beam from the TH beam. A lens placed after the sample was used to direct most of the TH light into a large-area silicon PIN detector coupled to a lock-in amplifier, Fig. 4.2.

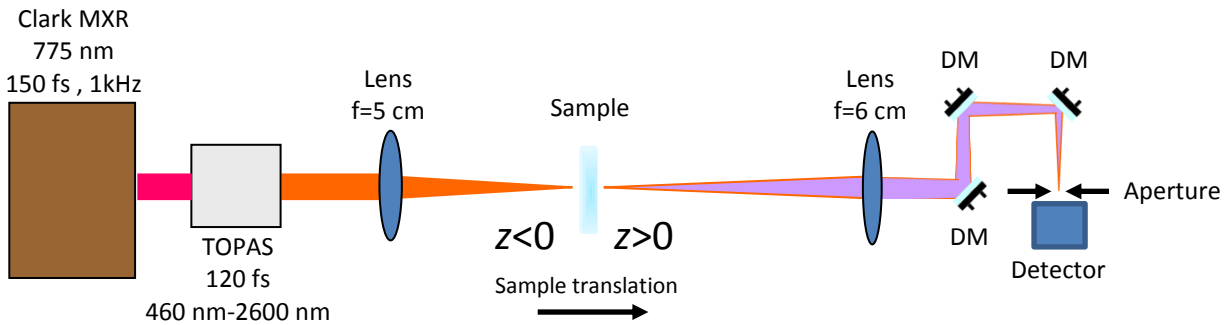


Figure 4.2 – Experimental setup for measuring the TH signal. DM, dichroic mirrors.  
Source: Adapted from BARBANO et al.<sup>27</sup>

## 4.2 Results

We have measured three optical glasses, BK7, SK11 and F2. In Table 4.1 we present their thickness and linear refractive index at 433 nm (TH wavelength) and 1300 nm (fundamental wavelength). We have used silica as a reference because it has a well-known nonlinearity,  $n_2 = 2.71 \times 10^{-20}$  m<sup>2</sup>/W.<sup>60</sup>

Table 4.1 – Optical glasses used with corresponding refractive index and thickness.

Sample	$n_0$ (433 nm)	$n_0$ (1300 nm)	thickness (mm)
Silica	1.46693	1.44692	1.225
BK7	1.52697	1.50370	0.925
SK11	1.57564	1.54965	1.155
F2	1.64271	1.59813	1.165

Source: By the author.

Figure 4.3 shows the THG curves. As it can be seen, the THG peaks generated at the exit are systematically more intense than those generated at the entrance interface for all samples measured. It is worth mentioning that although the Fig. 4.3 shows THG curves for a

fixed power (0.44 mW), this behavior was also observed for other power values, i.e., all curves exhibit a stronger peak at the exit interface (negative  $z$ ) and a smaller one at the entrance interface (positive  $z$ ) regardless of the power used. We also carried out measurements for different silica samples (with different thicknesses) and the signal was the same of that obtained here, since we worked within the thick sample condition.

Since the samples measured present different linear and nonlinear refractive indices, they can provide good insight on the working principles of the THG at interfaces. Silica and F2 have the lowest and the highest linear and nonlinear indexes of refraction, respectively, while BK7 and SK11 have intermediate values.

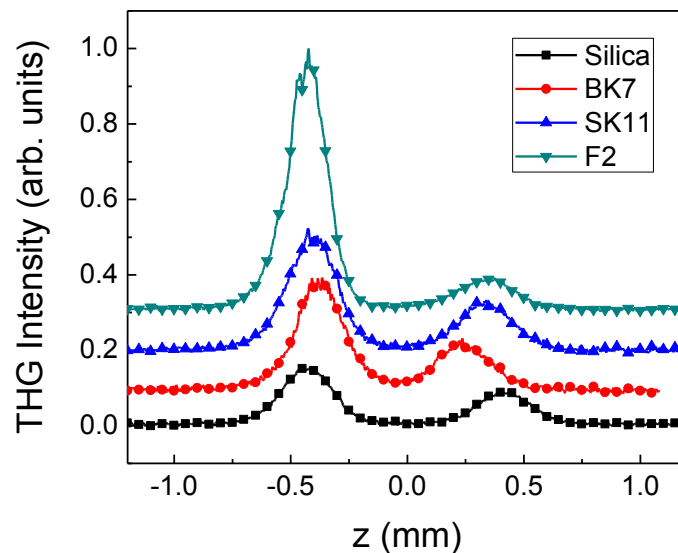


Figure 4.3 – THG Z-scan signal for silica, BK7, SK11, and F2 obtained at an average laser power of  $\sim 0.44$  mW. An offset of 0.1 between consecutive curves was introduced for better visualization.

Source: BARBANO; ZILIO; MISOGUTI.<sup>26</sup>

In Fig. 4.4 we present the normalized TH peaks generated at the entrance and exit interfaces. The normalized curves are related to the harmonics presented in Fig. 4.3. One can see clearly in Fig. 4.4 that the harmonics generated at entrance and exit interfaces exhibit different widths. The TH generated at the exit interfaces are systematically narrower than those generated at the entrance interfaces. For silica (which presents the lowest nonlinearity) the width alteration is more difficult to notice, but using a measurement tool with a higher average power, 0.8 mW ( $I_0 \approx 6.4 \times 10^{16}$  W/m<sup>2</sup>), this difference becomes evident, Fig. 4.5.

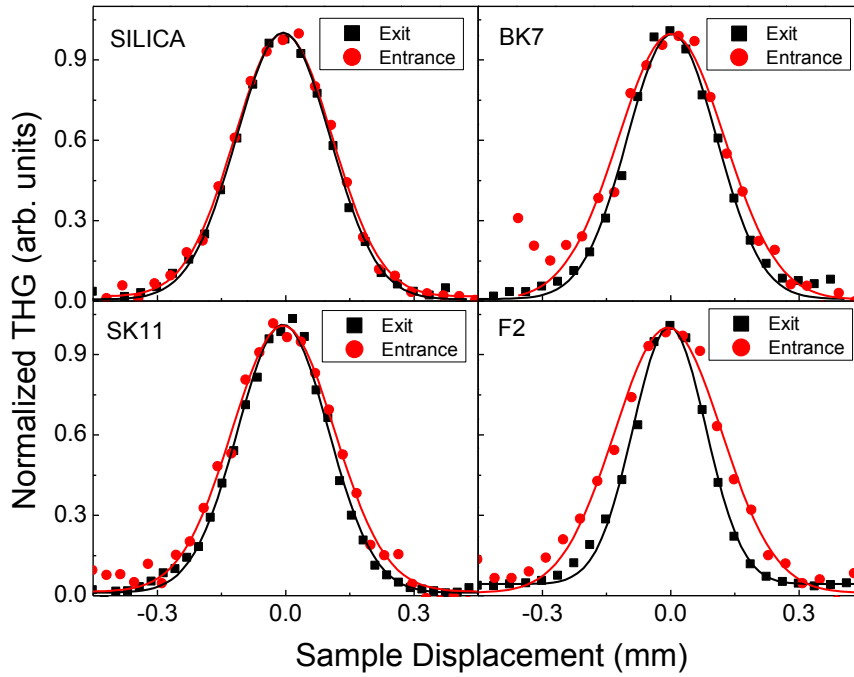


Figure 4.4 – Normalized TH peaks generated at the entrance (red) and exit (black) interfaces obtained with 0.44 mW pump power. The points are the experimental results, and the lines are fittings with Gaussian functions.

Source: By the author.

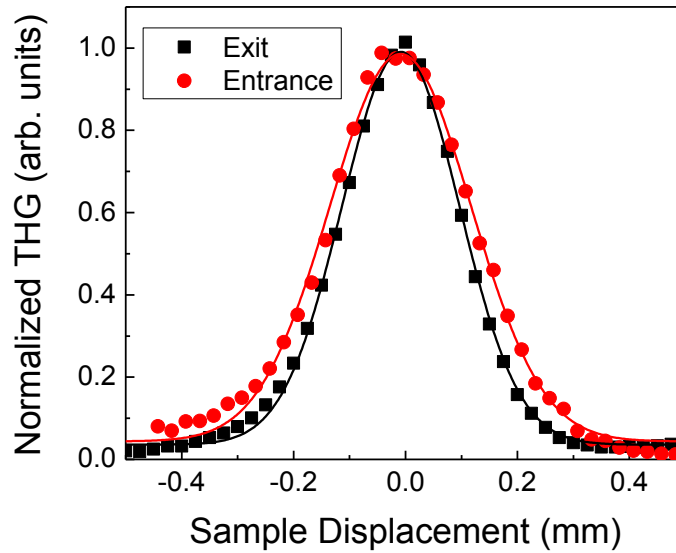


Figure 4.5 – Normalized TH peaks generated at the entrance (red) and exit (black) interfaces for silica obtained with 0.8 mW pump power. The points are the experimental results, and the lines are fittings with Gaussian functions.

Source: BARBANO; ZILIO; MISOGUTI.<sup>26</sup>

This reduction in the width indicates a change in the Rayleigh range (or Rayleigh parameter) of the Gaussian beam because it corresponds to the region where the laser beam is

strong enough to generate TH. As predicted by the Gaussian beam theory, the reduction in the Rayleigh range may be related to a beam waist radius reduction.<sup>33</sup>

We performed measurements as a function of the laser power and observed similar TH curve shapes, and so we considered only the peak values at the interfaces to establish the power law dependence through the log-log plots of Fig. 4.6. The slopes of the THG for entrance interfaces (red circles) are exactly 3 while the slopes for exit interfaces (black squares) are slightly higher than 3. The slopes were obtained by considering a linear fit in the log-log scale. As expected, F2 presents the uppermost slope because it has the highest nonlinear refractive index. The solid lines, corresponding to Eq. (4.7) of our model that takes into account the beam waist decrease, fit very well the experimental data. The fitting of the experimental data with Eq. (4.7) allows finding the sample nonlinearity using the value of silica as a reference. By comparing the relative B values of each fitting, one can estimate  $n_2$ , once the ratio  $B_{glass}/B_{silica}$  should be equal to  $n_{2,glass}/n_{2,silica}$ . Table 4.2 shows the results achieved by this procedure (THG slope).

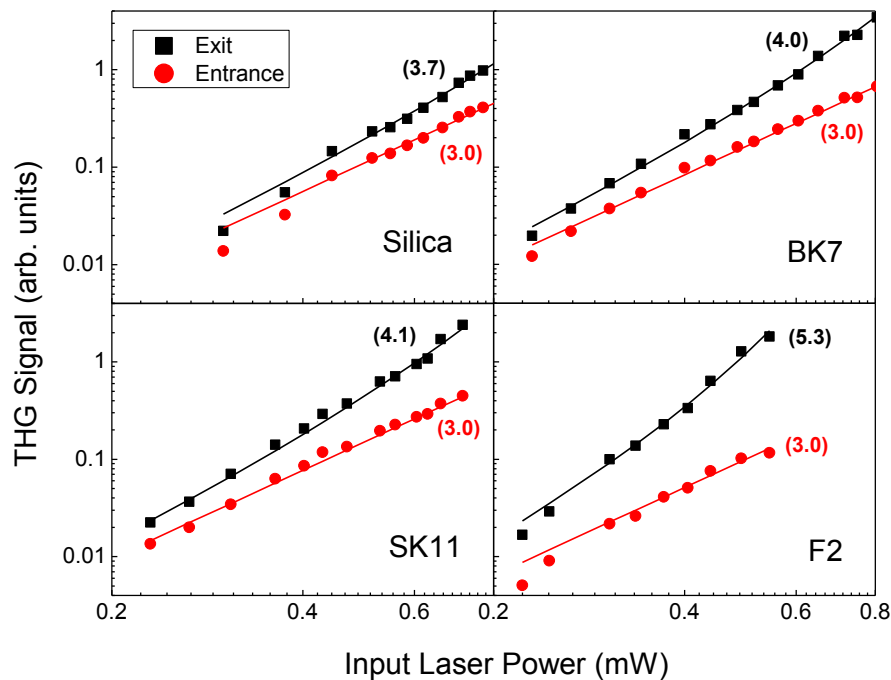


Figure 4.6 – THG peak values at the entrance (red) and exit (black) interfaces as a function of the incident laser power for silica, BK7, SK11, and F2. The symbols are the experimental data, while the solid lines are results obtained with the model proposed. The numbers in parenthesis indicate the slopes (THG dependence with laser power).

Source: BARBANO; ZILIO; MISOGUTI.<sup>26</sup>

Using the same results it is also possible to follow the confocal parameter behavior,  $2z_r$ , as a function of the input laser power. Basically, this parameter corresponds to the

Gaussian width where the intensity is  $1/e^2$  of the peak value. As the noise is significant in this part of the Gaussian curve, we have measured the full width at half maximum, FWHM, where the signal-to-noise relationship is better, and have obtained the confocal parameter by multiplying by 1.699. The results are shown in Fig. 4.7. Despite the noise in the measured widths, Fig. 4.7 shows a trend of broadening (entrance) and shortening (exit) of the THG peaks. The effect is more evident in F2 because of its high nonlinearity.

Broadening and shortening of the THG peaks are explained by the self-focusing effect as the TH is generated near the focal plane. When the nonlinear sample is placed after the focus position (entrance interface), the self-focusing effect tends to recollimate the beam, and  $z_r$  increases. On the other hand, for a sample positioned before the focal plane (exit interface),  $z_r$  decreases. The broadening of  $z_r$  at the entrance interface does not affect the fundamental laser irradiance, as most of the TH is generated near the interface, where the self-focusing did not take place yet because of the lack of beam propagation. This explains why the THG at the entrance interfaces follows the cubic power law. In the case of the exit interfaces, most of the THG occurs in the vicinity of the output face where the beam waist compression already took place due to self-focusing and propagation along the Rayleigh distance. Due to this reduction of the beam waist radius, the laser irradiance increases and leads to a THG law with an exponent greater than cubic. Such confocal parameter behavior can be understood considering the  $z_r$  dependence with  $w$ ,

$$2z_r(P) = \frac{2\pi n}{\lambda} [w(P)]^2 \quad (4.9)$$

or, using Eq. (4.4), we have

$$2z_r(P) = 2z_{r_0} (1 \pm BP)^2 \quad (4.10)$$

where  $z_{r_0}$  corresponds to the Rayleigh range in the absence of self-focusing. The positive (negative) signal is relative to the entrance (exit) interface. In Fig. 4.7, the symbols are the experimental data, while the solid lines are obtained from Eq. (4.10). With the  $B$  values obtained by these fittings we also calculated the  $n_{2_{glass}}/n_{2_{silica}}$  ratio. Table 4.2 shows the results achieved by this procedure ( $2z_r$  approach).

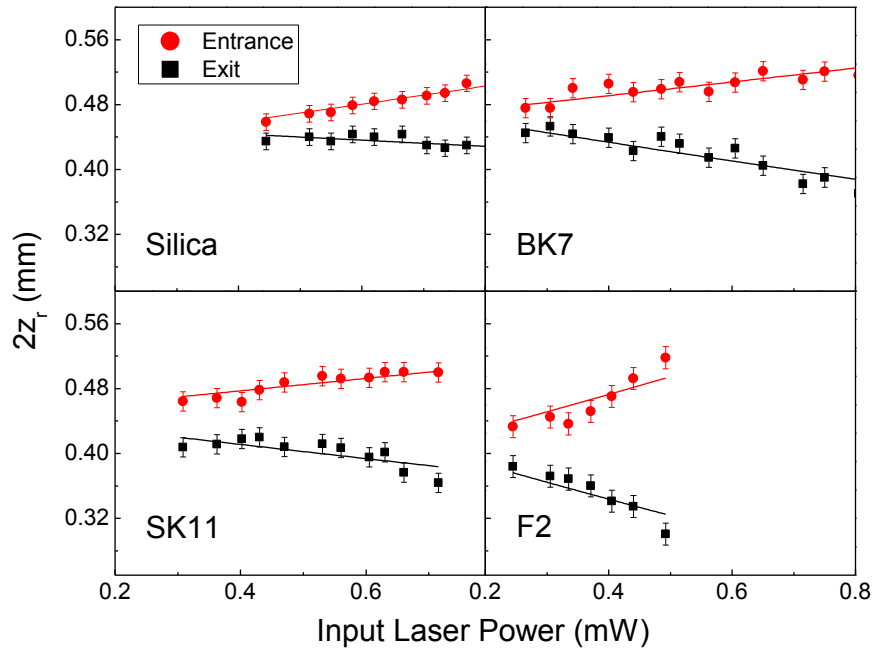


Figure 4.7 –  $2z_r$  from the TH collected as a function of the pump laser power for silica, BK7, SK11, and F2 glasses. The solid lines were obtained from Eq. (4.10).

Source: By the author.

In order to compare the measured nonlinearity, we can use the empirical expression where  $n_2$  can be theoretically derived from the linear index of refraction,  $n_e$  (at  $\lambda = 546.1$  nm) and the Abbe number,  $\nu_e$ :<sup>61-62</sup>

$$n_2(10^{-13} \text{ esu}) = \frac{68(n_e - 1)(n_e^2 + 2)^2}{\nu_e \left[ 1,517 + \frac{(n_e^2 + 2)(n_e + 1)}{6n_e} \nu_e \right]^{1/2}} \quad (4.11)$$

which can be converted to SI units according to

$$n_2(m^2/W) = \frac{4,19 \times 10^{-7}}{n_e} n_2(esu). \quad (4.12)$$

Such theoretical values of  $n_2$ , although obtained for the visible range, indicate the right trends of the nonlinearities in these four samples. Considering that there is a typical wide dispersion on the value of the nonlinearity,<sup>58,60</sup> it is possible to say that this new method used here leads to good values of the nonlinearities, and it allows making further comparison with other values obtained by other methods. Table 4.2 summarizes the results obtained by our proposed method to understand the THG at interfaces.

Table 4.2 – Theoretical and experimental  $n_2$ . The experimental values were obtained from the ratio  $B_{glass} / B_{silica}$ .

Sample	$n_e$ (546,1 nm)	$n_2$ (theory) Eqs. (4.11) e (4.12) $\times(2.53 \times 10^{-20} \text{ m}^2/\text{W})$	$n_2$ (experimental) -THG slope- $\times(2.71 \times 10^{-20} \text{ m}^2/\text{W})$	$n_2$ (experimental) -2z, approach- $\times(2.71 \times 10^{-20} \text{ m}^2/\text{W})$
Silica	1.46008	1.0	1.0	1.0
BK7	1.51872	1.3	1.7	1.3
SK11	1.56605	1.5	1.8	1.3
F2	1.62408	3.8	3.8	3.1

Source: By the author.

### 4.3 Discussion

We have studied the THG at interfaces of different optical glasses using femtosecond laser pulses. The TH intensities asymmetry could be explained by the self-focusing effect, which increases the laser irradiance at the exit interface due to the reduction of the beam waist. The beam waist radius should change as a function of sample nonlinearity and input laser power. It is important to mention that we realized the self-focusing influence by the results of Figs. 4.3, 4.4 and 4.5 and, in order to investigate more carefully this contribution, we proposed the study shown in Figs. 4.6 and 4.7. At first, we resorted to self-focusing models already available in the literature<sup>10,49</sup> but none of those correctly predict the results reported here. This is probably due to the simplifying assumptions they make such as flat-top beams or unchangeable beam waist radius at the focal plane. We proposed a simple empirical equation, Eq. (4.4), considering there is a change in the beam waist due to self-focusing where the beam waist decreases as the laser power and/or material's nonlinearity increases. Using our model we could follow the TH signal behavior as a function of the laser power and estimate the material's nonlinear refractive index.

We believe this study is important for fundamental understanding of the THG process in transparent materials at the tightly focused condition. Also, for the application's point of view, it is important for the material's third-order nonlinearity characterization and in the THG scanning laser microscopy.

## 5 THIRD-HARMONIC GENERATION AT THE INTERFACES OF A CUVETTE FILLED WITH ORGANIC SOLVENTS<sup>†</sup>

The development of new experimental procedures for a better understanding of the TH generated at surfaces is of great interest. In Chapter 4 we observed that the THG can be influenced by different nonlinear processes that drastically change the expected signal. We studied the effect of self-focusing occurring in Kerr media with nonlinear refractive index  $n_2$  (where  $n_2 \propto \chi^{(3)}(-\omega; \omega, -\omega, \omega)$ ) on the THG intensity profile at interfaces. We showed that it clearly affects the THG at entrance and exit interfaces of a single slab, and that the power dependence, of the signal at the exit interface, can be higher than 3 due to the reduction of the beam waist radius occurring as a consequence of the self-focusing effect. In Chapter 4 we investigated the THG at the only two possible interfaces: entrance and exit, and also, as a consequence of only electronic nonlinearities in optical glasses. Now, using a cuvette containing liquid, we extend the study to a more complex configuration with four different interfaces separating different materials and with the presence of both electronic and noninstantaneous nonlinearities in the liquids. In opposition to a single slab sample, where the entrance and exit interfaces are very simple due to the presence of air with negligible nonlinearity, there is now the presence of a medium inside the cuvette with a nonzero nonlinearity. In fact, the linear and nonlinear optical properties of the surrounding medium significantly affect the THG signal depending on the propagation direction. Using silica and Schott B270 Superwhite crown glass cuvettes, filled with three organic solvents (acetone, chloroform, and dimethyl sulfoxide (DMSO)), we have a large variety of interfaces with materials of different linear and nonlinear properties. Kerr nonlinearity of organic solvents can present significant contributions from both pure fast electronic nonlinearities and slow nuclear contributions, such as orientational effects.

The TH peaks for each interface in a particular cuvette-solvent pair have their own magnitude and power dependence. Similar to the single slab interfaces, the cuvette interfaces are also very asymmetric in terms of beam propagation direction. In other words, the THG signal observed when the laser beam propagates from the cuvette to the solvent may be completely different from that generated in the opposite direction. Such dependence was never carefully studied before and it is very relevant for material's characterization and the understanding of fundamental properties. There are several works studying the THG  $z$  response at interfaces between liquid and solid media where the unknown third-order

---

<sup>†</sup> Results already published in Applied Optics.<sup>27</sup>

nonlinear optical susceptibilities of liquids are determined.<sup>3-4,63-65</sup> All these works require the precise value of phase matching integrals ( $J$  integrals) for the case of tightly focused beams. This is not a simple task for interfaces between two media (1 and 2) with unequal dispersion ( $\Delta k_1 \neq \Delta k_2$ ) and nonlinear susceptibilities ( $\chi_1^{(3)} \neq \chi_2^{(3)}$ ).<sup>3</sup> It is possible to do a fast  $\chi^{(3)}$  ratio determination if the  $J$  integrals are previously determined with a numerical calculation.<sup>4,66</sup> In this Chapter we are going to present THG measurements at liquid-glass interfaces and interpret the results. We shall determine the nonlinear optical coefficients of the liquids using a method that makes use of the phase matching integral<sup>4</sup> and, also, show how we can obtain these coefficients using our approach that considers the self-focusing contribution. In our method the nonlinear refractive indices,  $n_2$ , and third-order nonlinear susceptibilities of the solvents,  $\chi^{(3)}$ , are determined simultaneously by the THG signals using the cuvette walls as a reference. The results are compared and discussed.

### 5.1 Theoretical approach

In Chapters 2 and 4 we showed that the THG, in the tightly focused laser beam condition (thick sample), is observed when the interface between two different materials is within the laser confocal parameter region. The THG intensity can be written as

$$I^{(3\omega)} \propto |\Delta\chi^{(3)}|^2 (I^{(\omega)})^3, \quad (5.1)$$

where  $I^{(3\omega)}$  is the irradiance of the TH and  $I^{(\omega)}$  is the irradiance of the fundamental beam.  $\Delta\chi^{(3)}$  is the difference between the third-order nonlinear susceptibility of the two materials, labeled 1 and 2, at the interface. In a more general approach where we consider the  $J$  integrals, we can say that, if medium 2 is air, which has a very weak nonlinearity, we just need the susceptibility of medium 1 (cuvette wall) to obtain<sup>4</sup>

$$I_{cuvette/air}^{(3\omega)} \propto \left| J(b, \Delta k_1) \chi_1^{(3)} \right|^2 (I^{(\omega)})^3. \quad (5.2)$$

On the other hand, for two media with non-negligible nonlinearities:

$$I_{cuvette/solvent}^{(3\omega)} \propto \left| J(b, \Delta k_1) \chi_1^{(3)} - J(b, \Delta k_2) \chi_2^{(3)} \right|^2 (I^{(\omega)})^3, \quad (5.3)$$

where  $J(b, \Delta k)$  is the phase-matching integral defined as

$$J(b, \Delta k) = \int_0^\infty \frac{e^{i\Delta k z}}{(1 + 2iz/b)^2} dz, \quad (5.4)$$

$b$  is the confocal parameter, and  $\Delta k$  is the wave vector mismatch

$$\Delta k = 3k_1 - k_3 = \frac{6\pi}{\lambda} (n_1 - n_3), \quad (5.5)$$

where  $n_1$  and  $n_3$  are the refractive indices at the fundamental and the third harmonic wavelengths, respectively.

It is possible to determine the  $\chi^{(3)}$  ratio between two media (1 = cuvette wall and 2 = solvent) using Eqs. (5.2) and (5.3), according to

$$\frac{\chi_2^{(3)}}{\chi_1^{(3)}} = \frac{J(b, \Delta k_1)}{J(b, \Delta k_2)} \left[ 1 \pm \left( \frac{I_{cuvette/solvent}^{(3\omega)}}{I_{cuvette/air}^{(3\omega)}} \right)^{1/2} \right]. \quad (5.6)$$

In this case, one needs to know the values of  $J$  and use the correct signal, which is usually positive when the nonlinearity of the solvent is higher than that of the cuvette.<sup>66</sup>  $J$  can be numerically calculated with Eq. (5.4). For a fast evaluation of the nonlinear susceptibility ratio, it is possible to graphically obtain an empirical equation that fits  $J$  as a function of  $|b\Delta k|$ .<sup>66</sup> In this case we propose the following dispersion equation:

$$J(x)/b = \left( C_1 + \frac{C_2(x + C_3)^2}{(x + C_3)^2 - C_4} + C_5(x + C_3)^2 \right)^{1/2}, \quad (5.7)$$

where  $x = |b\Delta k|$ , and  $C_1, C_2, C_3, C_4$  and  $C_5$  are the constants to be determined by the fitting procedure. This expression can be justified by its similarity to Sellmeier's equation, in the sense that the dependence of  $J/b$  on  $x$  is analogous to the refractive index dispersion.

It was observed that the THG is strongly affected by the self-focusing that reduces the beam waist at the output of a sample. In this case, the beam waist radius changes at the exit interface as a function of the laser power  $P$  according to

$$w_{output} = w(P) = w_0(1 - BP), \quad (5.8)$$

where  $w_0$  is the radius without self-focusing and  $B$  is an empirical constant proportional to the nonlinear refractive index. The irradiance  $I$  is proportional to  $P/w^2$  and we have

$$I^{(3\omega)} = A' \left( \frac{P}{[w_0(1 - BP)]^2} \right)^3, \quad (5.9)$$

where  $A'$  is the constant related to the term that multiplies  $(I^{(\omega)})^3$  in Eq. (5.3), i.e., the sample nonlinearity. It can be seen in Eq. (5.9) that, due to the self-focusing effect,  $I^{(3\omega)}$  is not proportional to  $P^3$  at the exit interface because the term  $BP$  changes the slope of the  $I^{(3\omega)}$  versus  $P$  curve.  $A'$  is used to adjust the offset. Besides, the self-focusing does not affect the THG  $P^3$  power dependence at the entrance interface because most of the third harmonic is generated before the reduction of the beam waist takes place. Therefore, this model predicts that only the power dependence of the TH generated at the exit interface is affected.

In the previous Chapter, THG at optical glass interfaces, we did not consider the  $A'$  values for any further calculations. Indirectly, the  $A'$  coefficients carry information about  $\chi^{(3)}$  values. To be more complete here, we have used both the  $A'$  and  $B$  coefficients to study the nonlinear refractive indices of the studied organic solvents.

## 5.2 Experiments

The experimental setup is the same one shown in Fig. 4.2. The OPA was set to generate pulses at 1300 nm, leading the TH to be centered at 433 nm. This fundamental wavelength was carefully chosen because it has negligible linear absorption, as does its third harmonic, in all solvents studied. Note that organic solvents usually present several absorptions peaks in the IR range which severely restricts the useful spectral range of THG.

As done in the previous experiment, the sample was scanned through the focus of the laser beam at  $z = 0$ . The negative value of  $z$  means that the sample is placed between the focusing lens and its focal plane. This assumption implies that the exit (entrance) interface appears in the negative (positive)  $z$  position. The laser is focused into the sample with a 50 mm focal length lens ( $b \approx 0.3$  mm,  $w_0 \approx 8$   $\mu$ m) and a 60 mm focal length lens is placed after the sample to collect the TH light into the detector. Since we are using a relatively high laser

irradiance ( $1.4$  to  $2.0 \times 10^{16}$  W/m<sup>2</sup>), the TH generated at the interfaces was strong enough to be detected by a large area silicon PIN detector coupled into a lock-in amplifier. Using the same setup with a germanium PIN detector, we carried out open-aperture Z-scan measurements<sup>15</sup> to verify the presence of any absorptive nonlinearity. With the irradiances used here, no significant two-photon absorption was observed in any of the solvents.

As shown in Fig. 5.1(I), there are four different interfaces for laser focus positioning when a silica cuvette is filled with solvent: (a) air-SiO<sub>2</sub> (entrance interface), (b) SiO<sub>2</sub>-solvent, (c) solvent-SiO<sub>2</sub>, and (d) SiO<sub>2</sub>-air (exit interface). A similar configuration occurs for the B270 cuvette. Owing to these interfaces, there are four positions giving rise to THG, as depicted in Fig. 5.1(II).

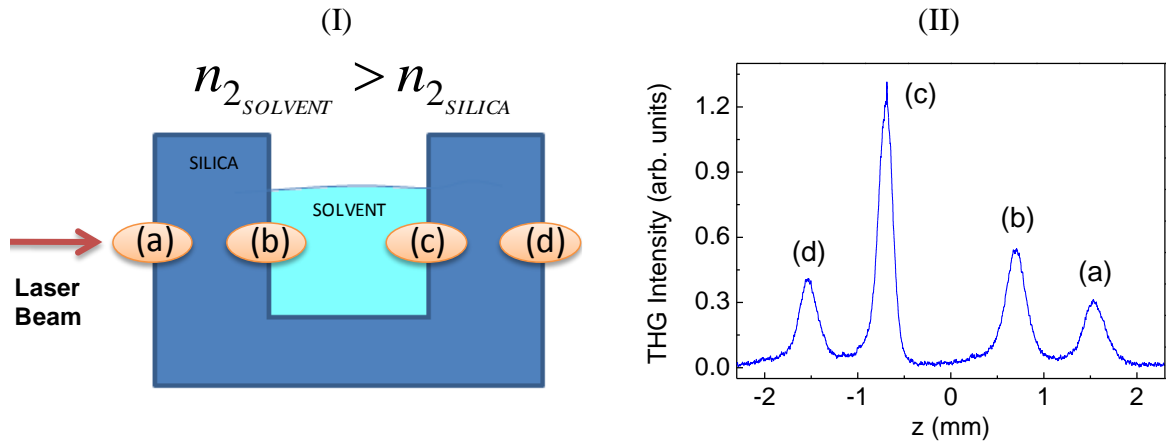


Figure 5.1 – (I) Definition of the cuvette interfaces and, (II) typical TH intensity curve for silica/DMSO system. Source: BARBANO et al.<sup>27</sup>

### 5.3 Results and Discussion

As already mentioned, we used two cuvettes (silica and B270) and three different organic solvents: acetone (CH<sub>3</sub>COCH<sub>3</sub>), chloroform (CHCl<sub>3</sub>), and dimethyl sulfoxide [(CH<sub>3</sub>)<sub>2</sub>SO]. Table 5.1 shows their linear refractive indices,  $n_0$ , for the fundamental and TH wavelengths. These solvents were selected because they have low infrared absorption. Both commercial cuvettes have a 2 mm internal optical path with two windows with 1.2 mm thickness each. The total cuvette thickness is 4.4 mm.

In order to achieve a fast  $\chi^{(3)}$  ( $n_2$ ) ratio calculation, we first found several values of  $J$  by numerically solving Eq. (5.4) (squares in Fig. 5.2), and then we found the best parameters that fit Eq. (5.7) to these points. We obtained the values  $C_1 = -0.2396$ ,  $C_2 = 0.23924$ ,  $C_3 = 4.959$ ,  $C_4 = 19.40569$ , and  $C_5 = 2.93 \times 10^{-8}$ .

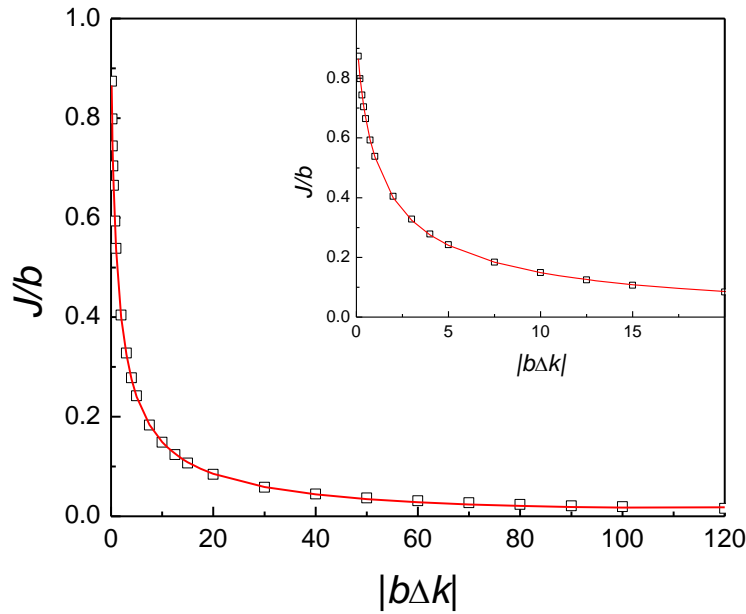


Figure 5.2 – Open squares show values of  $J/b$  as a function of  $|b\Delta k|$  calculated with Eq. (5.4). The solid curve is the best fit obtained by using Eq. (5.7) and the inset is just an expanded view.  
Source: BARBANO et al.<sup>27</sup>

Figure 5.3 shows typical TH profiles for the cuvettes containing the three solvents measured, where four TH peaks with different amplitudes can be seen. By making measurements with different laser powers, each curve presents its own THG peak values at each interface. We first used the procedure described in Barille's paper<sup>4</sup>, based on the ratio between the THG peak values from two distinct interfaces: air/glass and glass/solvent, without considering self-focusing, to find the nonlinear susceptibilities ratios of our solvents with respect to silica and B270. As it can be seen in Fig. 5.3, peaks (b) and (c) [or (a) and (d)] have different magnitudes due to the presence of self-focusing. In this way, there are four possible values for the nonlinear susceptibility ratio for each laser power. These are obtained by using the proper  $I^{(3\omega)}$  ratio in Eq. (5.6), i.e.,  $I^{(3\omega)}$  generated in surface (b) divided by those of (a) and (d), and from surface (c) with (a) and (d). Using these four values we determined an average value and the deviation of each of them from it. Figure 5.4 shows that the nonlinear susceptibilities ratios are nearly constant with the laser power, but the deviations increase as a function of the laser power and nonlinearity strength. These deviations reflect the asymmetry existing in the TH profiles whose origin is the self-focusing effect. DMSO has the highest discrepancy among all solvents because it has the highest nonlinearity. Table 5.2 shows the averaged (AVG) nonlinear susceptibilities ratios obtained with all different laser powers (Fig. 5.4) where the respective uncertainties came from the difference between the maximum (highest laser power) and the minimum values (lowest laser power). From the experimental

data, we can also find that the ratio  $\chi_{B270}^{(3)}/\chi_{silica}^{(3)}$  is about  $1.5 \pm 0.2$ . It is important to observe that in this method, the error rapidly increases with laser power and nonlinearity due to the influence of self-focusing. Note that in the model given by Barille et al.<sup>4</sup>, no self-focusing is taken into account.

Table 5.1 – Dispersion properties of the materials used<sup>a,b</sup>

	$n_0$ (0.43 $\mu\text{m}$ )	$n_0$ (1.3 $\mu\text{m}$ )	$ \Delta k $ ( $\mu\text{m}^{-1}$ )	$ b\Delta k $
Silica	1.467	1.447	0.290	87
B270	1.534	1.510	0.348	104
Acetone	1.368	1.352	0.232	70
Chloroform	1.458	1.434	0.348	104
DMSO	1.492	1.464	0.406	122

Source: BARBANO et al.<sup>27</sup>

<sup>a</sup>The refractive indices were obtained using the Sellmeier coefficients of Silica<sup>67</sup>, B270<sup>68</sup>, acetone<sup>69</sup>, chloroform<sup>70</sup>, and DMSO<sup>71</sup>.

<sup>b</sup>The confocal parameter is  $b = 0.3$  mm.

Next, we determined the nonlinearity ratio using the procedure where self-focusing is considered. The power-dependent TH signals for each interface of the two cuvettes are plotted in Figs. 5.5 and 5.6. As seen, the slopes of the TH peaks can be significantly different from 3, the value expected for a third-order nonlinear process. This can be explained by taking into account the self-focusing effect. We propose a self-consistent procedure to explain the results by using Eq. (5.9) and one parameter, the nonlinear refraction of the cuvette, as a reference. In order to simplify our study, we start by separately analyzing the interfaces that present the same  $\Delta\chi^{(3)}$ , that is, interfaces (a) and (d) and interfaces (b) and (c). According to Eq. (5.1), they should generate the same TH if no self-focusing was present. As seen in Fig. 5.3, the harmonic generated at interface (d) is more intense than one generated at interface (a), and also, it presents a slope higher than 3 (Figs. 5.5 and 5.6) which agrees with previous results obtained with single glass slabs.

In interface (c), the laser beam already propagated from the solvent to silica (or B270) and, as the nonlinearity of all solvents used here are larger than that of the cuvettes walls, the high value of the slope ( $>3$ ) can be explained with the self-focusing effect in the output interface of the solvent. In our model, the self-focusing in the output interfaces, which reduces the beam waist, explains why the slope is larger than 3 which is also responsible for the high magnitude of these peaks in comparison to peaks (b).

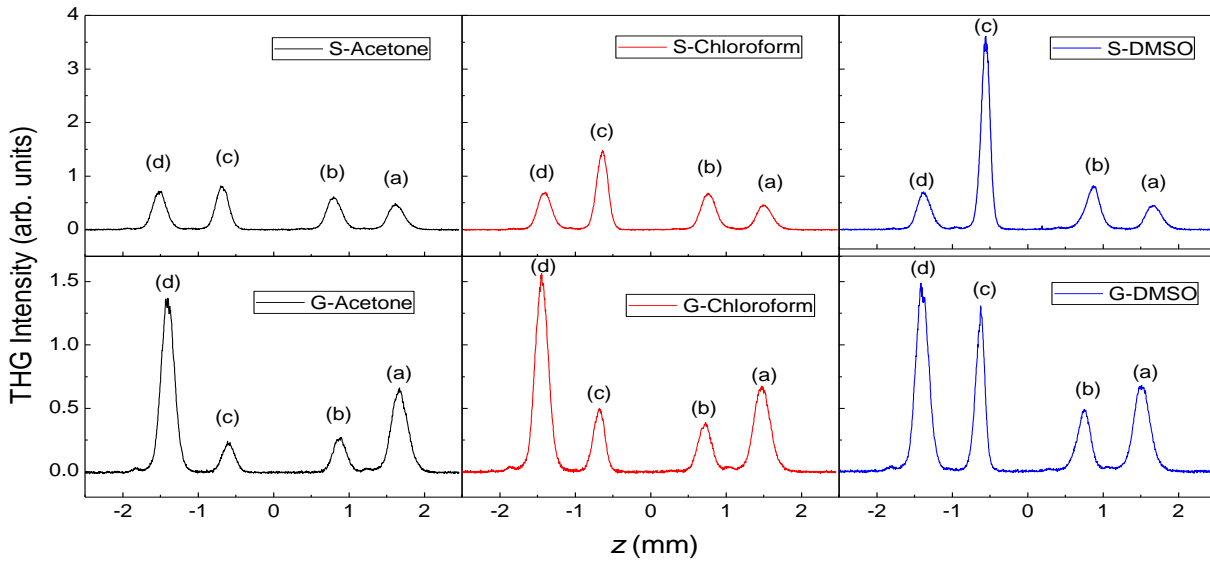


Figure 5.3 – THG signals for three different solvents as a function of the sample position for the four interfaces. We used two different cuvettes: silica (S) and B270 glass (G). The curves were obtained using pump powers of 0.430 mW and 0.415 mW for silica and B270 cuvettes, respectively. Other pump powers present very similar curves.

Source: BARBANO et al.<sup>27</sup>

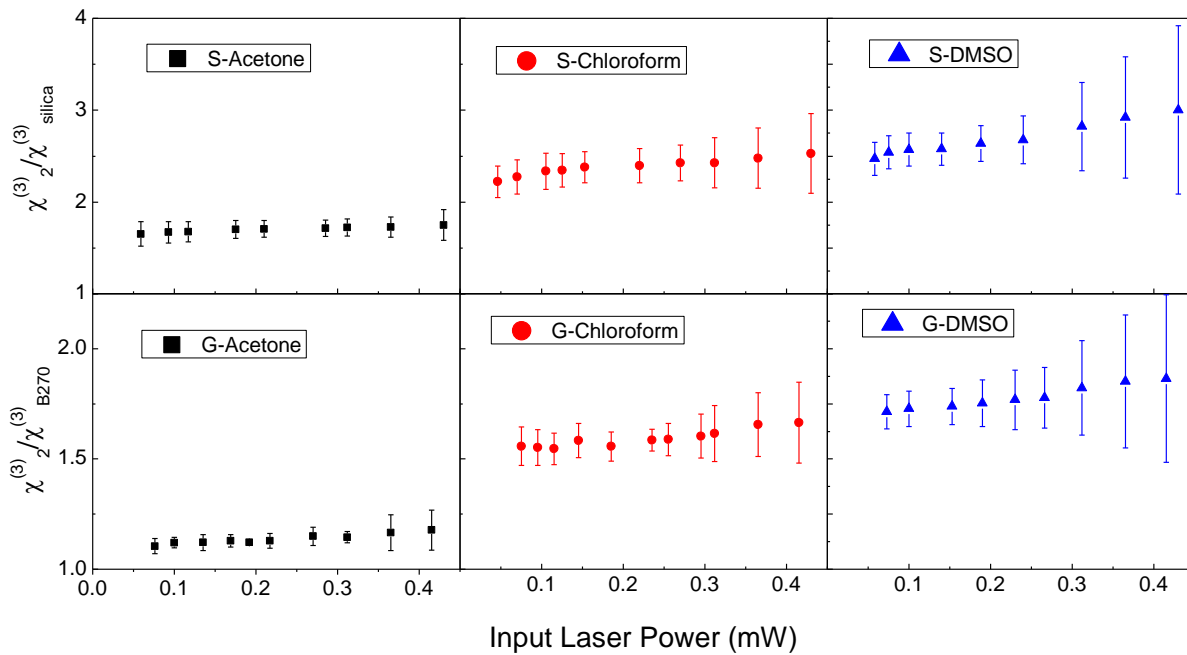


Figure 5.4 – Nonlinear susceptibility ratios for all solvents obtained with TH peak ratios using Eq. (5.6) for different laser powers. We used two different cuvettes: silica (S) and B270 glass (G). The error bar for each laser power comes from dispersion among the four possible ratios.

Source: BARBANO et al.<sup>27</sup>

Table 5.2 – Nonlinear susceptibility ratios of the solvents obtained by averaging the experimental data of Fig. 5.4<sup>a</sup>

Sample	$\chi_2^{(3)}/\chi_{silica}^{(3)}$	$J/b$	$\chi_2^{(3)}/\chi_{silica}^{(3)}$ AVG	$\chi_2^{(3)}/\chi_{B270}^{(3)}$ AVG
Silica	1	0.0209	-	-
B270		0.0195	-	-
Acetone	1.5 <sup>58</sup>	0.0252	$1.7 \pm 0.1$	$1.1 \pm 0.1$
Chloroform	2.3 <sup>58</sup>	0.0195	$2.4 \pm 0.3$	$1.6 \pm 0.1$
DMSO	2.4 <sup>72</sup>	0.0200	$2.7 \pm 0.6$	$1.8 \pm 0.2$

Source: BARBANO et al.<sup>27</sup><sup>a</sup>Here we can consider the silica nonlinearity:  $n_2 = 2.7 \times 10^{-20} \text{ m}^2/\text{W}$ ,  $\chi^{(3)} = 2.0 \times 10^{-22} \text{ m}^2/\text{V}^2$ .<sup>60</sup>

Figure 5.3 shows that the TH generated at the interface (c) is always greater than that generated at (b), except for acetone in the B270 cuvette. In this case, the THG signals are small because their nonlinearities are of the same order of magnitude. This implies that interfaces (b) and (c) experience roughly the same beam waist reduction and, even though the acetone nonlinearity is slightly larger than B270, it is not enough for the peak (c) to overcome the peak (b). Furthermore, acetone presents the largest linear absorption at the pump frequency which reduces the irradiance at the interface (c). This absorption can be noticed in peak (d), which is the output of the B270 cuvette, where the THG signal is somewhat smaller with acetone in comparison with other solvents.

It is evident from Fig. 5.3 that Fresnel reflection is not the main factor responsible for the TH intensity profile change, as could be expected.<sup>12</sup> When the laser beam passes through an interface from an isotropic material to another, at near-normal incidence, there is interference between the incident and reflected light within a distance of  $\lambda/4$  of the entrance interface.<sup>49,73</sup> If the beam propagates from one material with higher refractive index to another with lower refractive index, constructive interference happens and increases the laser intensity, and destructive interference occurs for the opposite propagation case. In fact, this effect is used to explain why the exit interfaces, not the entrance interfaces, are first damaged. But here, for the silica cuvette filled with acetone or chloroform, we have constructive interference at the interface (b) and destructive interference at the interface (c). For DMSO, we have the opposite case, destructive interference at (b) and constructive at (c). However, in all cases the TH generated at the interface (c) is more intense than that generated at the interface (b), independent of the Fresnel reflection. Even for the B270 cuvette, the self-focusing effect is more appropriate to explain the THG behavior. Nonlinear susceptibilities and refractions can be found by fitting the slope of the power dependence of each peak, as shown in Figs. 5.5 and 5.6. In order to do it, we fit the experimental data by means of Eq.

(5.9) and obtain the coefficients  $A$  ( $A = A'/w_0^6$ ) and  $B$  for each solvent. The constant  $A$  is related to the symmetry breaking of the nonlinear susceptibility at the interface,  $\Delta\chi^{(3)}$ ,  $B$  is proportional to the nonlinear refraction,  $n_2$ , responsible for changing the beam waist radius owing to the self-focusing action. We assume that  $B$  must be the same at the interfaces (b) and (d),  $B_b = B_d$ , since the self-focusing occurs in the same material of the cuvette (silica or B270), and must be zero at the interface (a),  $B_a = 0$ , since the THG slope is unaffected by self-focusing, i.e., the slope is constant and equal to 3. Also, we use the condition that the two internal interfaces must present the same value of  $A$ ,  $A_b = A_c$ , as well as the two external interfaces,  $A_a = A_d$ . Using these considerations it is possible to carry out the adjustment at each interface by placing only one parameter as a variable, which provides more reliable values for each coefficient. We start with the interface (a) where we already know the coefficient  $B$ , ( $B_a = 0$ ), and then we obtain the parameter  $A_a = A_d$  by the fitting.

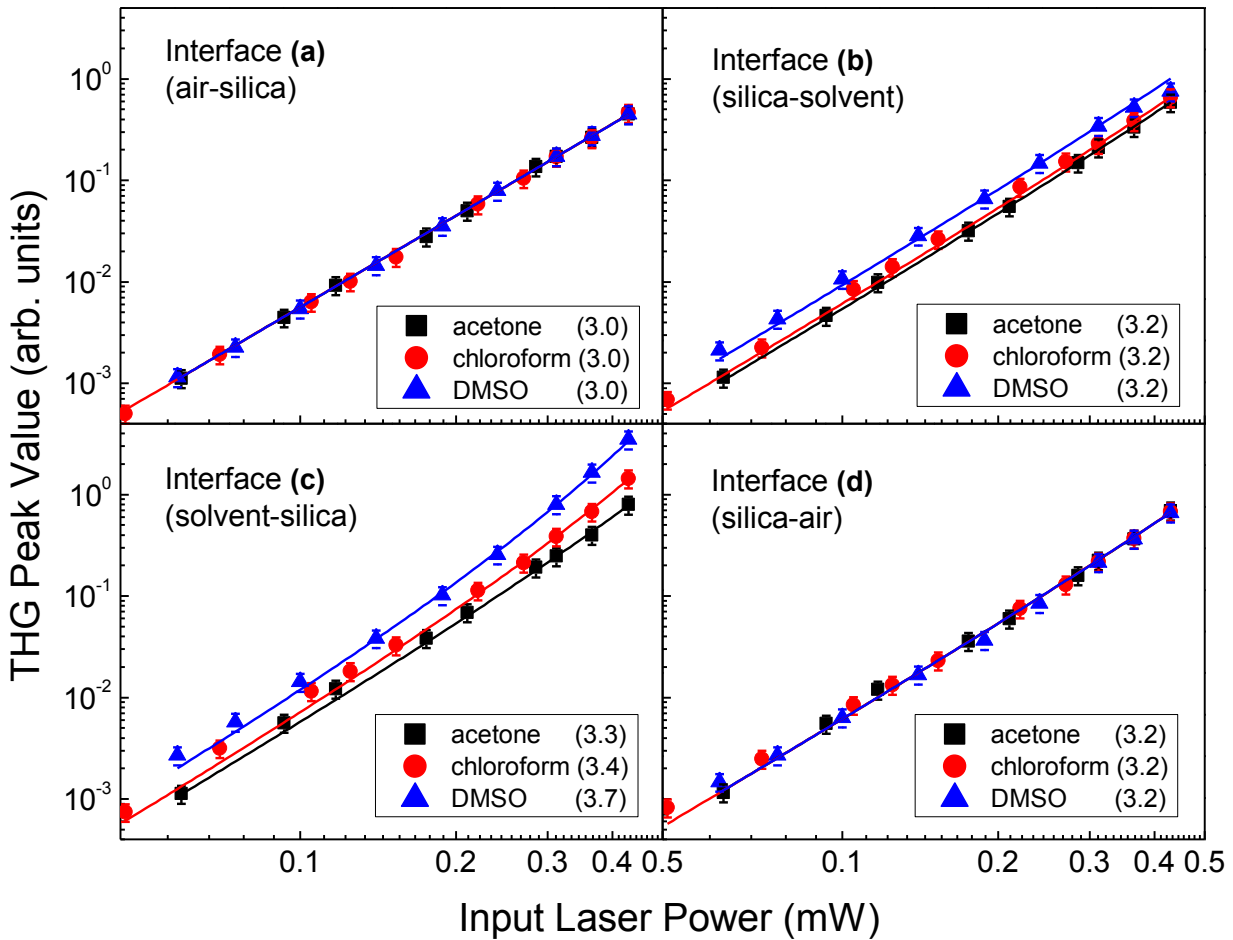


Figure 5.5 – Peak values of THG curves at the silica cuvette interfaces as a function of input laser power for all solvents and all interfaces. The symbols are the experimental data and the solid lines are the fits using the empirical model. The numbers in parentheses are the approximate slopes.

Source: BARBANO et al.<sup>27</sup>

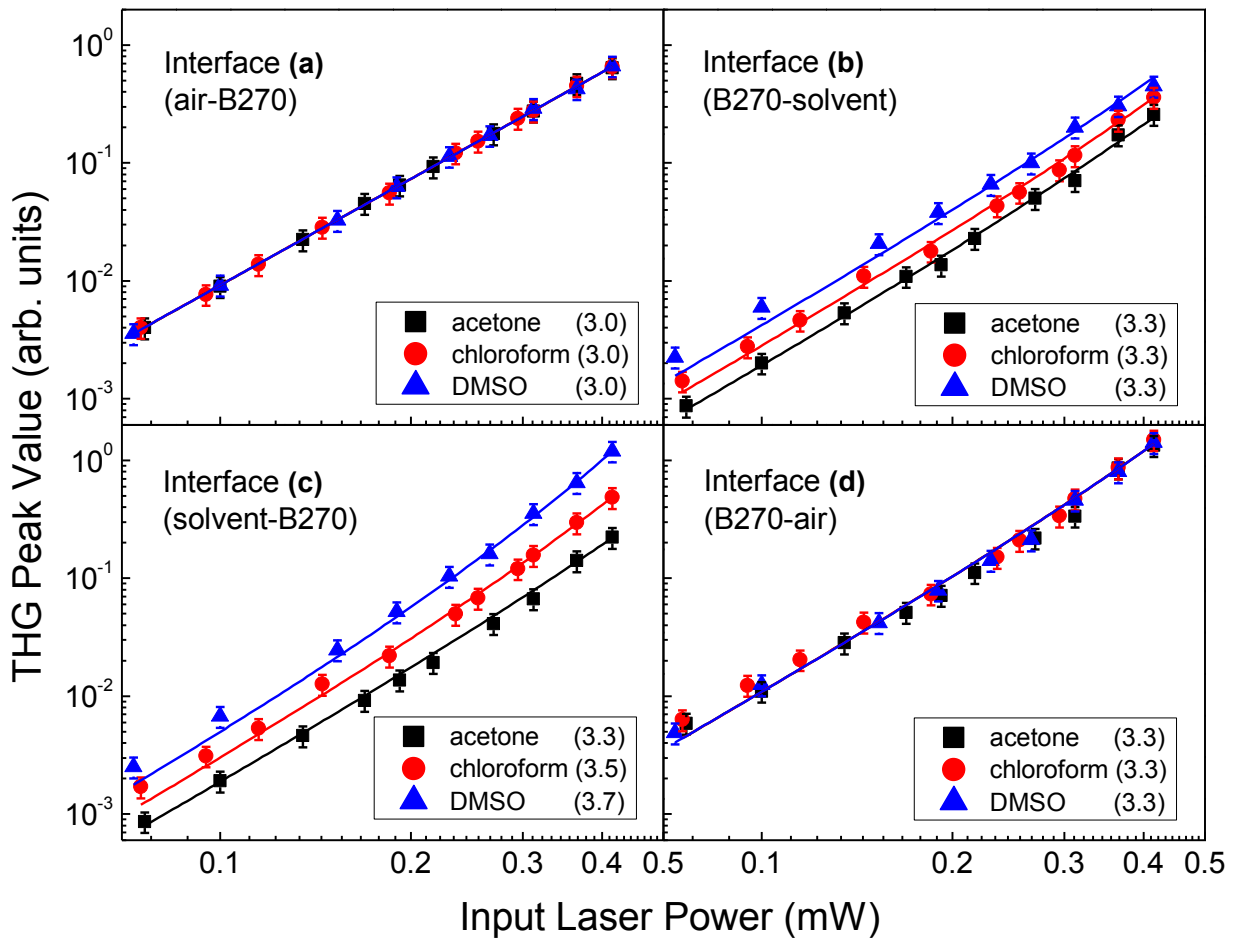


Figure 5.6 – Peak values of THG curves at the B270 cuvette interfaces as a function of input laser power for all solvents and all interfaces. The symbols are the experimental data and the solid lines are the fits using the empirical model. The numbers in parentheses are the approximate slopes.

Source: BARBANO et al.<sup>27</sup>

Table 5.3 – Coefficients  $A$  and  $B$  obtained for the silica cuvette for interfaces (b) and (c)<sup>a</sup>

Sample	(b)	(c)
Acetone	$A = 4.95 \pm 0.06$	$A = 4.95 \pm 0.06$
	$B = 0.15 \pm 0.01$	$B = 0.25 \pm 0.01$
Chloroform	$A = 5.6 \pm 0.1$	$A = 5.6 \pm 0.1$
	$B = 0.15 \pm 0.01$	$B = 0.41 \pm 0.02$
DMSO	$A = 8.5 \pm 0.1$	$A = 8.5 \pm 0.1$
	$B = 0.15 \pm 0.01$	$B = 0.55 \pm 0.02$

Source: BARBANO et al.<sup>27</sup>

<sup>a</sup>For interfaces (a) and (d) for all solvents,  $A = 5.6 \pm 0.1$ ,  $B = 0$  and  $A = 5.6 \pm 0.1$ ,  $B = 0.15 \pm 0.01$ , respectively.

$A_d$  must be used at the interface (d) to obtain  $B_d = B_b$ . The procedure follows by using  $B_b$  to find  $A_b = A_c$  at the interface (b). Finally, knowing  $A_c$  we obtain  $B_c$  at interface (c). Tables 5.3 and 5.4 summarize all values found for silica and B270 cuvettes. Both  $A$  and  $B$  are related to  $n_2$  (or  $\chi^{(3)}$ ) and it is possible to estimate the nonlinearity of each solvent by using directly the ratio  $B_c/B_b = n_2(\text{solvent})/n_2(\text{silica or B270})$ , or by using Eq.(5.6) just

replacing  $I$ 's by respective  $A$ 's, since  $A$  carries information about the TH intensity. As can be seen, it is not possible to get the values of nonlinearity ratios by simply using the  $A$ 's ratios. It is necessary to use an indirect method based on Eq. (5.6). In this case, it is also necessary to use the  $J$  values for each solvent and cuvette material. Using a linear fit in a log-log scale we can note the slope is equal to 3 only at the first interface, where there is no self-focusing contribution in the TH peak value. For the other interfaces, the power law dependence of the THG is higher than 3 due to the influence of the Kerr lens effect.

Table 5.4 – Coefficients  $A$  and  $B$  obtained for the B270 cuvette for interfaces (b) and (c)<sup>a</sup>

Sample	(b)	(c)
Acetone	$A = 1.62 \pm 0.02$	$A = 1.62 \pm 0.02$
	$B = 0.28 \pm 0.02$	$B = 0.24 \pm 0.01$
Chloroform	$A = 2.38 \pm 0.04$	$A = 2.38 \pm 0.04$
	$B = 0.28 \pm 0.02$	$B = 0.39 \pm 0.02$
DMSO	$A = 3.55 \pm 0.05$	$A = 3.55 \pm 0.05$
	$B = 0.28 \pm 0.02$	$B = 0.55 \pm 0.02$

Source: BARBANO et al.<sup>27</sup>

<sup>a</sup>For interfaces (a) and (d) for all solvents,  $A = 9.2 \pm 0.1$ ,  $B = 0$  and  $A = 9.2 \pm 0.1$ ,  $B = 0.28 \pm 0.02$ , respectively.

Table 5.5 – Ratios  $n_{2\text{solvent}}/n_{2\text{cuvette}}$  obtained with the coefficients  $B$  and  $A$ <sup>a</sup>

Sample	Literature (silica)	$B$ (silica)	$A$ (silica)	AVG (silica)	$B$ (B270)	$A$ (B270)	AVG (B270)
Acetone	1.7 <sup>58</sup>	$1.7 \pm 0.1$	$1.6 \pm 0.1$	$1.7 \pm 0.1$	$0.9 \pm 0.1$	$1.1 \pm 0.1$	$1.0 \pm 0.1$
Chloroform	2.3 <sup>58</sup>	$2.7 \pm 0.2$	$2.1 \pm 0.2$	$2.4 \pm 0.3$	$1.4 \pm 0.1$	$1.5 \pm 0.1$	$1.5 \pm 0.1$
DMSO	2.4 <sup>72</sup>	$3.7 \pm 0.3$	$2.3 \pm 0.2$	$3.0 \pm 0.7$	$2.0 \pm 0.2$	$1.6 \pm 0.1$	$1.8 \pm 0.8$

Source: BARBANO et al.<sup>27</sup>

<sup>a</sup>AVG corresponds to averaged values obtained with the  $A$  and  $B$  coefficients.

As expected, interfaces (a) and (d) for both silica and B270 cuvette have about the same results independent of the solvent. Fortunately, for this pulse width and wavelength, dispersion is not expected to significantly broaden the pulse or cause chromatic aberration. In this way, we have not considered any change caused by dispersion.

Table 5.5 summarizes the results obtained for nonlinear refractive index ratios using coefficients  $B$  and  $A$ , in silica and B270 cuvettes. Here, we observe that the coefficients  $A$  and  $B$  lead to roughly similar  $n_2$  ratios. The discrepancies between the two values increase systematically with the sample's nonlinearity as in the Barille's method.<sup>4</sup> However, in our model, Eq. (5.9), the coefficients  $A$  and  $B$  have reverse contribution to the THG intensity. An overestimation of  $A$ 's corresponds to underestimation of  $B$ 's and, in this way, the most correct values can be obtained by averaging the two values. In fact, if we take the average ratio values

of the  $n_2$ 's in Table 5.5, for each solvent, we can get about the same values shown in Table 5.2. Since all measurements were carried out using the same laser configuration, we can also find the ratio of the  $n_2(\text{B270}) / n_2(\text{silica})$  using the respective coefficients  $A$  and  $B$ . Using  $A$ 's (using Eq. 5.2) and  $B$ 's we got about 1.37 and 1.87, respectively. The average value is about  $1.6 \pm 0.2$  which is very similar to one obtained from intensity ratio measurements,  $1.5 \pm 0.2$ , and they are in the range of that expected for such borosilicate type of glass.<sup>74</sup> We believe that the main reason for the difference between the ratio's values obtained by these two coefficients is the simplicity of our model. Despite this drawback, our model explains very well the contribution of the self-focusing on the change of the slope for the THG versus  $P$  curves in organic solvents.

It is also possible to notice the contribution of the self-focusing in narrowing the peaks (c)'s width. In each measurement, the peak (c) is the narrowest peak in the curve. Although this effect is expected at the exit interface in the presence of the self-focusing, here, it is not clear about entrance or exit interfaces since both media no longer have negligible nonlinearities. In fact, according to our model, there is competition between narrowing (exit interface of the solvent) and broadening (entrance interface of the cuvette wall) in these interfaces (c), for instance. In this way, we have not considered this study here because no clear behavior was observed in terms of narrowing or broadening of the two, (b) and (c), internal interfaces. Such competition is not easy to model and there is no simple confocal length equation as a function of the laser power that can be evaluated as in the previous work with optical glasses. In general, we notice that both peaks, (b) and (c), were narrowed (beam waist reductions) and, consequently, an increase in the peaks' slopes were observed.



## 6 THG AT ORGANIC SOLVENTS INTERFACES AS A FUNCTION OF PULSE DURATION

Although the TH is a pure electronic process, the self-focusing can have electronic and other nonlinear mechanism (such as orientational, for instance) contribution. Several organic solvents have both electronic and orientational nonlinearities.<sup>58</sup> Here, working in the tightly focused laser beam condition and with a silica cuvette filled with solvent, we can obtain conditions where the self-focusing occurs inside the silica, where only the electronic nonlinearity is present, and a situation where self-focusing occurs inside the solvent, where both contributions, electronic and orientational, may be present. In addition, the instantaneous electronic nonlinearity is a constant as a function of the pulse width, which is not the case for the orientational one. Orientational  $n_2$  is only constant for pulses much longer than the orientation response time.<sup>75</sup> Hence, it is possible to change the effective nonlinearity of a solvent controlling the pulse duration (chirp) if the orientational response time is in the order of the pulse duration. Here, we propose a study of the self-focusing effect on the THG just changing the pulse duration of the excitation beam.

In this experiment we have used the same laser system Ti:sapphire (CPA 2001 – Clark MXR) which delivers pulses with 150 fs duration at 1 kHz repetition rate. This time, we did not use the OPA since we wanted to control the pulse duration. The laser emission is centered at  $\lambda = 775$  nm with THG at the ultraviolet, 258 nm. The laser beam is focused into the sample using a 50 mm focal length lens ( $z_R \approx 0.17$  mm,  $w_0 \approx 7$   $\mu\text{m}$ ,  $I_0 \approx 1 \times 10^{16}$  W/m<sup>2</sup>). After the sample we use a 60 mm focal length lens to collect the TH light into the detector (UV-VIS USB 2000+, Ocean Optics). This collection lens must be transparent to 258 nm and, in this way, we have used a silica lens, instead of the BK7 lens typically used. The temporal pulse duration ( $\sim 150$  fs to  $\sim 2$  ps) can be controlled directly by the laser compressor already inside the laser system. The pulse duration was measured by Z-scan technique, in the thin sample condition, using silica as a reference. The Z-scan  $\Delta T_{pv}$  for a refractive signature is proportional to the nonlinearity of the sample, the sample's thickness and the laser irradiance. Using a well-known sample, silica, with known thickness and  $n_2$ , it is possible to calibrate the irradiance necessary to obtain the  $\Delta T_{pv}$  measured. Finally, with the laser power and beam waist radius,  $w_0$ , one can find the pulse duration. As sample we have used a silica cuvette filled with the same organic solvents: acetone, chloroform and DMSO.

## 6.1 Results

In the cuvette we have four interfaces: air-silica (entrance interface), silica-solvent, solvent-silica and silica-air (exit interface), that were labeled as (a), (b), (c) and (d), respectively, see Fig. 5.1. The cuvette was scanned along the  $z$  axis, as done in the two previous experiments, and the TH signal was collected into the spectrometer. Due to the shorter TH wavelength, peaks (a) and (b) are strongly attenuated by the solvent absorbance and, in this way, we can only use the peaks (c) and (d) for analysis.

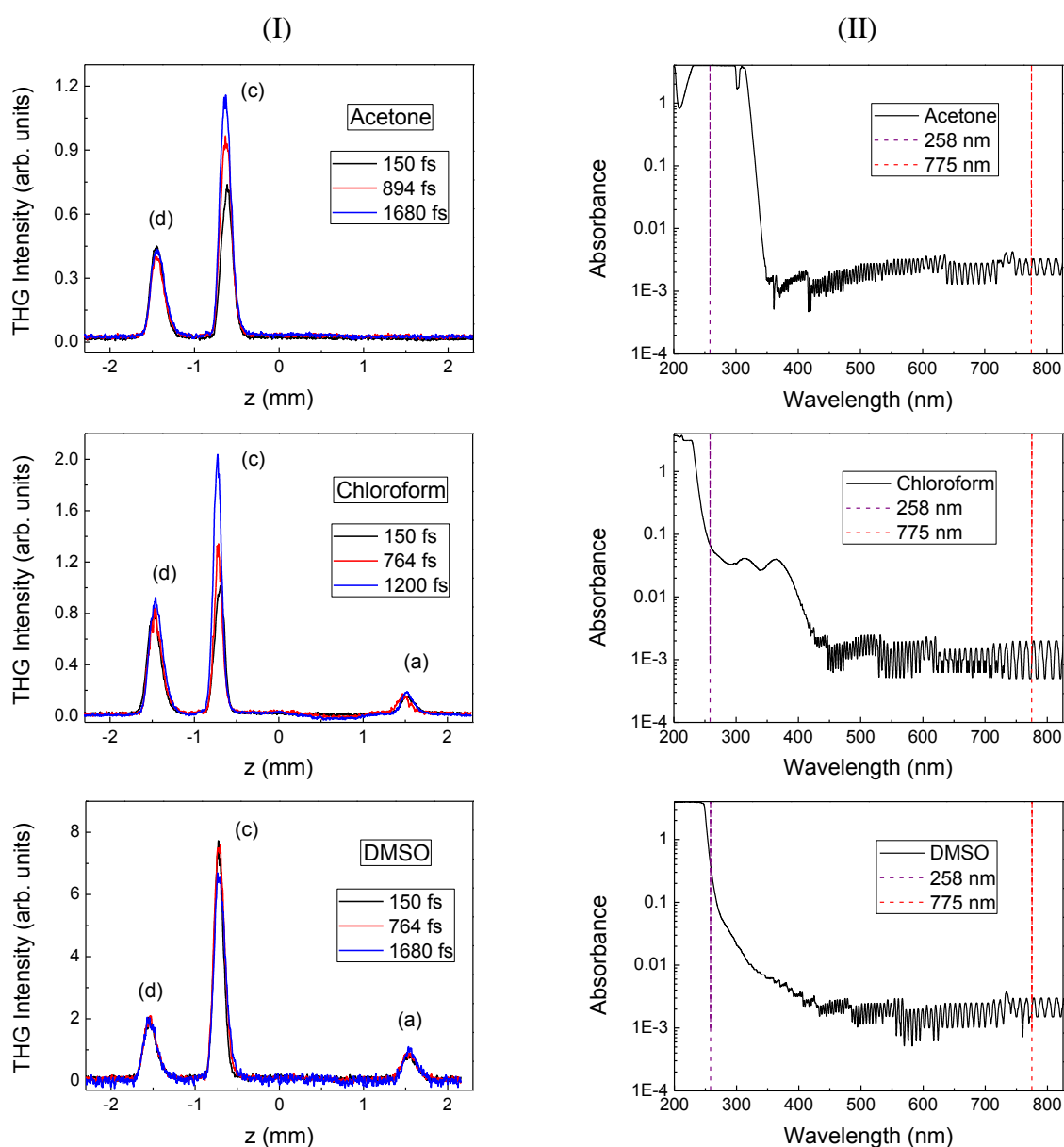


Figure 6.1 – (I) Integrated THG signal. The interfaces were labeled as (a) air-silica (entrance interface), (b) silica-solvent (there is no signal at this interface), (c) solvent-silica and (d) silica-air (exit interface). The TH profiles are presented for acetone, chloroform and DMSO for different pulse durations. (II) Absorbance spectrum for each solvent.

Source: By the author.

Figure 6.1 (I) shows THG measurements for different pulse durations. In order to preserve the same TH signal at the interface (d), that we can use as a reference due to the electronic origin of its nonlinear response, the irradiance was set to be approximately constant, for each solvent, for the different pulse durations.

As it can be seen in Fig. 6.1 (I), the TH signal for acetone and chloroform at the interface (c) is enhanced for longer pulses and there is no significant variation for DMSO. These results indicate that, for long pulses, the orientational nonlinear refractive index increases its contribution on the self-focusing effect in acetone and chloroform. By our results, chloroform has somewhat stronger orientational nonlinearity in comparison with acetone, which is in agreement with Rau et al.<sup>58</sup> In the case of DMSO, it seems that this solvent has no significant orientational nonlinearity for the pulse widths we have used here. That means the DMSO may have a low orientational contribution and most of its nonlinearity has electronic origin (the pure electronic nonlinearity of the solvent should have the same pulse width dependence of the silica and, consequently, no enhancement should be observed). More measurements and references to check the DMSO behavior are needed. Also, the TH generated at the entrance interface, peak (a), disappears for acetone due to the strong linear absorption at 258 nm. For chloroform and DMSO, it is possible to see the peak (a) because they have lower linear absorption at the TH wavelength, Fig. 6.1 (II). Peaks (b)s are not seen in the Fig. 6.1 (I), for none of the solvents, probably due to the presence of both linear and nonlinear absorption. Our results, although preliminary, are in accordance with the expected by the self-focusing model. In the future, we intend to extend this study to other solvents in order to discriminate the contribution of the electronic and orientational processes on THG at interfaces.



## 7 SPIFI IMAGING WITH A PROGRAMMABLE 2D SPATIAL LIGHT MODULATOR

### 7.1 Abstract

This chapter presents the activities developed in the Squier's group at Colorado School of Mines (CSM), Golden, CO, USA. The activities involved the construction of a new SPIFI (SPatIal Frequency-modulated Imaging) microscope's design using a 2D SLM (Spatial Light Modulator) and the record and analyses of images obtained by different nonlinear optical processes, such as, TPEF (Two-Photon Excitation Fluorescence), SHG (Second-Harmonic Generation) and THG (Third-Harmonic Generation). Especially, we recorded THG SPIFI images for the first time. Also, the THG images were obtained by different configurations of the SLM, amplitude modulation and phase modulation. This new design gives more flexibility and can open new possibilities for SPIFI as well as permits to explore superresolution images (sub-diffraction-limit).

### 7.2 Introduction

Third-harmonic generation (THG) is a nonlinear optical process which has been used for material's characterization and in applications such as in optical microscopy. In this last case, THG microscopy is a background-free imaging technique that does not require additional staining and occurs in all media regardless of symmetry.<sup>76</sup> It was first proposed in 1997 by Barad et al.<sup>7</sup> and was extended to the realization of three-dimensional volume imaging in 1998.<sup>77</sup> In the pioneer work, Barad et al.<sup>7</sup> demonstrated that the THG of a tightly focused ultrashort pulse can be used to form a nonlinear laser scanning microscope. Generally, tight focusing conditions prevent the production of the third harmonic (TH). This can be understood in terms of the Gouy phase shift the beam experiences when going through the focus position as discussed in Chapter 2. However, at the interface between two different materials the TH is nonvanishing. It occurs because at the interface the symmetry is broken within the confocal parameter by either a change in the refractive index or third-order nonlinear susceptibility.<sup>78</sup> Thus, despite the TH be radiated from the bulk of the media, on the tightly focused condition, it is observed only at the interface. Therefore, the idea of THG microscopy is that TH will be produced at existing interfaces and inhomogeneities in the specimen. The long excitation wavelength generally used in this technique and the

nonresonant nature of the third-order process make the method potentially nonbleaching and, also, reduce the possibility of biological damage.<sup>77</sup> Since it is a nonlinear optical effect, basically only at the focal plane the light efficiently drives the nonlinearity. This condition eliminates out-of-focus contributions and results in the optical sectioning inherent to nonlinear imaging techniques. Because we study the THG process and know it is an important contrast mechanism in nonlinear optical microscopy, we are interested in learning more about this applied research strand.

Most nonlinear imaging methods rely on point-by-point scanning of an image, but with this approach extended time may be required to form a full image. A line cursor geometry can be used allowing high-speed image acquisition.<sup>77</sup> In such a system the line sweeps out a two-dimensional field in the focal plane with a single axis scan, and the multiphoton signal can be recorded at the same time by a two-dimensional detector, such as a charge-coupled-device (CCD) camera.<sup>79</sup> However, non-ballistic photons may scatter at the sample and be registered at an incorrect position on the 2D detector, decreasing the image quality.<sup>80</sup> An advancement in imaging technology for eliminating the scattering ambiguity is the line cursor excitation system that only requires single element detection.<sup>16</sup> In this case, the excitation beam is spatially modulated with frequencies that linearly increase across its spatial extent. This provides a unique modulation frequency to each spatial point of the beam mitigating the scattering ambiguity problem. This spatially-chirped intensity modulation on the excitation beam is performed using an amplitude mask pattern printed onto a spinning disc which is placed at the focal plane of the cylindrical lens. This approach of a SPAtial Frequency modulation for Imaging is abbreviated as SPIFI. The SPIFI technique has been used to obtain two-dimensional images of absorptive and fluorescent objects<sup>16</sup> and also two-photon excitation fluorescence (TPEF) imaging.<sup>79</sup> SPIFI has been extended to two-dimensional imaging through parallel acquisition of line images<sup>17</sup> and to the combination of features of spatially chirped modulation with spectral encoding.<sup>81</sup> Recently, SPIFI has been shown to have the added benefit of superresolved multimodal imaging.<sup>18</sup> Multiphoton SPIFI provides spatial resolution up to  $2\beta$  below the diffraction limit, where  $\beta$  is the highest power of the nonlinear irradiance response, for instance,  $\beta = 4$  for SHG and  $\beta = 6$  for THG. Michael D. Young developed in his PhD<sup>82</sup> a SPIFI system replacing the printed mask by a programmable 2D spatial light modulator (SLM). This has the advantage that we can do adaptive aberration correction by using different masks and opens the possibility of taking images with amplitude modulation as well as phase modulation. Working directly with Michael in the Squier's group, we developed a new version of the Young's microscope where

we improved the microscope's design and took third-harmonic images for the first time using a SPIFI setup. Due to patent's issue we won't describe the microscope design in detail in this dissertation but we are going to show the basic setup and the first images. In order to illustrate the versatility of this new configuration we shall show TPEF, SHG and finally THG images. It is worth mentioning that the THG images by either amplitude or phase modulation are unprecedented.

### 7.3 SPAtIal Frequency-modulated Imaging - SPIFI

In optical microscopy, a strategy for improving imaging speeds is to use an extended geometry such as a line cursor instead of a point focus. The first demonstration of a real-time multiphoton microscope was performed by Brakenhoff et al.<sup>83</sup> where the multiphoton signal was mapped using a two-dimensional detector, such as a CCD camera. Later, it was demonstrated that it is possible, through spatial modulation of the beam, that is, SPIFI approach, to use the line cursor excitation combined with single element detection.<sup>16,79</sup> In SPIFI, the output of the laser is usually expanded in a telescope, and then focused with a cylindrical lens that creates the line cursor at an intermediate plane. A modulator placed at the focal plane of the cylindrical lens produces an intensity modulation with a frequency that linearly increases along the extent of the line focus, Fig. 7.1.

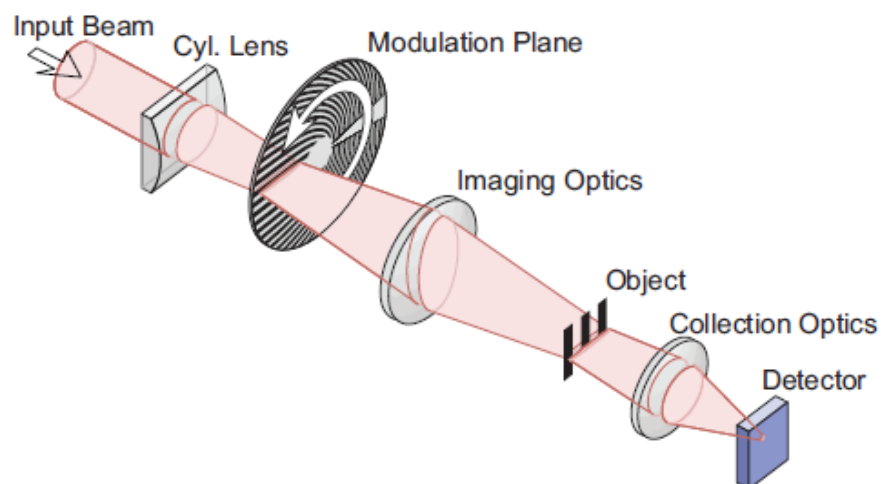


Figure 7.1 – Schematic of first SPIFI setup.  
Source: FUTIA et al.<sup>16</sup>

In SPIFI, the sequential points in the line focus are modulated at slightly higher frequencies as a function of spatial position. In this way, the spatial location is encoded by the

modulation frequency. This modulated line is then imaged onto an object and the transmitted light collected with a single-element detector, such as a photodiode or photomultiplier tube (PMT). The spatial information of the image is encoded in the temporal modulation frequencies, which are present in the signal recorded by the detector. For nonlinear microscopy, as presented here, the spatially-chirped intensity modulation of the excitation beam might be transferred to the photons emitted by either fluorescence or harmonic generation and the Fourier transform of the signal should retrieve the line image of the object.

Recently, it was demonstrated that using the SPIFI microscope it is possible to obtain images in superresolution (sub-diffraction-limit).<sup>18</sup> When the laser beam passes through the time-dependent spatial modulation pattern, produced by the spinning disk rotation (or, as in our case, by the SLM modulation), the line focus is diffracted into several beams with varying propagation angles,  $\theta_j$ , where  $j$  corresponds to the diffracted order, Fig. 7.2. The microscope is configured such that the diffracted orders are collected in the pupil of the objective lens and, in the object plane, they interfere and form a spatial intensity pattern that vary with scan time. Considering  $j \in \{-1,0,1\}$  where  $j = 0$  corresponds to the undiffracted beam and  $j = \pm 1$  corresponds to the first-order diffracted beams, we can say that, at the focus, the interference of these three beams results in an irradiance of the form  $I(x,t) = H_0(t) + H_1(t)\cos[2\pi k_x(t)x] + H_2(t)\cos[2\pi(2k_x(t))x]$ , where the time-varying amplitudes are from vignetting caused by the circular pupil.  $k_x(t)$  is the spatial frequency of the interference fringes and  $H_q(t)$  is determined by the amplitude of the diffracted beams in the object plane as a function of scan time and the image order  $q$ . Here we are assuming the light is focused in the  $y$  dimension and we have the line focus in the  $x$  dimension. The first term  $H_0(t)$  consists of a background irradiance which presents no interference fringes. The first spatially modulated component,  $I_1(x,t) = H_1(t)\cos[2\pi k_x(t)x]$ , is generated from the interference of the undiffracted beam with each diffracted beam and the second one,  $I_2(x,t) = H_2(t)\cos[2\pi(2k_x(t))x]$ , from the interference of the two diffracted beams with one another. The spatial frequency of  $I_2(x,t)$  is twice that of  $I_1(x,t)$ . But, by means of multiphoton nonlinear optical processes, it is possible to reach spatial frequencies greater than  $2k_x$  since the irradiance dependence is of the form  $I^\beta$  where  $\beta$  is the power of the nonlinear irradiance response, for instance, for TPEF and SHG  $\beta = 2$  and for THG  $\beta = 3$ . In this way, multiphoton SPIFI microscopy can provide spatial resolution up to  $2\beta$  below the diffraction limit.<sup>18</sup>

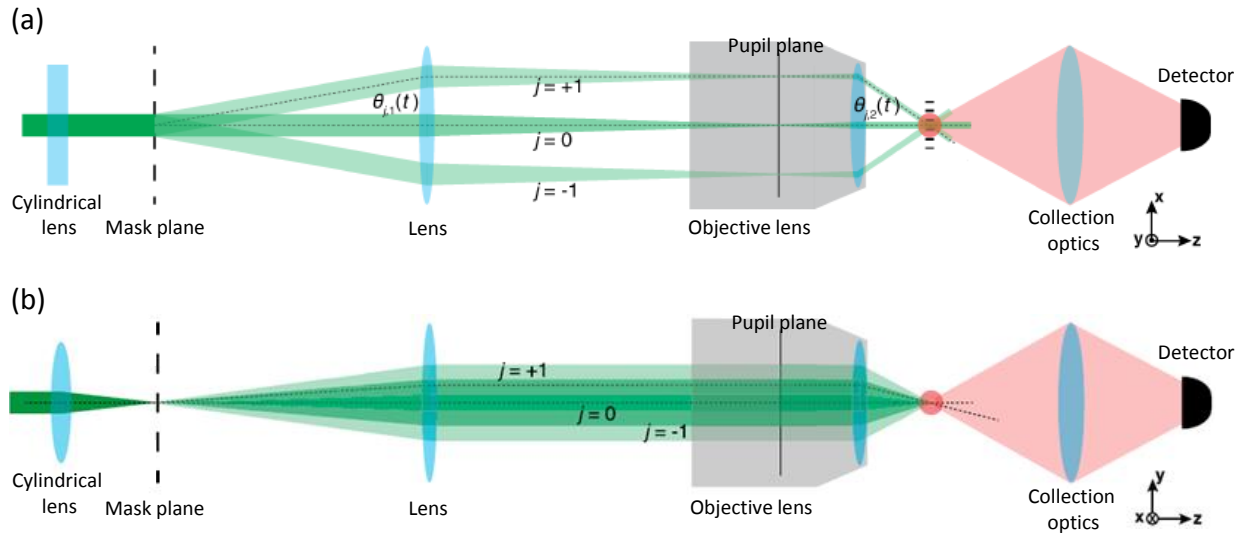


Figure 7.2 – SPIFI system configuration with circular reticle (mask) for superresolved multiphoton microscopy. Schematic representations in the  $(x,z)$  (a) and  $(y,z)$  (b) planes.

Source: Adapted from FIELD et al.<sup>18</sup>

The modulation disk used by Futia et al.<sup>16</sup> is the Lovell reticle<sup>84</sup> which is a series of spatial frequencies plotted in  $\theta$  and are all in phase at  $\theta_0$ . The equation for the modulation pattern is given by

$$m(R, \theta) = \frac{1}{2} + \frac{1}{2} \cos(\Delta k R \theta) \quad (7.1)$$

where  $R$  and  $\theta$  are, respectively, the radial and angular coordinates relative to the center of the disk and  $\Delta k$  is the modulation frequency range over the radius of 0 to  $R_{max}$ . Spinning the mask at a constant angular velocity  $d\theta/dt = \omega$  we can make the substitution  $\theta = \omega t$ , where we are taking  $\theta_0 = 0$ . In this case, the modulation equation in terms of  $R$  and  $t$  is given by

$$m(r, t) = \frac{1}{2} + \frac{1}{2} \cos(\Delta k R \omega t) \quad (7.2)$$

Since the spinning reticle is in circular form and the SLMs are constructed in rectangular form, the mask should be transformed and plotted in Cartesian coordinates.<sup>85</sup> In this way, the modulation equation in Cartesian coordinates is:<sup>82</sup>

$$m(x, y) = \frac{1}{2} + \frac{1}{2} \cos(2\pi \kappa x y) \quad (7.3)$$

The spatial frequency in  $x$  and  $y$  is given by

$$k_x(y) = 2\pi\kappa y \quad (7.4)$$

$$k_y(x) = 2\pi\kappa x \quad (7.5)$$

With the spinning disk the spatial frequencies come into phase at  $\theta_0$  and constructively interfere over a certain coherence time, Fig. 7.3. With the SLM the equivalent is in the middle of the  $x$  dimension, Fig. 7.4.

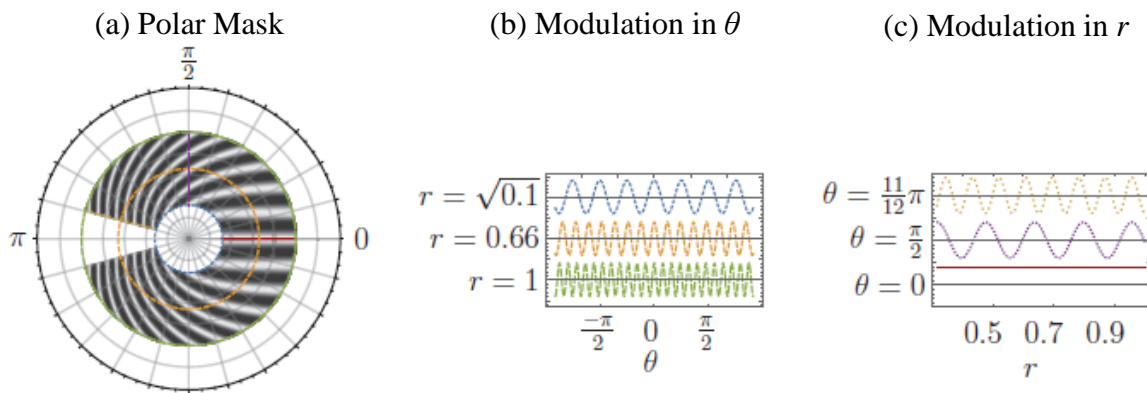


Figure 7.3 – (a) circular reticle. (b) modulation in  $\theta$  at different values of  $r$ . (c) modulation in  $r$  at different values of  $\theta$ .

Source: Adapted from YOUNG.<sup>82</sup>

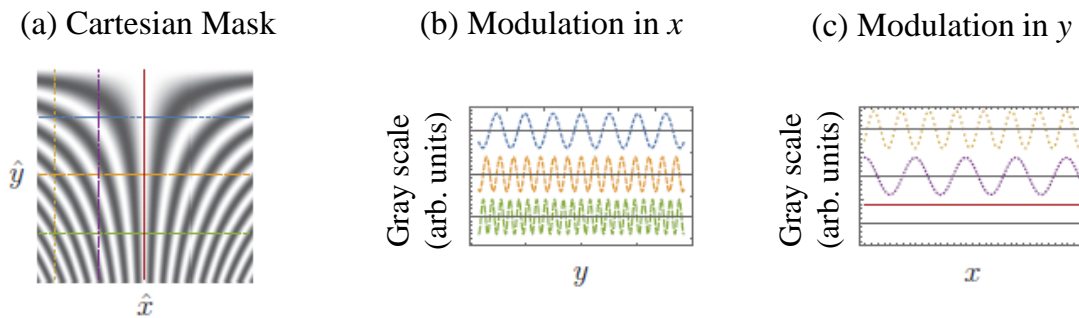


Figure 7.4 – (a) equivalent Cartesian mask to be used with the 2D SLM. (b) modulation in the  $x$  dimension at different values of  $y$ . (c) modulation in the  $y$  dimension at different values of  $x$ .

Source: Adapted from YOUNG.<sup>82</sup>

It is important to point out that in this SPIFI method each frequency carries information about one position of the sample corresponding to one particular position of the line focus. To recover the image from the single detector it is necessary to make a Fourier Transform operation, where we may have access to the different orders (harmonics) of the fundamental frequency. The strongest image (or fundamental image) is recovered from the first-order, but we may have other orders (second, third, fourth...) that appear as weaker

images (the higher the order, the weaker the image) that promote improvement on image resolution.

#### 7.4 Experimental setup

As light source we have used a solid state KGW laser pumped by a 25 W fiber coupled diode module with a 200  $\mu\text{m}$  core diameter emitting at 980 nm (F25-980-2, Apollo Instruments, Inc). The KGW laser generates a 56 MHz pulse train with a maximum average power of 2.5 W, thus yielding energies as high as 45 nJ/pulse. The pulses are centered at 1039 nm and have a duration of 247 fs (bandwidth of about 4.9 nm).<sup>21</sup>

The laser beam was focused by a cylindrical lens and the line cursor produced was projected onto the face of the SLM, which was, in turn, image relayed to the focal plane of the excitation objective. In order to produce the SPIFI signal the line cursor was scanned on the SLM from left to right and back continually by means of a galvanometric mirror controlled by software made in LabVIEW platform.

We have used a 512x512-pixel nematic liquid-crystal spatial light modulator (LC-SLM; Meadowlark Optics). The SLM may be thought as an array of tiny programmable waveplates. Like all waveplates, there is a fast axis and a slow axis. However, with the SLM we can control the refractive index along the slow axis electronically allowing accurate control of the polarization state. For amplitude modulation of the excitation beam the laser should pass through a Polarizing Beamsplitter (PBS), this will select a polarization state of the light. Next, the beam passes through a half waveplate at  $22.5^\circ$ , which rotates the polarization by  $45^\circ$ . This means the light illuminates the SLM polarized in  $45^\circ$  and is reflected off of the reflective pixels, passing again through the PBS which rejects one polarization state producing the amplitude modulation. A scan lens between the galvanometric mirror (scan mirror) and the SLM is used as described in Fig. 7.5. Choosing the correct focal length of the scan lens it is possible to adjust the system magnification. As mentioned earlier, due to patent's issue we don't describe the microscope design in detail in this report but Fig. 7.5 shows the basic microscope's schematic diagram for amplitude modulation configuration. But from this design one can easily change to the phase modulation configuration. In this case the cylindrical lens should be slightly tilted in order to change the height of the beam that, in its turn, passes over the PBS after the reflection on the SLM, that is, the beam does not pass through the PBS twice. In both cases, amplitude and phase modulation, the modulated light reaches the back aperture of the objective lens and is focused on the sample. A translation

stage is used to scan the sample and the signal is collected by a PMT. Depending on the nonlinear process we are measuring, TPEF, SHG or THG, different filters in the PMT must be used according to the wavelength of the produced light.

It is important to say that the nematic SLM, as used here, works by applying an electric field that changes the index of refraction of the pixel. This results in a change in the optical path length and, consequently, a phase delay for the photons incident on that pixel. Since a linear response for phase delay vs voltage applied is interesting because a better approximation of sinusoidal modulation (from minimum to maximum intensity) can be produced, and the standard SLM's LUT (Look-up-table) does not provide this linear response, an SLM calibration is necessary. For this, the SLM's response over its voltage range was recorded and calibrated.

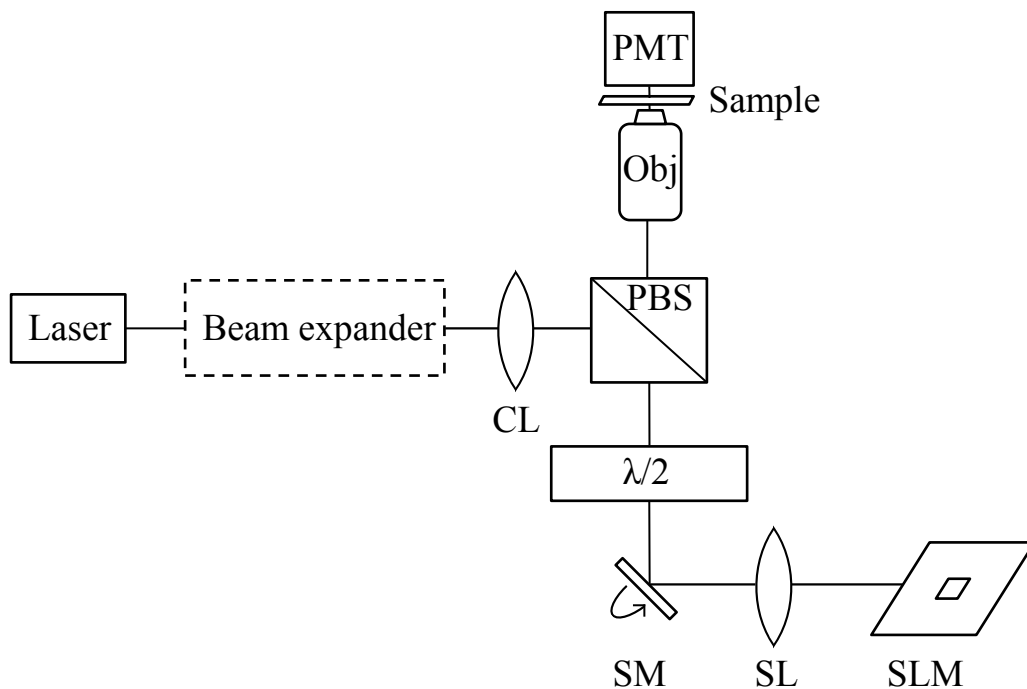


Figure 7.5 – Schematic diagram for amplitude modulation using cylindrical lens and galvanometric mirror, CL = cylindrical lens, PBS = polarizing beamsplitter,  $\lambda/2$  = half waveplate, SM = scan mirror (galvanometric mirror), SL = scan lens, Obj = objective lens. The half waveplate should rotate the input polarization by  $45^\circ$ .

Source: By the author.

## 7.5 Results

By matching the beam size to the back aperture of the objective lens, the resolution should be the diffraction limit of the objective. By using the Rayleigh criterion the diffraction limit is given by

$$d = \frac{0.61\lambda}{NA} \quad (7.6)$$

where  $\lambda$  is the wavelength of the pump beam and  $NA$  is the numerical aperture of the objective lens. In our system, all images were collected using  $\lambda = 1039$  nm and a 0.65  $NA$  objective lens. The lateral resolution is 975 nm for first order images.

In the first test we collected the beam signal without sample and observed the SPIFI trace, that is a pulse created when the frequencies come into phase. The Fourier transform converts the signal to its power spectrum where we can see the beam profile, Fig. 7.6.

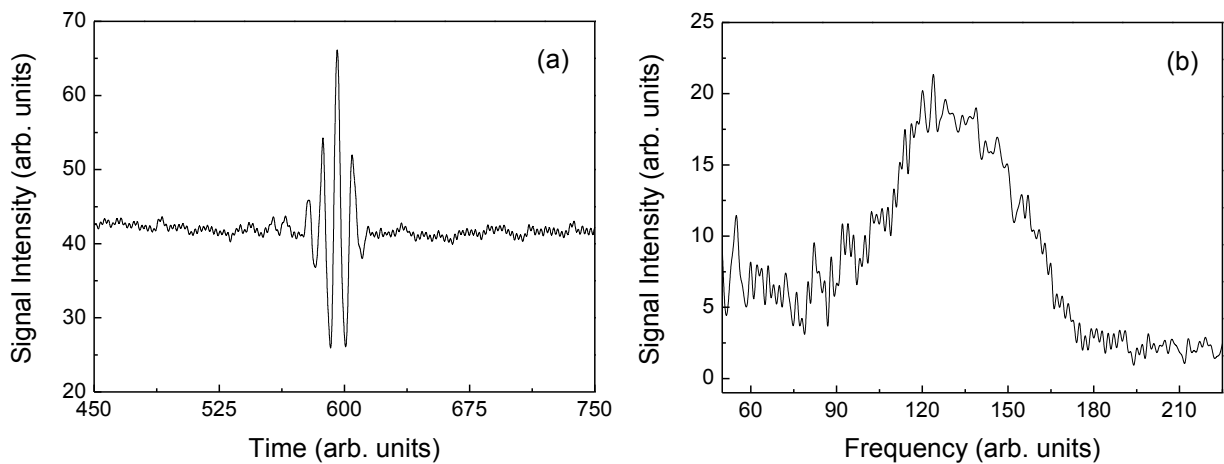


Figure 7.6 – (a) SPIFI trace of the laser beam. (b) beam profile retrieved.

Source: By the author.

In the second test we have blocked part of the line cursor using a stick, as shown in Fig. 7.7. By doing so, we removed the central part of the line cursor and, consequently, the central frequencies of modulation. This could be checked by analyzing the Fourier transform of the SPIFI signal, Fig. 7.8, confirming that our system is imaging correctly.

For the signals shown in Figs. 7.6 and 7.8 we have not observed the second harmonic of the fundamental signal in the Fourier transform (although it is a linear process it is possible to obtain, theoretically, up to the second-order signal). In another measurement, this time using a sample placed at the focal plane of the objective lens, we collected the TH of polystyrene beads, Fig. 7.9. Now we can see the second-order signal which is twice broader than the fundamental one, Fig. 7.10. The third-order is difficult to be observed due to the signal-to-noise ratio. There is an overlap between the range covered by the second- and the third-order signals. In Fig. 7.9 we just collected one SPIFI trace, but to form an image the sample should be translated and sequential SPIFI traces collected.

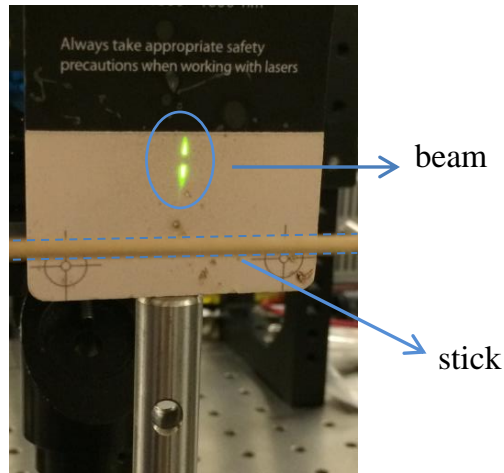


Figure 7.7 – Central part of the line cursor blocked with a stick.  
Source: By the author.

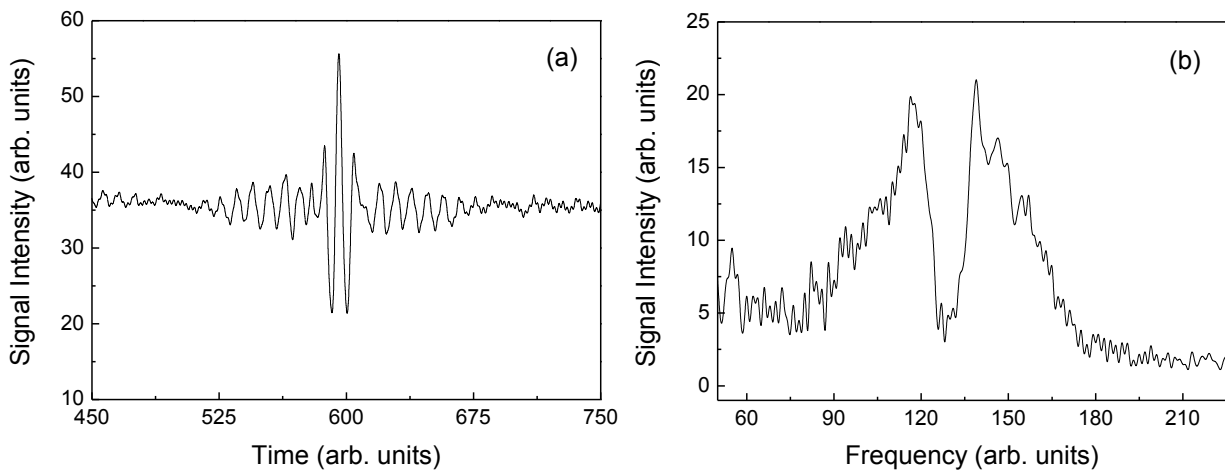


Figure 7.8 – Measurement with a stick blocking the central part of the beam as shown in Fig. 7.7. (a) SPIFI trace of the laser beam. (b) beam profile retrieved.  
Source: By the author.

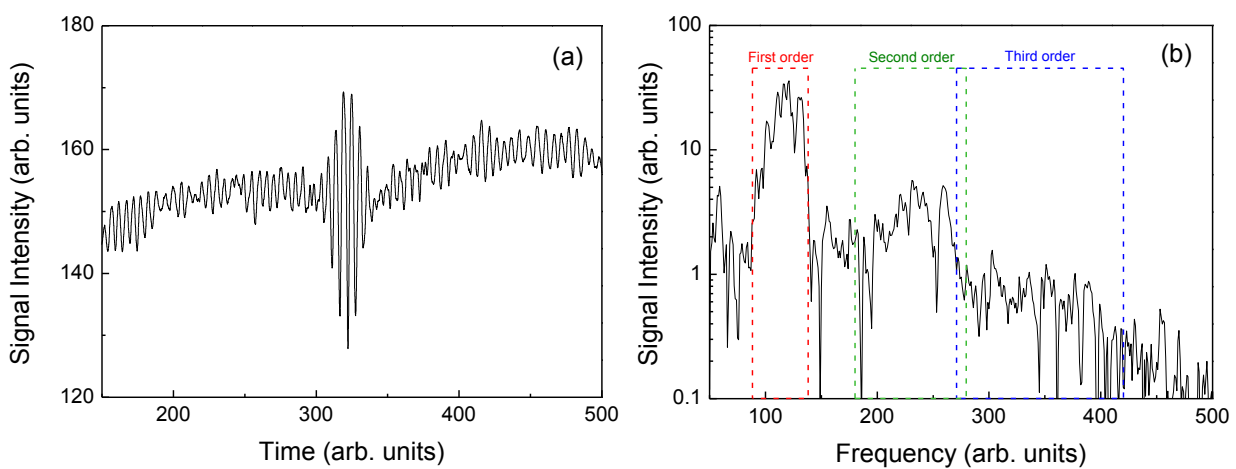


Figure 7.9 – THG SPIFI signal of polystyrene beads (a). Fourier transform of the signal with respect to the scan time where it is possible to observe the higher-order signals (b).  
Source: By the author.

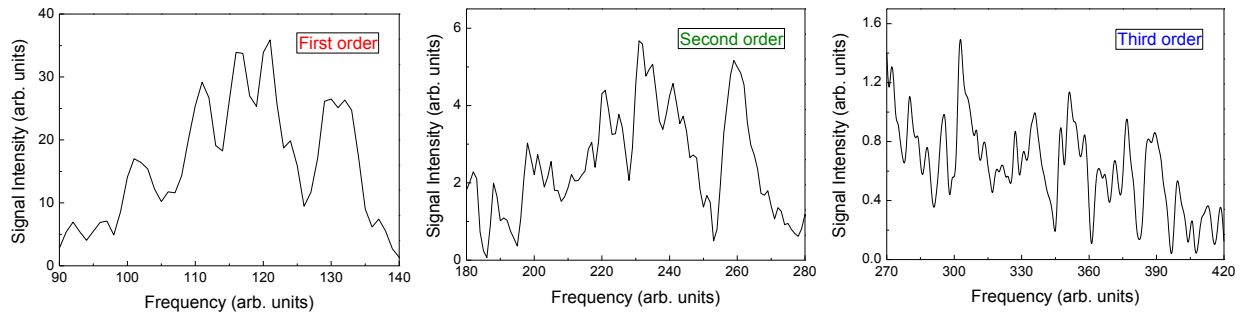


Figure 7.10 – First-, second- and third-order signals obtained in the Fourier transform. The higher orders make possible superresolution images.

Source: By the author.

In order to illustrate the versatility of the microscopy we show images recorded by different nonlinear optical process as TPEF, SHG and THG. Data were processed using *Mathematica* (Wolfram, Champaign, IL, USA). We colored the images differently depending on the process, TPEF = “*SunsetColors*”, SHG = “*BlueGreenYellow*” and THG = “*AvocadoColors*”. The samples were held between the cover slip and a cover slide which rests on the microscope’s stage.

### *TPEF SPIFI Imaging*

The first images were taken by TPEF using onion skin cells and lens tissue as samples. The samples were stained with a pink fluorescent highlighter which is an easy and inexpensive way to create test samples. The highlighter dye creates TPEF at focus that can be measured by the PMT. Figure 7.11 is an image of an onion cell skin. For this first measurement we do not have white light or real scale image but it is an interesting image which illustrates the procedure we used and shows how the second-order signal improves the resolution. In order to visualize and compare the first- and second-order images we normalized both to the same intensity (the higher is the order, the smaller is the signal). In this image we can see what looks like an improvement in resolution of the second order comparing it to the first one (it would be necessary a white-light image to ensure this). Also, as expected, the second-order image is twice the size in the horizontal dimension of the image which means an improvement of two in resolution.

Figure 7.12 shows how they look like when we rescale them to the same dimension. Due to the broader frequency range of the higher orders of diffraction, it is common that the higher order overlaps with the lower one and, as the lower order is more intense, the higher one is obfuscated. It is not the case of the Fig. 7.12 (b), but since it happens for the next

images, from now on, for all images which present higher orders we are going to use a black screen placed on the left side of the image where the lower order saturates the brightness, as shown in Fig. 7.12 (c). This helps us to visualize better the images related to the harmonics of the fundamental signal at the power spectrum.

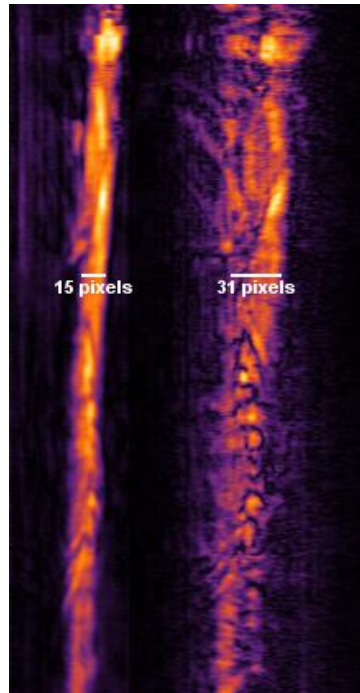


Figure 7.11 – Portion of an onion skin sample. On the left we see the first order and on the right the second order of diffraction, both correspond to the same portion of the sample. The bars were used to verify the second order is twice the thickness of the first, 31 and 15 pixels respectively.

Source: By the author.

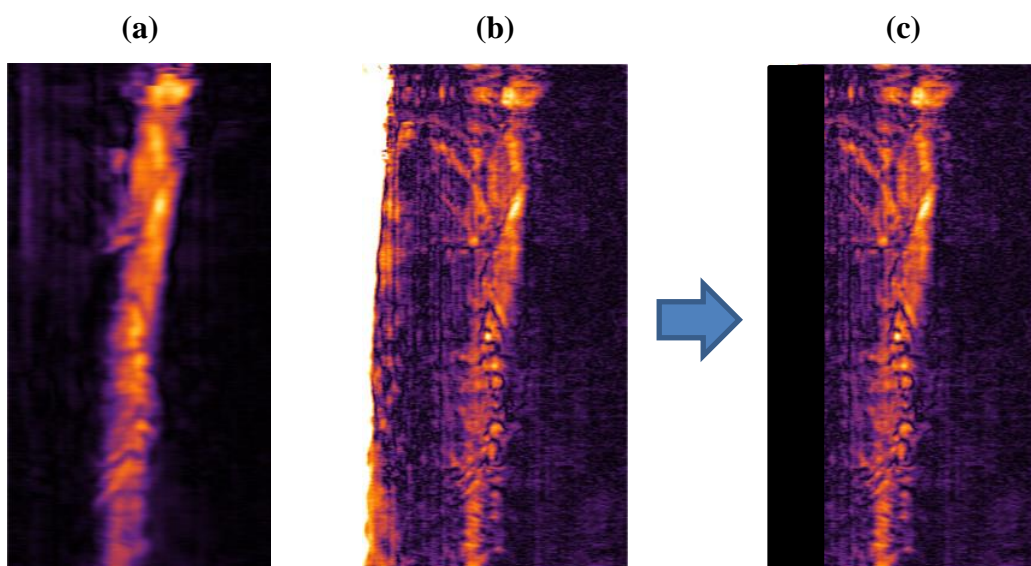


Figure 7.12 – TPEF images collected from a portion of onion skin sample with SPIFI. (a) first- and (b) second-order SPIFI images. (c) A black screen is placed on the left side of the image to avoid the saturation caused by the lower order.

Source: By the author.

Figure 7.13 shows the images obtained for the lens tissue sample. This time, due to the higher sample brightness we could reach the third-order signal (Fig. 7.13 (c)). Fig. 7.13 (d) shows the same portion of the sample under white light illumination. The vertical lines in the Fig. 7.13 (d) indicate approximately the portion of the sample (region between the lines) scanned by the line cursor.

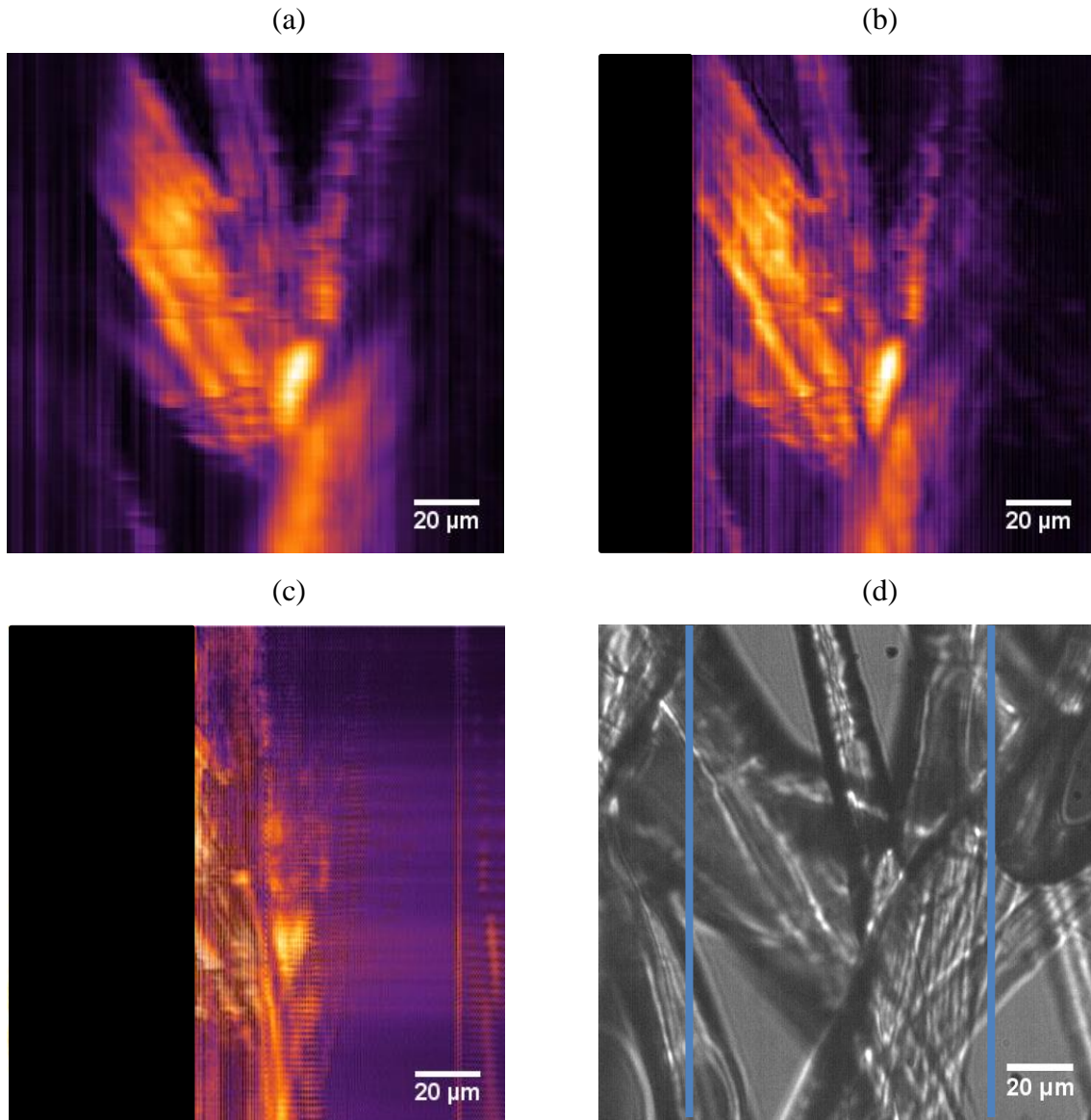


Figure 7.13 – TPEF images collected from lens tissue sample. (a) – (c) first through third order images. Scale bar: 20μm. (d) sample under white light illumination, the vertical lines indicate approximately the portion of the sample scanned by the line cursor.

Source: By the author.

*SHG SPIFI Imaging*

SHG image of cornstarch in water was taken, Fig. 7.14, the same configuration was used. For this sample any higher order was observed.

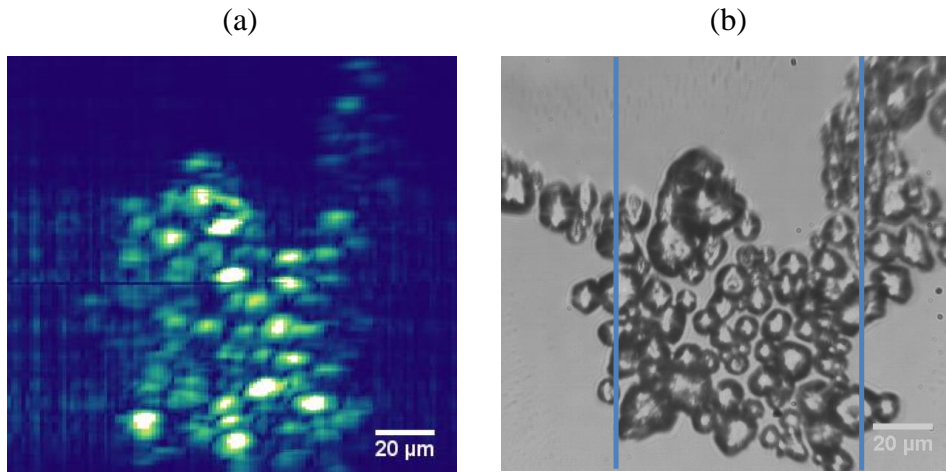


Figure 7.14 – SHG images collected from cornstarch in water. (a) SPIFI image, (b) sample under white light illumination, the vertical lines indicate approximately the portion of the sample scanned by the line cursor.

Source: By the author.

*THG SPIFI Imaging*

Finally, THG SPIFI images of polystyrene beads were taken. Figure 7.15 shows the first THG SPIFI image. The beads have a diameter of  $6 \mu m$  and their TH images do not require staining.

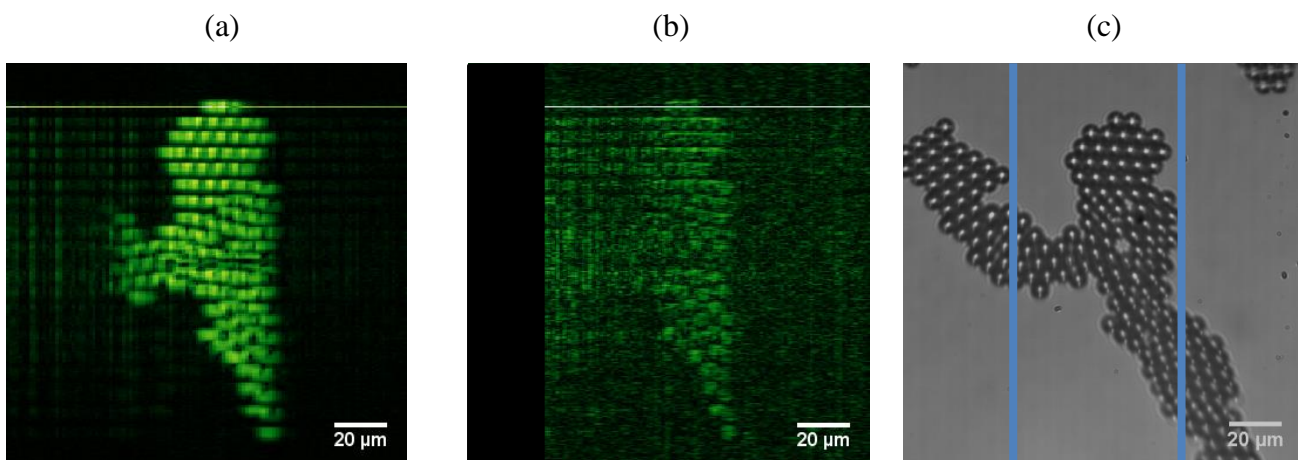


Figure 7.15 – First THG SPIFI image. (a) and (b) are the first and second order images of polystyrene beads (diameter =  $6 \mu m$ ). (c) sample under white light image. Scale bar:  $20 \mu m$ .

Source: By the author.

By repeating the measurement for the same sample we were able to get the third-order image as shown in Fig. 7.16.

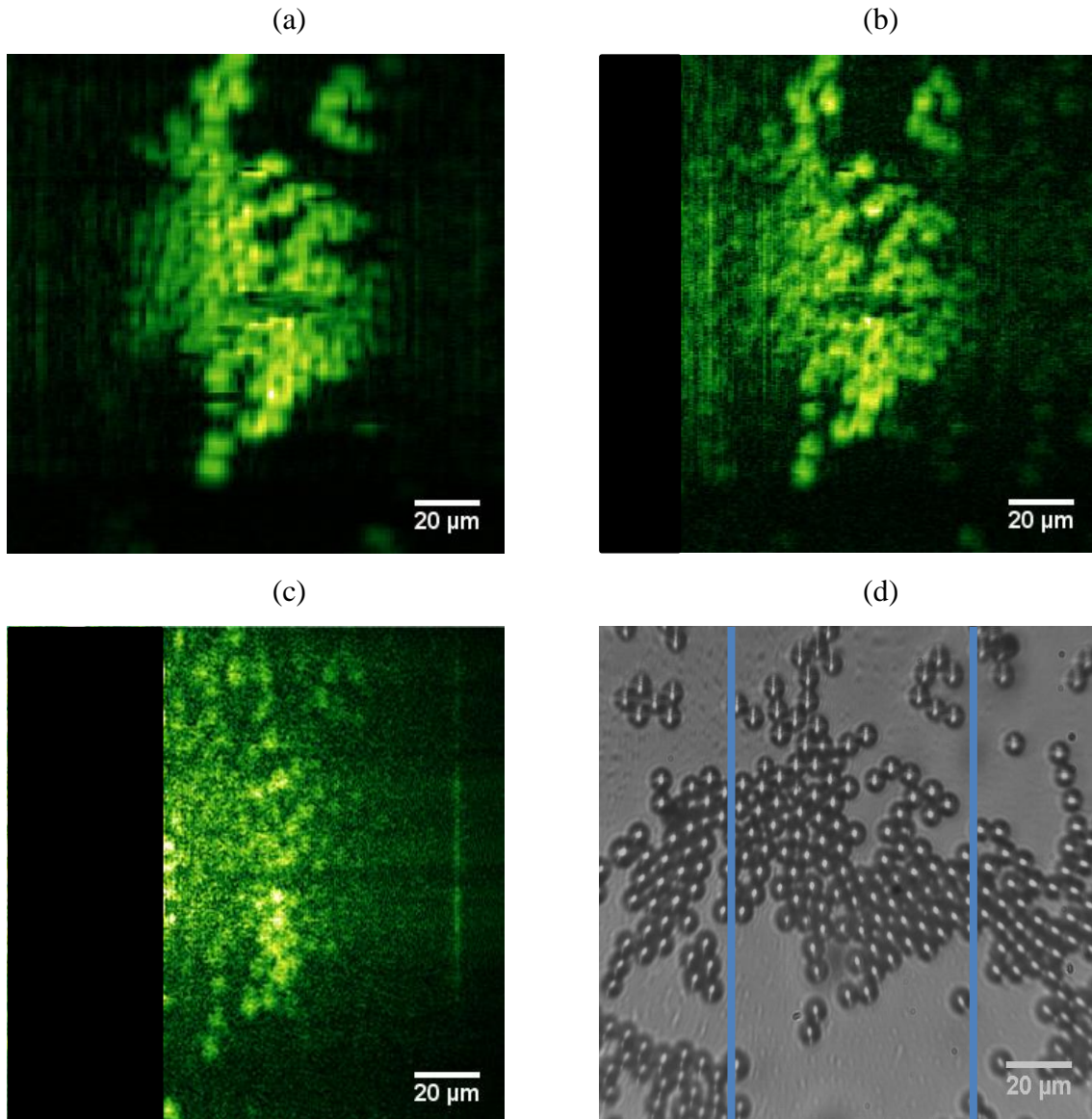


Figure 7.16 – THG SPIFI images of polystyrene beads (diameter = 6 μm). (a) – (c) first through third order images. Scale bar: 20μm. (d) portion of the sample under white light illumination.

Source: By the author.

### *THG SPIFI Imaging – Linear vs Circular*

An interesting property of the THG is that circularly polarized light does not generate TH in an isotropic medium. For a circularly polarized electric wave, the electric field vector is constant in amplitude throughout the optical cycle. The polarization vector amplitude is also a constant even though it is not linearly related to the fundamental field amplitude. Thus, the

polarization has no third-harmonic content.<sup>35,42</sup> Until now, we have used amplitude modulation with an approximately sinusoidal amplitude modulation where the beam irradiance oscillates between two limits, the maximum irradiance and almost zero. Now, the modulation is done controlling the polarization state of the beam (by phase modulation) using the SLM. Basically, we have maximum THG for linearly polarized fundamental wave and minimum for circular. By creating a mask to control the fundamental beam polarization state from linear to circular, we generate a TH oscillation which goes from maximum to zero as it happens in amplitude modulation. In this case, the modulated beam should not pass through the PBS in its way to the objective lens because the PBS would reject one polarization component and eliminate the circular/elliptical polarization. The beam should pass over the PBS as described earlier in the experimental setup section. We have used the same sample as before, polystyrene beads. The image is shown in Fig. 7.17, any higher order was observed.

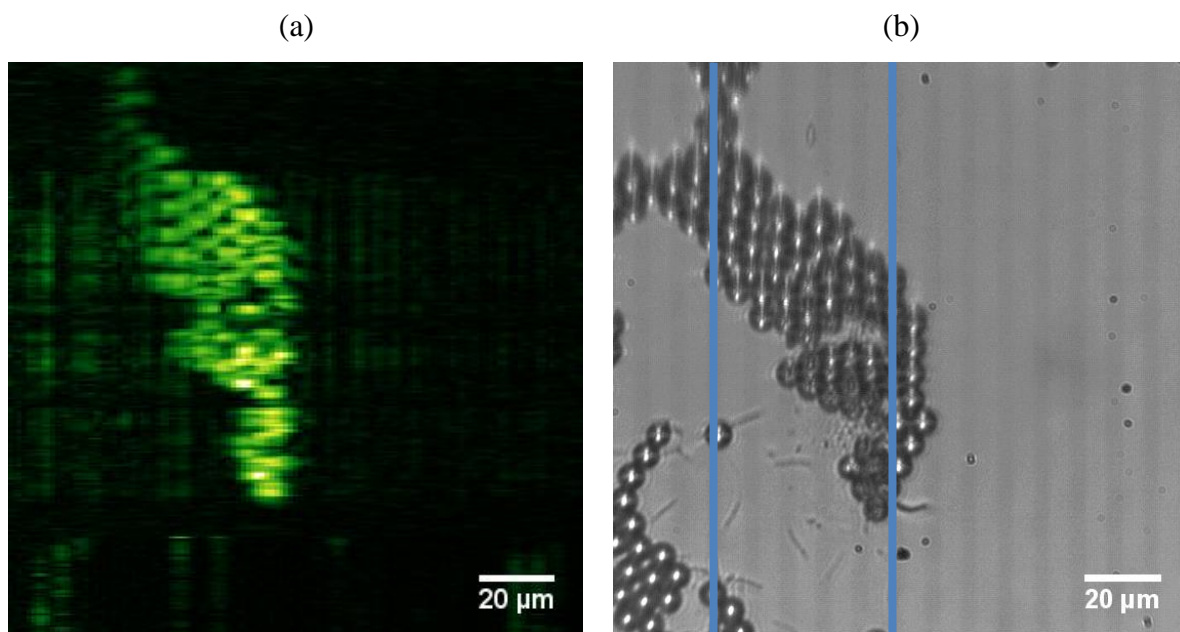


Figure 7.17 – (a) THG SPIFI image of polystyrene beads (diameter = 6  $\mu\text{m}$ ) using linear vs circular configuration. (b) portion of the sample under white light illumination. Scale bar: 20 $\mu\text{m}$ .

Source: By the author.

## 7.6 Discussion

We have presented SPIFI images using a new microscope's design where the traditional spinning disc is replaced by an SLM. Two-photon excitation fluorescence (TPEF), second- and third-harmonic generation (SHG and THG) images were taken. The THG SPIFI images by either amplitude or phase modulation (linear vs circular) are unprecedented. The

linear vs circular SPIFI image is possible because THG cannot be observed for circular polarization and because we have used the SLM instead of the spinning disc, the SLM makes possible circular polarization in selected parts of the beam. In the linear vs circular configuration, as the laser beam passes through the PBS just once, more intensity (double) is available for pumping the sample.

We have observed until the third-order signal when applying the Fourier transform (third harmonic of the fundamental beam at the frequency domain) which should be 325 nm in resolution (one-third the first order, 975 nm) for a diffraction-limited setup. Theoretically, sixth order is possible with THG. These are early results and more analysis and improvements should be done, for instance, resolution tests and signal-to-noise optimization to better visualize the higher order signals. Also, using the SLM we can quickly implement and test different masks. The time required to form a full image was about 20 to 30 minutes, therefore, scanning parameters optimization for improving the image acquisition rate is interesting as well.



## 8 GENERAL CONCLUSIONS AND PERSPECTIVES

In this dissertation, we have investigated the THG at the interfaces on different materials and understood the influence of the self-focusing on its intensity profile. In a first experiment, we have studied slabs of different optical glasses using femtosecond laser pulses. The results have shown that the self-focusing is the main reason for the TH intensity asymmetric profile and dependence of pump power at the interfaces. Although the THG is a pure third-order nonlinear process, the TH power dependence at the interfaces can be higher than 3 due to the influence of another nonlinear process, the self-focusing, which changes the beam waist at the interfaces. No significant influence of the Fresnel reflection was observed. Taking into account the self-focusing contribution, it was possible to explain the TH behavior and obtain the glasses nonlinearity.

In a second experiment, we have measured the THG of solvents inside cuvettes. To be clearer, THG at interfaces of solvent and cuvette walls using femtosecond laser pulses. The solvents may have, in addition to the electronic nonlinearity, also an orientational contribution, which is not present in optical glasses. Furthermore, the transitions between the media, at the internal interfaces of the cuvette, are not as abrupt as in the previous experiment (glass-air or air-glass). Even with these differences, our model works and, again, the self-focusing effect, which now has contribution of pure electronic and orientational nonlinearity, is important to explain the THG signal.

Preliminary results related to the THG intensity profile as a function of pulse duration were reported and a clear variation on the TH peak values at the solvent-silica interface was observed. This indicates an enhancement of the self-focusing due to the orientational nonlinearity contribution which increases with pulse duration. This result is in accordance with our expectation since self-focusing from orientational nonlinearity is not instantaneous and does depend on the pulse width. A detailed analysis with other solvents and other pulse durations would be interesting in order to discriminate the electronic and orientational contributions in the THG process.

The THG process is an important contrast mechanism in nonlinear optical microscopy. We have also presented here a modern microscopy technique, based on spatial frequency-modulated imaging (SPIFI) with a single element detection, which is capable of providing enhanced resolution images. The microscope design presented uses a SLM to provide the frequency modulation and permits to obtain images by alternative ways such as modulation by means of polarization control. We have obtained THG SPIFI images for the first time.

These are preliminary results and further resolution tests and signal-to-noise optimization are needed. Also, a detailed study with different masks would be interesting.

In general, the studies presented in this dissertation correspond to advancements in both basic and applied strands of research in third-harmonic generation and/or nonlinear optics. We were able to understand the contribution of the self-focusing on the THG at interfaces, which is very important for fundamental and applied point of view such as for materials characterization. We could also use the THG in a practical application, the microscopy. In this case, although the self-focusing was not considered at this point, it may be important in the future for correct interpretation of THG images.

---

**REFERENCES**

- 1 TSANG, T. Y. F. Optical third-harmonic generation at interfaces. **Physical Review A**, v. 52, n. 5, p. 4116-4125, 1995.
- 2 SCHINS, J. M. et al. Determination of material properties by use of third-harmonic generation microscopy. **Journal of the Optical Society of America B - optical physics**, v. 19, n. 7, p. 1627-1634, 2002.
- 3 SHCHESLAVSKIY, V.; PETROV, G.; YAKOVLEV, V. V. Nonlinear optical susceptibility measurements of solutions using third-harmonic generation on the interface. **Applied Physics Letters**, v. 82, n. 22, p. 3982-3984, 2003.
- 4 BARILLE, R. et al. Nonlinearity measurements of thin films by third-harmonic-generation microscopy. **Physical Review E**, v. 66, n. 6, p. 067602-1 - 067602-4, 2002.
- 5 SQUIER, J. A. et al. Characterization of femtosecond pulses focused with high numerical aperture optics using interferometric surface-third-harmonic generation. **Optics Communications**, v. 147, n. 1-3, p. 153-156, 1998.
- 6 TSANG, T. et al. Frequency-resolved optical-gating measurements of ultrashort pulses using surface third-harmonic generation. **Optics Letters**, v. 21, n. 17, p. 1381-1383, 1996.
- 7 BARAD, Y. et al. Nonlinear scanning laser microscopy by third harmonic generation. **Applied Physics Letters**, v. 70, n. 8, p. 922-924, 1997.
- 8 CARRILES, R. et al. Invited review article: imaging techniques for harmonic and multiphoton absorption fluorescence microscopy. **Review of Scientific Instruments**, v. 80, n. 8, p. 081101, 2009.
- 9 GOUY, L. G. Sur une propriété nouvelle des ondes lumineuses. **Comptes Rendus des Séances de l'Académie des Sciences**, v. 110, p. 1251-1253, 1890.
- 10 BOYD, R. W. **Nonlinear optics**. 3rd ed. San Diego: Academic Press, 2008.
- 11 BJORKLUND, G. C. Effects of focusing on third-order nonlinear processes in isotropic media. **IEEE Journal of Quantum Electronics**, v. QE11, n. 6, p. 287-296, 1975.
- 12 BARBANO, E. C. et al. Broadband third-harmonic generation on interfaces using femtosecond pulses. **Proceedings of SPIE**, v. 7917, 2011. doi: 10.1117/12.874790.
- 13 STOKER, D.; BECKER, M. F.; KETO, J. W. Optical third-harmonic generation using ultrashort laser pulses. **Physical Review A**, v. 71, n. 6, p. 061802, 2005.

14 WILSON, J. W.; BARTELS, R. A. Coherence-modulated third harmonic generation for vibrational spectroscopy: a theoretical treatment. **Journal of the Optical Society of America B - optical physics**, v. 29, n. 8, p. 1875-1883, 2012.

15 SHEIKBAHAE, M. et al. Sensitive measurement of optical nonlinearities using a single beam. **IEEE Journal of Quantum Electronics**, v. 26, n. 4, p. 760-769, 1990.

16 FUTIA, G. et al. Spatially-chirped modulation imaging of absorption and fluorescent objects on single-element optical detector. **Optics Express**, v. 19, n. 2, p. 1626-1640, 2011.

17 HIGLEY, D. J.; WINTERS, D. G.; BARTELS, R. A. Two-dimensional spatial-frequency-modulated imaging through parallel acquisition of line images. **Optics Letters**, v. 38, n. 11, p. 1763-1765, 2013.

18 FIELD, J. J. et al. Superresolved multiphoton microscopy with spatial frequency-modulated imaging. **Proceedings of the National Academy of Sciences of the United States of America**, v. 113, n. 24, p. 6605-6610, 2016.

19 WINTERS, D. G.; BARTELS, R. A. Two-dimensional single-pixel imaging by cascaded orthogonal line spatial modulation. **Optics Letters**, v. 40, n. 12, p. 2774-2777, 2015.

20 DENK, W.; STRICKLER, J. H.; WEBB, W. W. Two-photon laser scanning fluorescence microscopy. **Science**, v. 248, n. 4951, p. 73-76, 1990.

21 YOUNG, M. D. et al. A pragmatic guide to multiphoton microscope design. **Advances in Optics and Photonics**, v. 7, n. 2, p. 276-378, 2015.

22 NIU, W. F. et al. Highly selective two-photon fluorescent probe for ratiometric sensing and imaging cysteine in mitochondria. **Analytical Chemistry**, v. 88, n. 3, p. 1908-1914, 2016.

23 ZOUMI, A.; YEH, A.; TROMBERG, B. J. Imaging cells and extracellular matrix in vivo by using second-harmonic generation and two-photon excited fluorescence. **Proceedings of the National Academy of Sciences of the United States of America**, v. 99, n. 17, p. 11014-11019, 2002.

24 ZIPFEL, W. R. et al. Live tissue intrinsic emission microscopy using multiphoton-excited native fluorescence and second harmonic generation. **Proceedings of the National Academy of Sciences of the United States of America**, v. 100, n. 12, p. 7075-7080, 2003.

25 CAMPAGNOLA, P. Second harmonic generation imaging microscopy: applications to diseases diagnostics. **Analytical Chemistry**, v. 83, n. 9, p. 3224-3231, 2011.

- 
- 26 BARBANO, E. C.; ZILIO, S. C.; MISOGUTI, L. Influence of self-focusing of ultrashort laser pulses on optical third-harmonic generation at interfaces. **Optics Letters**, v. 38, n. 23, p. 5165-5168, 2013.
- 27 BARBANO, E. C. et al. Third-harmonic generation at the interfaces of a cuvette filled with selected organic solvents. **Applied Optics**, v. 55, n. 3, p. 595-602, 2016.
- 28 FOWLES, G. R. **Introduction to modern optics**. 2nd ed. Mineola: Dover Publications, 1989.
- 29 BLOEMBERGEN, N. **Nonlinear optics: a lecture note and reprint volume**. New York: W. A. Benjamin, 1965.
- 30 DIELS, J-C.; RUDOLPH, W. **Ultrashort laser pulse phenomena: fundamentals, techniques, and applications on a femtosecond time scale**. 2nd ed. San Diego: Academic Press, 2006.
- 31 YARIV, A. **Quantum electronics**. 3rd ed. New York: John Wiley & Sons, 1989.
- 32 ESTRADA, D. M. E. **Propagação de feixes ópticos em meios não-lineares**. 2008. 146 p. Dissertação (Mestrado em Engenharia Electrotécnica e de Computadores) - Instituto Superior Técnico, Universidade Técnica de Lisboa, Lisboa, 2008.
- 33 ZÍLIO, S. C. **Óptica moderna: fundamentos e aplicações**. São Carlos: Instituto de Física de São Carlos, Universidade de São Paulo, 2009.
- 34 KLEINMAN, D. A.; ASHKIN, A.; BOYD, G. D. Second-harmonic generation of light by focused laser beams. **Physical Review**, v. 145, n. 1, p. 338-&, 1966.
- 35 WARD, J. F.; NEW, G. H. C. Optical third harmonic generation in gases by a focused laser beam. **Physical Review**, v. 185, n. 1, p. 57-&, 1969.
- 36 PELEGATI, V. B. **Microscopias de óptica não linear: fluorescência excitada por absorção de dois fótons, geração de segundo harmônico e geração de terceiro harmônico**. 2010. 96 p. Dissertação (Mestrado em Física) - Instituto de Física "Gleb Wataghin", Universidade Estadual de Campinas, Campinas, 2010.
- 37 PUELL, H. et al. Third-harmonic generation of mode-locked Nd-glass laser-pulses in phase-matched Rb-Xe mixtures. **Physical Review A**, v. 14, n. 6, p. 2240-2257, 1976.
- 38 MAKER, P. D. et al. Effects of dispersion and focusing on production of optical harmonics. **Physical Review Letters**, v. 8, n. 1, p. 21-&, 1962.

39 HEISLER, I. A. et al. Spectrally resolved femtosecond Maker fringes technique. **Applied Physics Letters**, v. 92, n. 9, p. 091109-1 – 091109-3, 2008.

40 HEYL, C. M. et al. Spectrally resolved Maker fringes in high-order harmonic generation. **Physical Review Letters**, v. 107, n. 3, p. 033903-1 – 033903-4, 2011.

41 HERMAN, W. N.; HAYDEN, L. M. Maker fringes revisited: second-harmonic generation from birefringent or absorbing materials. **Journal of the Optical Society of America B-optical physics**, v. 12, n. 3, p. 416-427, 1995.

42 REINTJES, J. F. Third-harmonic generation and third-order frequency mixing. In: \_\_\_\_\_. **Nonlinear optical parametric processes in liquids and gases**. Orlando: Academic Press, 1984. cap. 2, p.31-148.

43 CHENG, J. X.; XIE, X. S. Green's function formulation for third-harmonic generation microscopy. **Journal of the Optical Society of America B-optical physics**, v. 19, n. 7, p. 1604-1610, 2002.

44 BOYD, R. W. Intuitive explanation of the phase anomaly of focused light-beams. **Journal of the Optical Society of America**, v. 70, n. 7, p. 877-880, 1980.

45 KALTENECKER, K. J. et al. Gouy phase shift of a tightly focused, radially polarized beam. **Optica**, v. 3, n. 1, p. 35-41, 2016.

46 PAPADOPOULOS, M. G.; SADLEJ, A. J.; LESZCZYNSKI, J. **Non-linear optical properties of matter: from molecules to condensed phases**. Dordrecht: Springer Science & Business Media, 2007.

47 KELLEY, P. L. Self-focusing of optical beams. **Physical Review Letters**, v. 15, n. 26, p. 1005-&, 1965.

48 ROBERT, B. W. **Nonlinear optics**. 2nd ed. San Diego: Academic Press, 1992.

49 KOECHNER, W. **Solid-state laser engineering**. 6th ed. New York: Springer-Verlag, 2006.

50 REINTJES, J. F. **Nonlinear optical parametric processes in liquids and gases**. Orlando: Academic Press, 1984.

51 MCTAGUE, J. P. et al. Observation of filaments in liquid argon. **Physics Letters A**, v. 32, n. 2, p. 82-&, 1970.

52 MACK, M. E. et al. Transient stimulated rotational and vibrational raman scattering in gases. **Applied Physics Letters**, v. 16, n. 5, p. 209-&, 1970.

- 53 GRISCHKO, D. Self-focusing of light by potassium vapor. **Physical Review Letters**, v. 24, n. 16, p. 866-870, 1970.
- 54 BJORKHOL, J. E.; ASHKIN, A. CW self-focusing and self-trapping of light in sodium vapor. **Physical Review Letters**, v. 32, n. 4, p. 129-132, 1974.
- 55 SHEN, Y. R. **The principles of nonlinear optics**. New York: John Wiley & Sons, 1984.
- 56 BARBANO, E. C. **Técnica de varredura-Z com pulsos de femtossegundo e geração de terceiro harmônico**. 2012. 95 p. Dissertação (Mestrado em Ciências) - Instituto de Física de São Carlos, Universidade de São Paulo, São Carlos, 2012.
- 57 SHEIKBAHAIE, M.; SAID, A. A.; VANSTRYLAND, E. W. High-sensitivity, single-beam  $n_2$  measurements. **Optics Letters**, v. 14, n. 17, p. 955-957, 1989.
- 58 RAU, I. et al. Comparison of Z-scan and THG derived nonlinear index of refraction in selected organic solvents. **Journal of the Optical Society of America B-optical physics**, v. 25, n. 10, p. 1738-1747, 2008.
- 59 MAGNI, V.; CERULLO, G.; DESILVESTRI, S. ABCD matrix analysis of propagation of gaussian beams through Kerr media. **Optics Communications**, v. 96, n. 4-6, p. 348-355, 1993.
- 60 MILAM, D. Review and assessment of measured values of the nonlinear refractive-index coefficient of fused silica. **Applied Optics**, v. 37, n. 3, p. 546-550, 1998.
- 61 HAZARIKA, S.; RAI, S. Characteristics of  $\text{Nd}^{3+}$  ions in sol-gel derived silicate glass in presence of  $\text{Al}(\text{NO}_3)_3$  and the  ${}^4\text{F}_{3/2} \rightarrow {}^4\text{I}_{11/2}$  transition. **Optical Materials**, v. 30, n. 3, p. 462-467, 2007.
- 62 BOLING, N. L.; GLASS, A. J.; OWYOUNG, A. Empirical relationships for predicting non-linear refractive-index changes in optical solids. **IEEE Journal of Quantum Electronics**, v. 14, n. 8, p. 601-608, 1978.
- 63 PILLAI, R. S.; BRAKENHOFF, G. J.; MULLER, M. Anomalous behavior in the third harmonic generation z response through dispersion induced shape changes and matching  $\chi^{(3)}$ . **Applied Physics Letters**, v. 89, n. 11, p. 111123, 2006.
- 64 PILLAI, R. S.; BRAKENHOFF, G. J.; MULLER, M. Analysis of the influence of spherical aberration from focusing through a dielectric slab in quantitative nonlinear optical susceptibility measurements using third-harmonic generation. **Optics Express**, v. 14, n. 1, p. 260-269, 2006.

65 SHCHESLAVSKIY, V. et al. Quantitative characterization of aqueous solutions probed by the third-harmonic generation microscopy. **Journal of Structural Biology**, v. 147, n. 1, p. 42-49, 2004.

66 NAUMOV, A. N. et al. Third-harmonic generation in focused beams as a method of 3D microscopy of a laser-produced plasma. **Optics and Spectroscopy**, v. 90, n. 5, p. 778-783, 2001.

67 MALITSON, I. H. Interspecimen comparison of refractive index of fused silica. **Journal of the Optical Society of America**, v. 55, n. 10, p. 1205-&, 1965.

68 B270 DATASHEET. 1993. Available from: <http://refractiveindex.info/?shelf=glass&book=SCHOTT-multipurpose&page=B270>. Accessible at: 21 Jun. 2016.

69 RHEIMS, J.; KOSER, J.; WRIEDT, T. Refractive-index measurements in the near-IR using an Abbe refractometer. **Measurement Science & Technology**, v. 8, n. 6, p. 601-605, 1997.

70 KEDENBURG, S. et al. Linear refractive index and absorption measurements of nonlinear optical liquids in the visible and near-infrared spectral region. **Optical Materials Express**, v. 2, n. 11, p. 1588-1611, 2012.

71 KOZMA, I. Z.; KROK, P.; RIEDLE, E. Direct measurement of the group-velocity mismatch and derivation of the refractive-index dispersion for a variety of solvents in the ultraviolet. **Journal of the Optical Society of America B-optical physics**, v. 22, n. 7, p. 1479-1485, 2005.

72 SHI, G. et al. Excited-state nonlinearity measurements of ZnPcBr<sub>4</sub>/DMSO. **Journal of the Optical Society of America B-optical physics**, v. 26, n. 4, p. 754-761, 2009.

73 CRISP, M. D.; BOLING, N. L.; DUBE, G. Importance of Fresnel reflections in laser surface damage of transparent dielectrics. **Applied Physics Letters**, v. 21, n. 8, p. 364-&, 1972.

74 CHEN, Y. H. et al. Measurement of transient nonlinear refractive index in gases using xenon supercontinuum single-shot spectral interferometry. **Optics Express**, v. 15, n. 12, p. 7458-7467, 2007.

75 REICHERT, M. et al. Temporal, spectral, and polarization dependence of the nonlinear optical response of carbon disulfide. **Optica**, v. 1, n. 6, p. 436-445, 2014.

76 MASIHZADEH, O.; SCHLUP, P.; BARTELS, R. A. Enhanced spatial resolution in third-harmonic microscopy through polarization switching. **Optics Letters**, v. 34, n. 8, p. 1240-1242, 2009.

- 77 MULLER, M. et al. 3D microscopy of transparent objects using third-harmonic generation. **Journal of Microscopy**, v. 191, n. 3, p. 266-274, 1998.
- 78 SQUIER, J. A. et al. Third harmonic generation microscopy. **Optics Express**, v. 3, n. 9, p. 315-324, 1998.
- 79 HOOVER, E. E. et al. Eliminating the scattering ambiguity in multifocal, multimodal, multiphoton imaging systems. **Journal of Biophotonics**, v. 5, n. 5-6, p. 425-436, 2012.
- 80 BLOCK, E. et al. Simultaneous spatial frequency modulation imaging and micromachining with a femtosecond laser. **Optics Letters**, v. 41, n. 2, p. 265-268, 2016.
- 81 HWANG, J. et al. Frequency- and spectrally-encoded confocal microscopy. **Optics Express**, v. 23, n. 5, p. 5809-5821, 2015.
- 82 YOUNG, M. D. **Developments in multifocal multiphoton microscopy with single element detection**. 2015. 192 p. Ph. D. Thesis (Applied Physics) - Colorado School of Mines (CSM), Faculty and the Board of Trustees of Colorado, Golden, CO, 2015.
- 83 BRAKENHOFF, G. J. et al. Real-time two-photon confocal microscopy using a femtosecond, amplified Ti:sapphire system. **Journal of Microscopy**, v. 181, n. 3. p. 253-259, 1996.
- 84 BENDIX Corp. Donald J. Lovell. **Electro-optic position indicator system**. US2997699 A, 3 Aug. 1959, 22 Aug. 1961.
- 85 DRIGGERS, R. G.; HALFORD, C. E.; BOREMAN, G. D. Use of spatial light modulators in frequency-modulation reticle trackers. **Optical Engineering**, v. 29, n. 11, p. 1398-1403, 1990.